Loss Mechanisms in a Highly Loaded Transonic Axial Turbine Stage

by

Kevin R. Shannon
B.S. Mechanical and Aerospace Engineering
Cornell University (2012)

Submitted to the Department of Aeronautics and Astronautics
in partial fulfillment of the requirements for the degree of
Master of Science in Aeronautics and Astronautics
at the
MASSACHUSETTS INSTITUTE OF TECHNOLOGY
June 2018

Signature redacted

Author .....
Department of Aeronautics and Astronautics
May 24, 2018

Signature redacted

Certified by .....
Choon S. Tan
Senior Research Engineer of Aeronautics and Astronautics
Thesis Supervisor

Certified by ..... Signature redacted
John P. Clark
Principal Engineer at the Air Force Research Laboratory
Thesis Supervisor

Certified by ..... Signature redacted .....
Scott M. Carson
Consulting Engineer at GE Aviation
Thesis Supervisor

Accepted by ..... Signature redacted .....
Hamsa Balakrishnan
Associate Professor of Aeronautics and Astronautics
Chair, Graduate Program Committee

Loss Mechanisms in a Highly Loaded Transonic Axial Turbine Stage

by

Kevin R. Shannon

Submitted to the Department of Aeronautics and Astronautics
on May 24, 2018, in partial fulfillment of the
requirements for the degree of
Master of Science in Aeronautics and Astronautics

Abstract

Flow in a one-and-a-half stage highly loaded transonic axial turbine representative of future generation turbine technology is assessed for its role in loss generation. Steady and unsteady two-dimensional and three-dimensional flow computations, complemented by simplistic control volume analyses as well as test data, provided results for establishing the quantitative level of loss from various sources. The test data has been acquired in a cascade and blowdown turbine research rig. Specifically, the overall loss determined from unsteady three-dimensional flow computations of a cooled one-and-a-half stage turbine is within 6% of that inferred from the blowdown turbine rig test data. The computed flows with different levels of flow and configuration complexities are post-processed and interrogated to allow an estimation of blade profile loss, trailing edge loss, shock loss, endwall loss, secondary flow loss, tip leakage loss, cooling injection loss, and unsteady flow loss. The dominant sources of loss are determined to be the trailing edge loss, profile loss, and tip leakage loss. The computed flows show that the flow deviation in a highly loaded transonic turbine airfoil with trailing edge shocks is negative (-2° to -4°); estimating the trailing edge loss by assuming zero flow deviation in a simple control volume approach would yield a significantly higher value. Loss arising from flow unsteadiness contributes an additional loss of about 1/6 of that in steady flow approximation; 3/4 of the flow unsteadiness induced loss occurs in the downstream vane where the flow is threaded with propagating shocks from the upstream blade and downstream shock reflections; and the remaining 1/4 is from unsteadiness in NGV wakes and shock oscillations from influence of the adjacent airfoil row. 1/5 of the overall loss in the one-and-a-half stage turbine is from the cooling and purge flows. A preliminary assessment of loss variation with turbine stage pressure ratio shows a non-monotonic trend.

Thesis Supervisor: Choon S. Tan
Title: Senior Research Engineer of Aeronautics and Astronautics

Thesis Supervisor: John P. Clark
Title: Principal Engineer at the Air Force Research Laboratory

Thesis Supervisor: Scott M. Carson
Title: Consulting Engineer at GE Aviation

Acknowledgments

The path through the past two years has been paved by the unconditional support of countless advisors, colleagues, friends, and family. I'd like to acknowledge everyone who has taken time to carry some portion of the load.

First and foremost, I would like to thank my research advisor Dr. Tan for unparalleled guidance, encouragement, and friendship over the course of the writing of this thesis. He has continuously pushed me to expand my thinking and achieve a higher level. I have learned as much about the world and myself from our conversations as about aerodynamics. I am also grateful to my advisor Dr. John Clark at the Air Force Research Lab for his dedication to this project. I couldn't have accomplished this work without his technical mentorship, continuous feedback, and analytical expertise.

Thank you to my GE Aviation advisors Scott Carson and Chris Johnson, I could always rely on them for new perspectives and insightful technical review. I am thankful to GE Aviation for making this project possible, in particular Dr. Dave Halstead, Dr. Eric Falk, Peter Rock, and Paul Vitt. I would like to thank my GE colleagues John Tawfik, Chris King, and Piotr Gradkowski for helping me turn the corner when I was stuck. My deepest thanks go to Dan Barber and Andy Ramsey for supporting me in this endeavor and giving me the freedom to pursue this opportunity. Thank you Tom Martyn, Dr. Fred Buck, and Dr. Gunnar Siden for reviewing my thesis. I also extend my gratitude to the GE ACE program for supporting my master's degree, especially to Paul Patoulidis and Ken Gould for the advice and encouragement.

My time spent at the GTL has been highlighted by my inspiring lab mates, each one a more incredible source of knowledge and experience than the last. I am grateful for the friendships I have made, especially to Pete Rock and Sebastien Mannai. Their support has been invaluable, and our friendship will continue far past graduation.

Last but not least, my loving family has given me an excess of encouragement, understanding, and motivation. Brendan has shown me what true energy is possible and Caitlin's optimism is contagious. Thank you Mom for teaching me how to learn and grow, and Dad for instilling the determination to get the job done.

Contents

List of Figures

List of Tables

Nomenclature

Abbreviations

$1B$ first blade row

$1V$ first vane row, upstream vane row

$2V$ second vane row, downstream vane row

$AFRL$ Air Force Research Lab

$BOAS$ blade outer air seal

CFD computational fluid dynamics

$CSKE$ coefficient of secondary kinetic energy

CV control volume

DFT discrete Fourier transform

HIT High Impact Technologies

ID inner diameter

NGV nozzle guide vane

OD outer diameter

$P2VYI21$ downstream vane endwall Kulite name

$PRTT15$ blade suction side Kulite name

PS pressure side

$RANS$ Reynolds-averaged Navier-Stokes

SKE secondary kinetic energy

SS suction side

SST shear-stress transport

TE trailing edge

$WPAFB$ Wright Patterson Air Force Base

Greek

α flow angle measured from the axial direction

β flow angle measured from the axial direction in rotating reference frame

δ boundary layer overall thickness, flow angle deviation at trailing edge

δ^* boundary layer displacement thickness

δ_s boundary layer entropy thickness

ϵ angle of tip leakage flow relative to mainstream

γ specific heat ratio

κ angle of cooling flow relative to mainstream

ρ fluid density

θ boundary layer momentum thickness

ζ entropy loss coefficient

Subscripts

1 inlet to the trailing edge control volume, airfoil row inlet

2	exit to the trailing edge control volume, airfoil row exit
b	base of the trailing edge
c	coolant flow
$exit$	domain exit
$free$	free stream
in	domain inlet
inj	injected flow
m	mainstream flow
$norm$	normalized to exit condition
o	stagnation conditions
r	radial
s	edge of entropy boundary layer, suction side
sec	secondary flow
te	just before the trailing edge
u	direction of blade rotation
$visc$	viscous portion of loss
z	axial

Symbols

$\dot{m}$	mass flow rate
$\dot{S}_a$	entropy creation rate per unit surface area
$\dot{S}_v$	entropy creation rate per unit volume

A area

C chord

C_d dissipation coefficient

C_p, C_v specific heat capacities

C_x airfoil axial chord

C_{pb} base pressure coefficient

g tip clearance

h blade height, flowpath height

h_o stagnation enthalpy

M Mach number

m_{fc} mass fraction of coolant

M_T blade tangential Mach number

P static pressure

P_o stagnation pressure

R gas constant

r radius

Re_θ Reynolds number based on momentum thickness

S total entropy

s specific entropy

s_δ specific entropy at edge of boundary layer

T static temperature

t trailing edge thickness

T_o stagnation temperature

U blade rotational speed

V flow velocity

V_δ blade surface velocity at edge of boundary layer

V_{leak} velocity of tip leakage flow

w throat width

x, y, z Cartesian coordinates

y^+ dimensionless wall distance

Chapter 1

Introduction and Background

Gas turbines are the predominant choice for aircraft propulsion. A high power-to-weight ratio, high fuel power density, and steady gains in turbine engine efficiency contribute to their popularity in aircraft applications. With contemporary turbine component efficiencies reaching well above 90%, it becomes important to assess system performance in concert with turbine aerodynamic design. This research explores the aerodynamic impact of increasing the work extraction of a gas turbine stage by raising the loading, a historical detriment to efficiency, with the goal of stage count reduction. A high work stage is accomplished by high airfoil turning, high stage pressure ratio, and high rotational speed, hereafter referred to as a highly loaded transonic turbine stage. A single high work stage can provide reduced system weight, cost, and complexity.

Understanding the aerodynamic losses of highly loaded transonic turbines is critical to reducing them in the design process. A primary goal of this thesis is to account systematically for loss sources within a high work turbine stage, present the primary drivers for irreversibilities, and suggest scaling rules for the reduction of these losses.

1.1 Motivation for a Highly Loaded Transonic Stage

The modern gas turbine engine generally utilizes multiple high pressure turbine stages for work extraction. This is necessary to keep blade loading and exit relative Mach

numbers within experience, while at the same time providing the work to power ever-higher pressure ratio compressors. Turbine blade rows are designed with subsonic exit relative Mach numbers to avoid passage shocks, trailing edge shocks, and other transonic effects that are not well understood. These flow mechanisms lead to inefficiencies, and avoiding them necessitates a multiple stage design.

Alternatively, at a detriment to efficiency, a single stage turbine can be used to extract the same amount of work. A large pressure ratio is applied across the stage, and the blade row is designed with a large amount of turning to increase the lift. In a highly loaded turbine stage the work extraction can be double that of a lightly loaded, subsonic blade row. With this increased loading, the blade exit relative velocity is increased to transonic levels, and the flow is prone to losses from high Mach number and unsteady effects.

The objective of this research is to quantify loss generation in a 1.5 stage highly loaded transonic axial turbine. This will be accomplished by implementing CFD simulations of a 1.5 stage highly loaded turbine and assessing the results against test data acquired at the Air Force Research Lab (AFRL). The CFD model is a 3D, multistage, unsteady calculation to match the unsteady test data. The research outcome is a consistent and rigorous loss accounting of a highly loaded turbine stage, and an assessment of the impact of pressure ratio, Mach number, and incidence angle on aerodynamic losses.

1.2 Literature Review

The subject of aerodynamic loss in turbines is well studied, but with limited focus on highly loaded designs and unsteady loss mechanisms. Denton [1] provides a foundational description of loss components and the use of entropy generation as a measure of turbine performance. Denton describes the steady loss mechanisms of interest and gives general guidelines for their contribution to turbine loss. The control volume analysis for trailing edge loss concludes that this loss is driven by geometric parameters, boundary layer size, and base pressure. Denton and Xu [2] give a detailed

discussion of the implications of transonic flow on trailing edge loss.

There have been several efforts to account for the losses in a turbine cascade or stage. Mee [3] evaluates a turbine cascade for Mach numbers ranging from 0.6 to 1.2 and estimates the relative contributions of profile loss, shock loss, and mixing loss. Duan [4] calculates the profile loss, shock loss, and trailing edge loss of a high Mach number turbine blade cascade. The power generation blade design in Duan's research has low turning and a thinner trailing edge than necessary for a cooled high work turbine, and so the trailing edge and mixing loss are lower than calculated in this thesis. Duan's profile loss calculation from boundary layer details is used in this research. The 2D loss accounting by Duan is expanded upon in this research by considering 3D loss generating mechanisms, and applying loss models to three airfoil rows in a 1.5 stage highly loaded turbine. Yoon [5] presents a loss audit of a transonic turbine stage that includes 3D effects of endwall loss and shrouded tip leakage. The results of this analysis are achieved by manipulating the CFD boundary conditions. Shock loss and trailing edge loss are not separated, leading to a high reported trailing edge loss for the rotor.

Tip clearance loss and purge flow loss are important 3D loss generating mechanisms that have been assessed with control volume methods. Huang [6] and Sakulkaew [7] discuss the calculation of tip clearance loss. Huang describes the implementation of a tip leakage control volume model, and then applies the model to turbine blades with varying tip loading. The same model is applied by Sakulkaew to a compressor stage with tip clearances varying from 0.04% to 5% span. The steady loss generating mechanisms associated with purge flow injection are quantitatively categorized by Zlatinov [8]. Volumetric entropy generation rate is discussed along with its numerical implementation limits. Clifton [9] also examines the effects of purge flow with a focus on unsteady interactions. The unsteady impact of vane wake pressure variation and rotor bow waves on purge flow loss is assessed.

The 1.5 stage turbine assessed in this thesis has significant airfoil cooling, and it is important to estimate the losses associated with cooling flow injection. Horlock, Young and Wilcock [10] discuss performance considerations for turbines with large

cooling flows. Horlock [11] also gives an overview of the basic thermodynamics of cooled turbines. Lim [12] describes a method for calculating film cooling loss and extends the solution for application to 3D injection angles. These techniques, which expand upon Denton's two stream mixing loss [1], are leveraged for this thesis.

Unsteady losses occur in turbines from the interaction between rotating and stationary blade rows. Denton describes several unsteady loss mechanisms; however, does not mention interaction between blade trailing edge shocks and the downstream vane row. The effect of upstream vane (NGV) trailing edge shocks on blade performance is mentioned, although it is not quantified. Ng and Epstein [13] calculate a small loss from periodic trailing edge shock motion, although this result is not shown to be general. The unsteady loss for a transonic turbine stage (NGV and blade) is quantified by Yoon [5] using CFD analysis. This thesis further investigates and quantifies unsteady loss in a highly loaded 1.5 stage turbine.

The turbine design used for this research is the High Impact Technologies (HIT) turbine designed at the Air Force Research Lab (AFRL). Anthony and Clark [14] led the design and test of HIT turbine and describe the challenges of designing a highly loaded turbine to mitigate unsteady forcing. The design and test of the HIT turbine and cascade experiments is thoroughly documented by Ooten [15].

An extensive research body is available for many of the loss generating mechanisms that afflict modern turbomachinery; however, not all of these losses are quantified for a high turning and high Mach number transonic turbine stage. The impact of trailing edge flow deviation is mentioned in the literature, but not quantified. Little research quantifies the loss generated from unsteady effects and blade-vane interaction of a highly loaded turbine stage.

1.3 Objective of Present Work

The goal of this work is to quantify the loss generating flow mechanisms in highly loaded turbine stages representative of designs for the next generation of aircraft engines. The focus is on a highly loaded transonic turbine stage in which unsteady shock

interactions are significant. To accomplish this goal, the following specific research objectives are addressed:

1. Quantify the loss sources in a 1.5 stage highly loaded transonic turbine.

2. Suggest scaling rules for loss generation in a highly loaded transonic turbine stage. Propose guidelines for improving turbine performance.

1.4 Contributions and Findings

The 1.5 stage turbine loss measured from a blowdown test is compared to a 1.5 stage CFD analysis. The CFD analysis includes steady and unsteady effects, purge flow, and cooling flow consistent with the blowdown test. The 1.5 stage overall loss from CFD is within 6% of the measured loss. CFD simulations and reduced order analytical models for the steady loss, unsteady loss, purge flow, and cooling flow are consistent with the test results.

The individual loss sources of a 1.5 stage highly loaded transonic turbine are determined and quantified for each airfoil row. A significant portion of the loss is from steady aerodynamic mechanisms, and additional loss is from unsteady sources. In quantitative terms, the design point 3D blade steady losses are 24% trailing edge loss, 18% profile loss, 23% shock loss from the steady trailing edge shocks, 26% tip leakage loss, 9% endwall loss, and 1% secondary flow vortex loss. The largest 2D cascade loss source is trailing edge loss. It is found that the calculated magnitude of trailing edge loss has a strong functional dependence on deviation, and negative deviation is possible in a high turning transonic turbine stage, which significantly lowers the trailing edge loss calculated assuming no deviation. A parametric assessment of the steady loss generating mechanisms shows a non-monotonic trend with pressure ratio and exit Mach number, which is consistent with findings from Mee [3] and Duan [4].

The unsteady losses in the turbine stage are from the interaction between the blade and upstream vane (NGV) wake, the blade trailing edge shock oscillation, and the movement of the blade trailing edge shock system through the downstream vane

row. The unsteady time averaged entropy generation in a 1.5 stage highly loaded transonic turbine is quantified. The total unsteady loss is 13% higher than the total steady loss. The majority of the unsteady loss is generated in the downstream vane airfoil row, where shocks from the blade row propagate into the stationary domain.

1.5 Organization of Thesis

This thesis is organized to best communicate the contributions and findings. Chapter 2 lays out the overall approach to accomplish the goals outlined in this chapter. Chapter 3 gives a summary and background of the turbine testing performed at the AFRL which enables this research. Chapter 4 describes the CFD experiments that are implemented to support the research objectives. The CFD setup, assumptions, and methodology are described. Chapter 5 describes the analysis techniques that are employed to quantify the various losses. This chapter is organized by loss generation mechanisms, and a detailed description of the control volumes, assumptions, and limitations is provided. Chapter 6 presents the results of these loss calculations for 2D cascade, 3D airfoil row, and full 1.5 stage analyses. These calculated losses are compared to that estimated from computed flow field and test data. Chapter 6 also gives a parametric assessment of the variation in loss mechanisms in response to pressure ratio, exit Mach number, and incidence angle. Chapter 7 summarizes the research findings and provides suggestions for future work.

Chapter 2

Research Approach

Experimental results analysis, CFD simulation, and simplified control volume calculation are necessary to fully characterize the loss generating mechanisms in a highly loaded turbine. A 1.5 stage highly loaded transonic turbine, incorporating future generation turbine aerodynamics technology, was designed by the Air Force Research Lab (AFRL). This design, named the High Impact Technologies (HIT) research turbine, was tested in the blowdown test facility at Wright Patterson Air Force Base (WPAFB). Figure 2-1 is a picture of the facility with the test rig in center, supply tank at left, and discharge tanks at right. In addition to the blowdown test, stationary cascades of several airfoil sections were tested. All testing was completed in 2014 and an extensive data set is available for this research.

2D and 3D CFD models are created based on the HIT turbine design, and the results are assessed against the cascade and HIT experimental data. The CFD scope for this project ranges from blade-only 2D steady to multistage 3D unsteady models.

Boundary conditions from the CFD simulations are used to perform a complete loss accounting of the turbine with control volume and physics based models. This research seeks to explain the physical flow mechanisms of the observed losses, particularly the shock loss and unsteady shock interaction between the blade and downstream vane. A parametric assessment is performed to determine the loss generation trends in a highly loaded 1.5 stage turbine. The goal of this research is to make suggestions for improving turbine performance based on the findings.

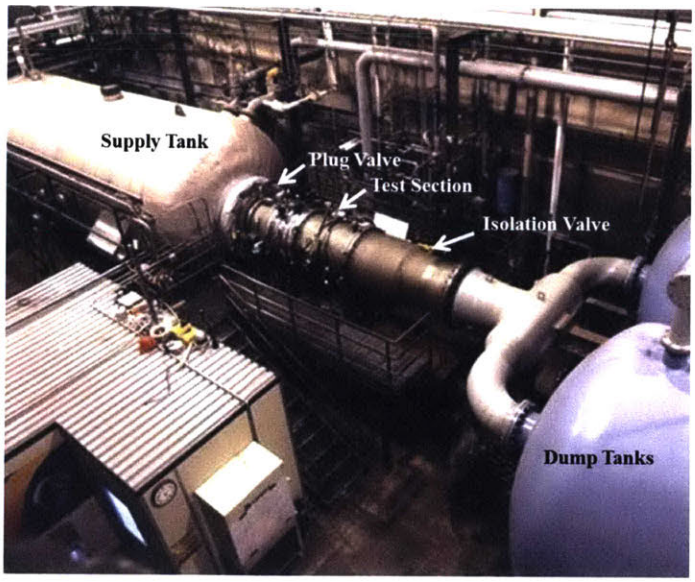

Figure 2-1: The High Impact Technologies turbine rig and the blowdown facility at WPAFB where the experimental data for this thesis was collected. [15]

2.1 Entropy Generation as a Measure of Loss

The ultimate judgment of gas turbine performance is efficiency. Inefficiency in a gas turbine is the result of a reduced ability of the flow to do work. Traditionally, many measures have been employed to quantify turbine efficiency. Loss coefficients are common because their inputs are readily available from test instrumentation. Loss coefficients, however, cannot account for isentropic stagnation pressure rise or fall from radius change of the flow in a rotating passage, and therefore are limited to use on cascade tests. In a gas turbine, isentropic efficiency is useful for determining the actual work of a turbine compared to the isentropic work. Isentropic efficiency purely measures the deviation of a real flow from an isentropic process, and therefore quantifying entropy generation is fundamental to determining isentropic efficiency.

The use of entropy generation as a method to describe losses in a turbine is useful since it is irrelevant whether the machine is rotating or stationary. Entropy generation is independent of reference frame. Both rotating and stationary airfoil rows are assessed in this thesis, and it is useful to compare entropy generation across airfoil rows of a 1.5 stage turbine.

Entropy generation in an adiabatic gas turbine is limited to irreversible viscous flow processes and shock loss. Thermal mixing between cooling or purge flow and the main gas path also generates entropy; however, the loss from these processes is generally charged to the turbine cycle efficiency. Irreversible entropy generation is the fundamental cause of inefficiency in a gas turbine, and therefore it is the best method for describing loss.

2.2 Loss Accounting Methodology

The losses in an airfoil row are classified by their flow mechanism or geometric source. The steady loss generating mechanisms in a turbine airfoil row can be divided into the following categories: profile loss, trailing edge loss, oblique shock loss, tip leakage loss, endwall loss, secondary flow loss, and cooling and purge flow loss. Additionally, unsteady loss generating mechanisms are present in a 1.5 stage highly loaded turbine. Upstream vane (NGV) wakes interact with the downstream blades, trailing edge and reflected shocks oscillate from periodic pressure fluctuations, and reflected shocks travel upstream and downstream between airfoil rows. To identify the quantitative contribution of these unsteady loss mechanisms, steady and unsteady computational assessments are compared. A quasi-steady modeling approach is used by applying steady control volume models to discrete timepoints of the unsteady analysis.

Loss components that are measured by entropy generation can be summed to find the total entropy generated for an airfoil row. Furthermore, the entropy generated by multiple airfoil rows can be summed to find the loss generated by the full turbine stage. In this thesis, computational entropy generation results from control volume analysis, CFD, and test data are compared for individual airfoil rows and the full 1.5 stage turbine.

2.3 Computational Tools

The General Electric (GE) CFD tool TACOMA is used for this research. TACOMA was chosen over other commercially available tools because of its ability to dovetail with the GE HPC cluster, its robust handling of mixing plane and multistage calculations, and computationally efficient unsteady analysis. The grid is a structured grid with $y^+<1$, and is created using commercial software Autogrid. Wall functions are not used and the boundary layer is resolved to the wall. The boundary layer details are needed for several loss calculations. The shear-stress transport (SST) k-ω turbulence model is used.

2.4 Summary

The loss generating mechanisms of a highly loaded transonic 1.5 stage turbine are characterized by assessing experimental data, implementing CFD simulations, and performing simple control volume calculations. Entropy generation is employed to quantify the losses for individual flow mechanisms, airfoil rows, and the entire 1.5 stage turbine. A full range of physical and geometric complexities of CFD models are utilized to determine the entropy generated from the CFD computational result and to provide boundary conditions for the reduced order models based on simple control volumes.

Chapter 3

High Impact Technologies Turbine

The Air Force Research Lab (AFRL) designed and tested a highly loaded, high Mach number, 1.5 stage turbine named the High Impact Technologies (HIT) research turbine. The blowdown turbine rig is heavily instrumented with airfoil and flowpath high-frequency static pressure taps, inlet and exit rakes, and heat flux gauges. The turbine design is based on a modern engine cycle and is designed to exhibit a high amount of unsteady interaction between the transonic blading and downstream vane. A significant data set was collected from the test that can be assessed against computational simulations of the design.

3.1 Test Facility

The HIT research turbine test was conducted in the AFRL's blowdown facility at Wright Patterson Air Force Base (WPAFB) pictured in Figure 2-1. The facility is capable of testing a full-size rig for a blowdown period of more than six seconds. Figure 3-1 is a schematic of the rig.

Heated nitrogen is the test medium, and vacuum tanks are used to increase the pressure ratio and prolong the blowdown period. An eddy current brake controls the corrected speed during the blowdown.

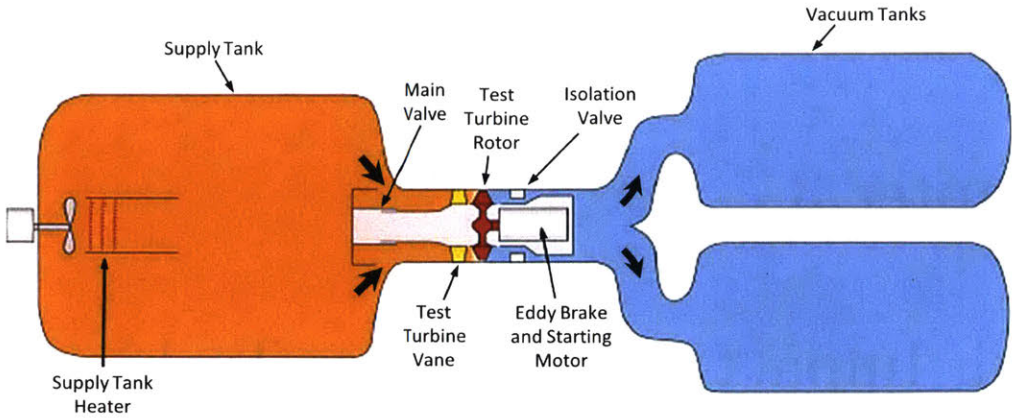

Figure 3-1: Schematic representation of the blowdown rig facility at WPAFB. [14]

3.2 Turbine Design

The HIT research turbine is a highly loaded transonic 1.5 stage design. The airfoil rows are an NGV (1V), blade (1B), and downstream vane (2V). Figure 3-2 shows a midspan section of the turbine airfoils with the velocity triangles for reference.

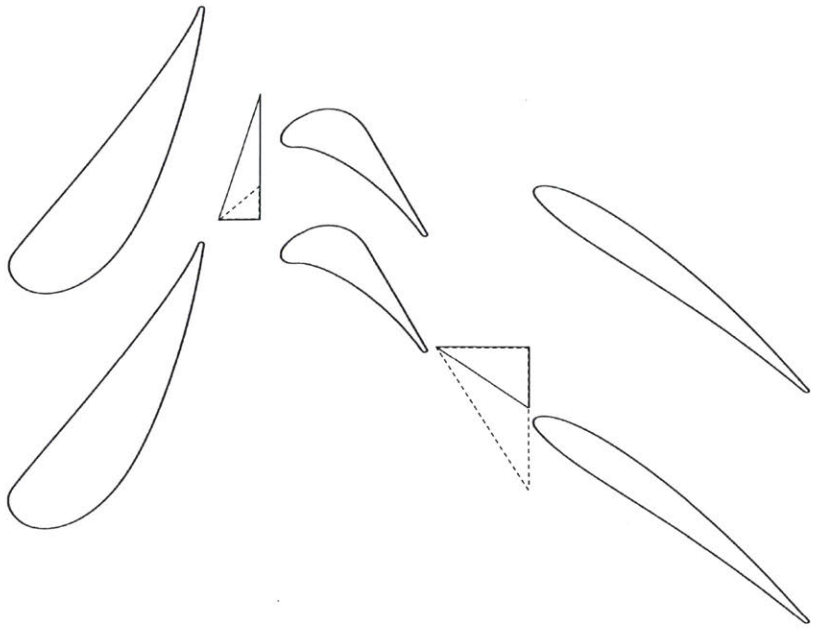

Figure 3-2: Mispan section of the 1.5 stage HIT turbine. Solid lines represent absolute velocity vectors and dashed lines represent relative velocity vectors.

The HIT turbine is a highly loaded design with a Zweifel coefficient of 1.13 [14]. The turbine speed is also high, with a tangential tip Mach number, M_T, equal to about 0.8. These design characteristics enable high work extraction in a single stage. The work coefficient is 2.1, larger than a typical value of 0.9-1.1 for maximum efficiency [16]. High blade turning and a large stage pressure ratio lead to a high exit relative Mach number. The design point exit Mach number for the HIT turbine blade is 1.3. The downstream vane performs little turning since it is designed for use with a counter-rotating low pressure turbine. Table 3.1 is a complete list of the turbine design parameters [14].

Table 3.1: HIT turbine design parameters, comparing the engine and test rig designs. The exit Mach number, work coefficient and blade turning are high compared to a traditional turbine stage. [14]

Parameter	**Engine**	**Rig**
Fluid	Air	N_2
Inlet Total Temperature (K)	1,961	444
Inlet Total Pressure (MPa)	4.05	0.69
Wheel Speed (rpm)	16,000	7,617
Mass Flow (kg/s)	101	37
Power (MW)	57	4.7
Work Coefficient	2.10	2.08
Flow Coefficient	0.73	0.71
Reaction (%)	49.5	49.5
Annulus Area x Wheel Speed^2 x 10^{-6} (m^2rpm^2)	37	8.4
(Inlet Total) Gas-to-Wall Temperature Ratio	1.36	1.36
(Inlet Total) Coolant-to-Wall Temperature Ratio	0.74	0.74
Pressure Ratio	3.63	3.75
Speed Parameter (rpm/$K^{1/2}$)	361	361
Ratio of Specific Heats	1.3	1.4
Prandtl Number	0.70	0.71
Blade Exit Reynolds Number x 10^{-6}	1.34	1.43
Blade Exit Mach Number (Local)	1.30	1.30
Blade Exit Mach Number (Isentropic)	1.45	1.45
Blade Turning (degrees)	115.4	115.5

3.3 Instrumentation

The rig is equipped with stationary and rotating instrumentation. There are over 900 pieces of instrumentation on the rig. These include inlet and exit stagnation pressure and temperature rakes, static pressure taps, and heat flux sensors. High-frequency pressure taps (Kulites) are on the cooled NGV airfoils, cooled rotating blades, and uncooled downstream vanes. There are also high-frequency pressure taps on the downstream vane row endwalls between airfoils. The cooling flows are controlled by two independent circuits with venturis for accurate flow measurement. The corrected speed is controlled to be constant during the blowdown period. Figure 3-3 is a cross section of the HIT turbine showing the position of the inlet and exit rakes.

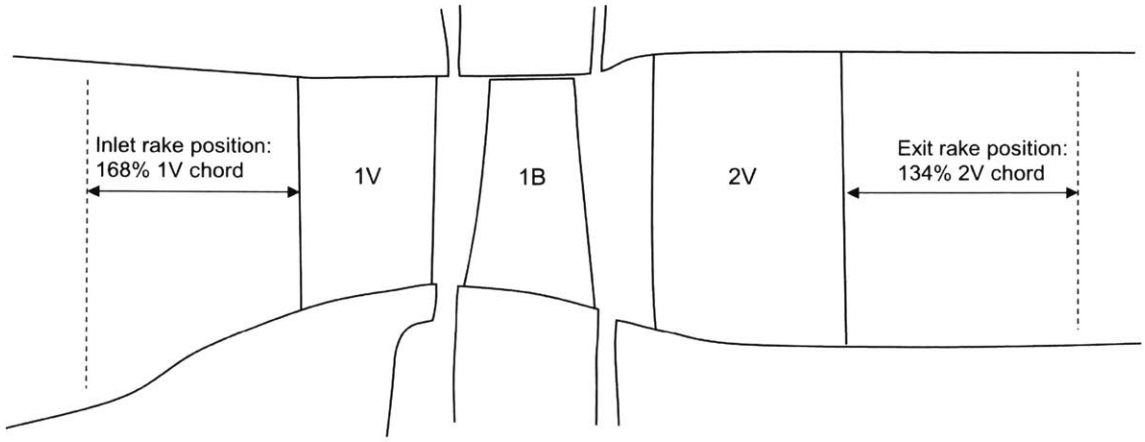

Figure 3-3: HIT turbine cross section with inlet and exit rake positions.

Four traversing rakes, two at the inlet and two at the exit, sweep a total of 120 degrees during the blowdown period. Each rake has nine stagnation pressure and temperature sensors spaced at radial positions of equal annulus area. The area average and time average of this data is used to determine the turbine loss and to set the boundary conditions for CFD analysis.

3.4 Cooling Flow

The HIT research turbine has cooled airfoils on the first vane and blade rows. The cooled airfoils are mixed with uncooled airfoils for the test. The first vane row has 16 cooled airfoils and 7 uncooled airfoils. The blade row has 34 cooled airfoils and 12 uncooled airfoils. The cooled airfoils are not distributed evenly around the annulus; however, the 120 degree traverse of the rakes captures the average loss for the turbine. Figure 3-4 [15] is a map of the first vane and blade configuration. The uncooled airfoils are grouped together on the first vane row and they are distributed in groups of two on the rotor. Heat flux gauges and thermocouples are applied to cooled and uncooled airfoil surfaces.

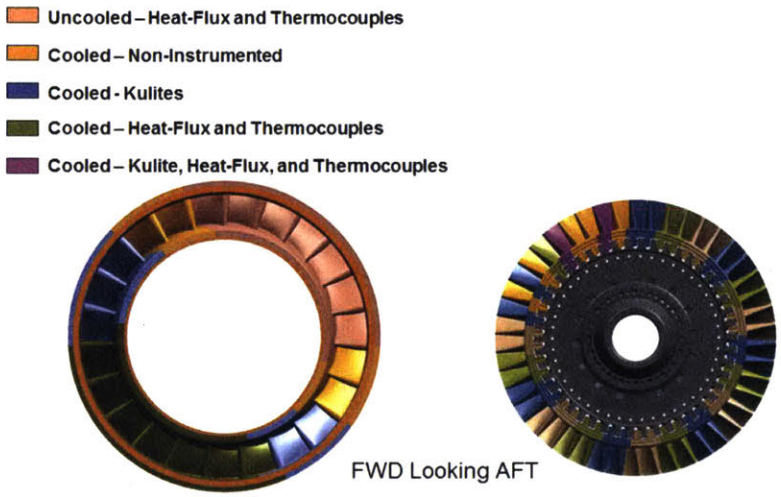

Figure 3-4: HIT turbine first vane and blade cooling schematic. The cooled airfoils are not distributed evenly around the annulus. [17]

Two source plenums feed the cooling circuits. The outer diameter tank feeds the vane outer band, vane trailing edge cooling, and blade outer air seal (BOAS) purge. The inner diameter tank feeds the vane inner band, vane leading edge circuit, rim purge, and blade cooling. Figure 3-5 shows the cooling flow circuit. A complete description of the cooling flow design and configuration is found in Ooten [15].

During the HIT turbine blowdown periods assessed, the flow rate measured through

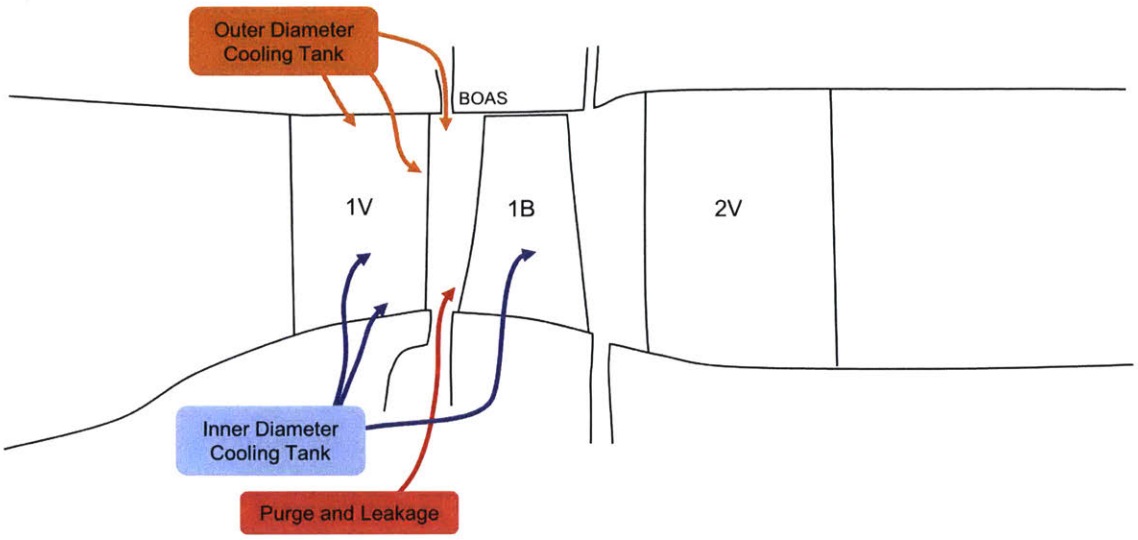

Figure 3-5: HIT turbine cross section identifying cooling and purge flow sources. The vane is cooled by two separate sources through leading edge and trailing edge plenums. The blade cooling flow has the same source as the vane ID band and leading edge plenum cooling flow.

the outer diameter tank venturi was 90% higher than the design intent, and the flow rate measured through the inner diameter tank venturi was 69% higher than the design intent. The mass flow rate of cooling air is assumed to flow through the blades and vane cooling circuit with the design intent proportions, but it is scaled up to match the higher flow rate measured on test. This additional cooling flow is accounted for in calculating the experimental stage loss and also modeled in the cooled CFD assessment. The test hardware is shown in Figure 3-6. Airfoil cooling holes are visible on the first vanes and blades, and heat flux gauges are seen on the rotor blades.

Figure 3-6: The HIT research turbine test hardware: nozzle guide vane (top left), blade wheel (top right), and downstream vane (bottom). [17]

3.5 Summary

The HIT turbine testing carried out at the AFRL is crucial to the understanding of highly loaded transonic turbine aerodynamics. The testing provides a reference point for the CFD results presented in this paper and gives confidence in the loss accounting models. The instrumentation on the rig is numerous and provides all the data required to assess the results of unsteady CFD simulations.

Chapter 4

Computational Framework

Computational Fluid Dynamics (CFD) analysis is used in this research to determine the individual loss components in the turbine stage. The CFD results are assessed against the experimental data to ensure the computation is representative of the flow physics. The computed flow field is then used for deriving flow parameters required in control volume models for loss estimation.

Several levels in physical and geometrical complexities of CFD models are formulated and implemented of flow in the turbine stage. 2D models of the midspan geometry are created to evaluate 2D flow mechanisms and provide a baseline for 3D analysis. The 2D computation resources requirement is significantly less, providing an advantage for effectively evaluating design and modeling changes. 3D models are created for a multistage simulation. The 3D multistage simulation has been implemented on a steady and unsteady basis. This gives insight into unsteady loss generating mechanisms and their contributions to overall loss. The 3D CFD analysis is also performed with and without cooling and purge flow, allowing for isolation of cooling and purge flow losses. These various CFD models are applied as needed to achieve the research goals.

The CFD software is a General Electric proprietary code called TACOMA. This is an in-house developed code with a second order finite volume scheme. A multi-grid algorithm is used to improve solution convergence rate. The RANS simulations are solved computationally on structured grids with a k-ω shear-stress transport (SST)

turbulence model. The grid is resolved down to the wall with a $y^+<1$, and wall functions are not used in order to fully resolve the boundary layer. TACOMA's unsteady RANS (URANS) capability is used for the unsteady calculations. TACOMA benefits from over 20 years of development and use on gas turbine applications and is well suited for addressing the research issues posed in Chapter 1.

4.1 2D Analysis

The initial simulations implemented are for a 2D section. The section described here is a blade midspan section that is the same geometry as the cascade test. Figure 4-1 shows the blade midspan section and the domain for the 2D analysis.

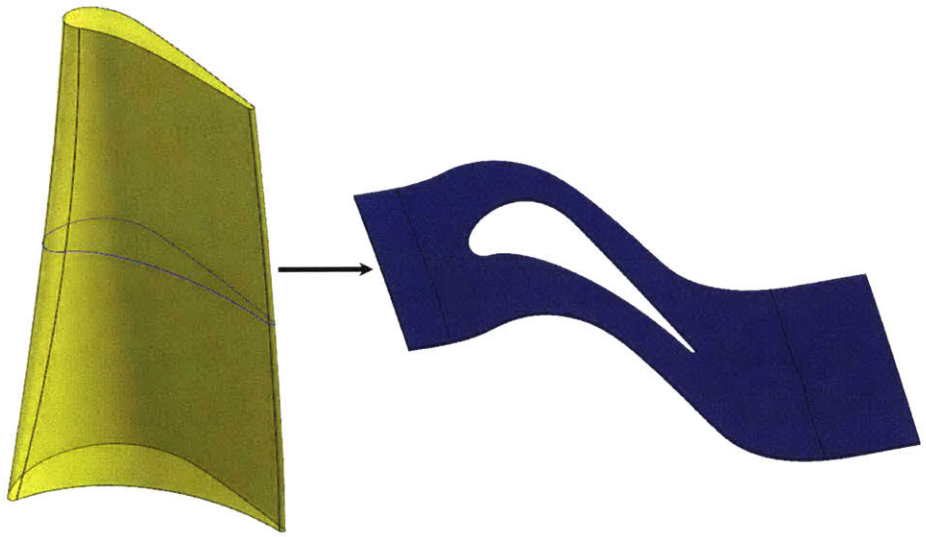

Figure 4-1: Geometry of blade midspan section for cascade analysis.

The grid is generated with Autogrid software. The domain extends by more than 50% of the airfoil axial chord upstream and more than a full axial chord downstream. In the cascade test, the exit rake is located at 68% axial chord downstream of the trailing edge, so this domain is able to be assessed at the rake location for a direct comparison to test data. Three grids are created initially to demonstrate suitable grid independence. The number of nodes in each grid is listed in Table 4.1.

Figure 4-2 is the total entropy generated for each of the grid sizes. There is a 1.9%

Table 4.1: 2D Grid Independence

Grid	**Number of Nodes**	**Entropy Generation** ζ
Coarse	39,300	0.0416
Medium	56,300	0.0408
Fine	115,000	0.0409

difference in overall entropy generation between the coarse and medium grid size, and a 0.2% difference between the medium and fine grid size.

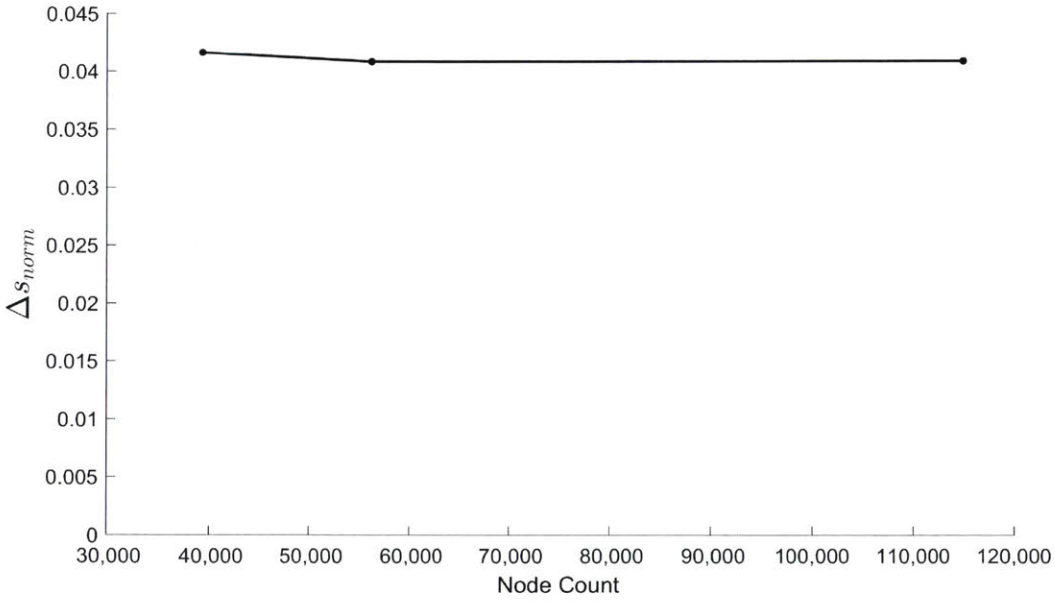

Figure 4-2: Grid resolution convergence of steady 2D analysis.

Adequate grid independence is achieved for the medium grid; however, the coarse grid is utilized for this thesis. This will introduce an error of less than 2% in the overall result, but the benefit of needing lesser computational resources for each assessment allows for increasing the number of computations so that a broad spectrum of relevant flow situations can be examined. This is especially important for the full 3D analysis. The coarse grid density allows a multistage grid count of 9,300,000 nodes, whereas the medium grid resolution would require 19,000,000 nodes with a consequential step change in required computational resources.

The airfoil loading of the 2D CFD result is compared against the uncooled cascade test data in Figure 4-3. The test data is from static pressure taps on the airfoil surface. There is a good agreement between the CFD result and the test data. The pressure fluctuation through the suction side shock system is captured in the CFD model and the leading edge pressure distributions agree. This indicates the incidence angle in the CFD model closely matches the nominal test value.

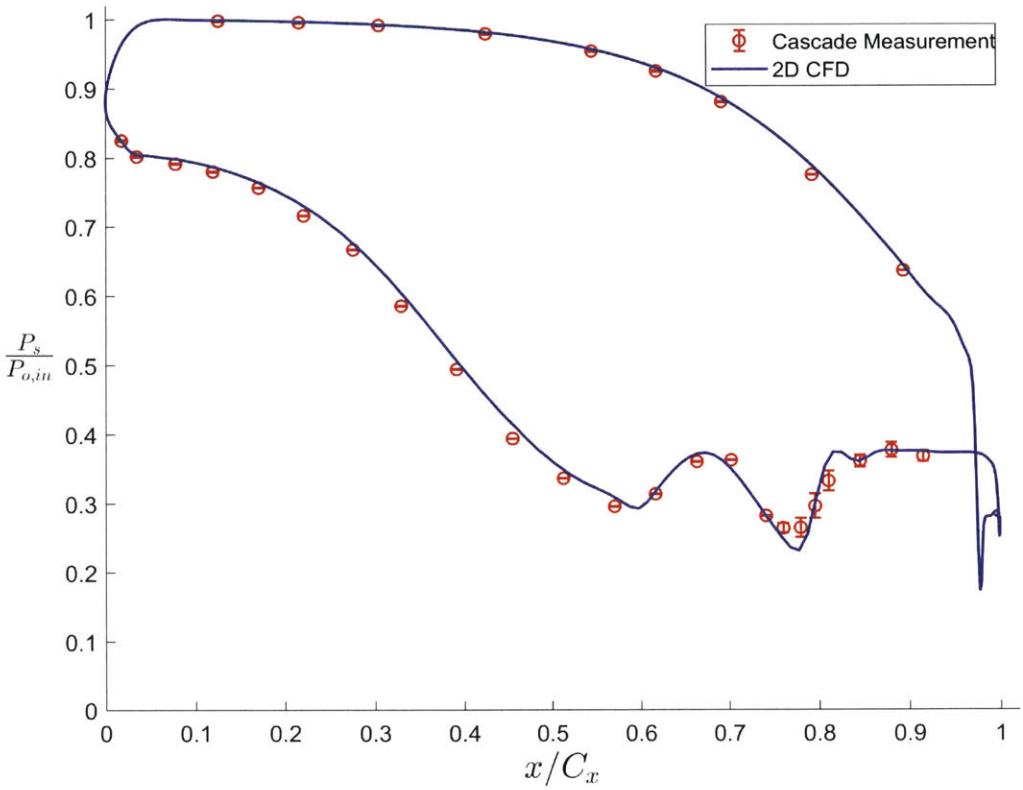

Figure 4-3: Surface static pressure comparison between 2D analysis result and cascade test data.

4.2 3D Analysis

Upon completing the post-processing and analysis of the 2D computed flows, 3D models are created for each airfoil row. Figure 4-4 shows the 3D blade domain for CFD analysis that is created from the airfoil geometry. The 3D blade grid has a root

fillet and tip gap that matches the hardware tested on the blowdown rig. The first vane has root fillets modeled at the ID and OD endwalls. The second vane does not have fillets modeled since it is able to be rotated on test and has sharp corners at the interface between airfoil and endwall surfaces.

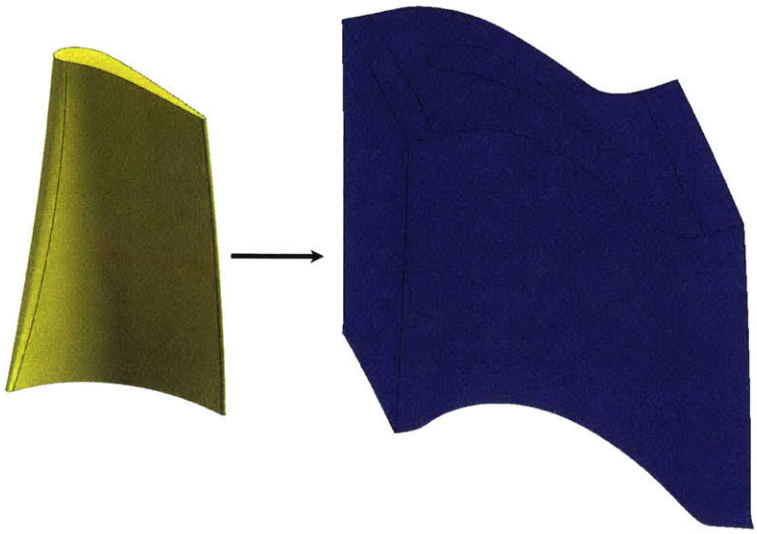

Figure 4-4: Geometry of blade domain for 3D analysis.

The models are built with grid densities that are consistent with the 2D coarse grid density. The grids are again generated with Autogrid. Each individual airfoil domain is converged with uniform inlet and exit boundary conditions. Stagnation temperature, stagnation pressure, radial flow angle, and tangential velocity are prescribed at the inlet plane. Static pressure is prescribed at the exit plane.

4.3 Multistage Steady Analysis

Figure 4-5 depicts the full layout of the 1.5 stage turbine with three 3D airfoil domains. The airfoil domains are split at the midpoint (where the mixing plane is located) between the upstream trailing edge and downstream leading edge. The steady multistage analysis uses a mixing plane algorithm to pass boundary conditions between airfoil rows. Mass, momentum, and energy flux are conserved across the mixing plane boundary.

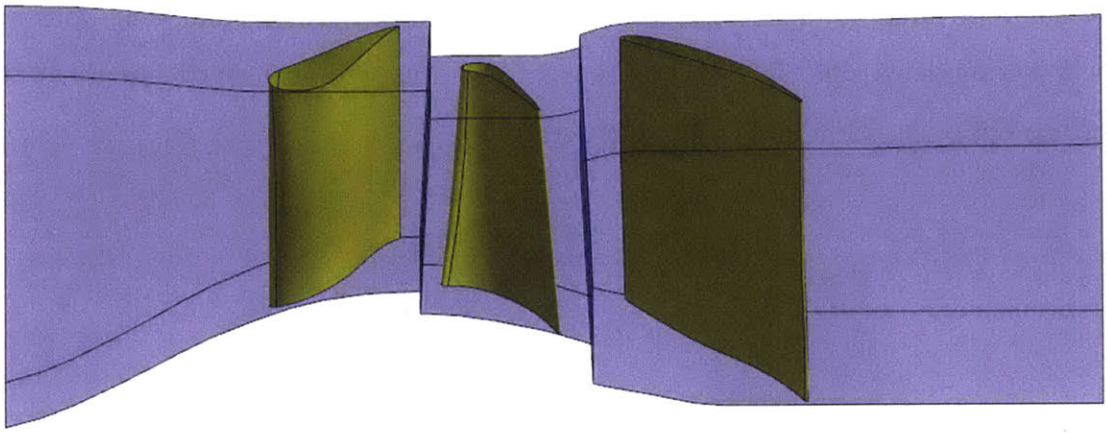

Figure 4-5: 3D multistage CFD domains with mixing plane interfaces between airfoil rows.

Additional models of the first vane (1V), blade (1B), and second vane (2V) airfoil rows are created with an exit domain extended well past the multistage domain exit. The walls of the extended region are modeled as slip walls. Figure 4-6 compares the 1V extended and multistage domains. Figure 4-7 compares the 1B extended and multistage domains. Figure 4-8 compares the 2V extended and multistage domains. The extended domain models are used to calculate the mixing loss downstream of the multistage domain exit. Since the multistage exit is close to the trailing edge, the flow is not fully mixed out. The control volume models for loss estimation assume a fully mixed out exit condition, therefore, a fully mixing out CFD model is needed for a back-to-back comparison. The downstream mixing loss for each airfoil row is presented in Chapter 6.

The blade midspan section pressure distribution from the multistage analysis is different than the cascade test pressure distribution. This is caused by a difference in vane exit flow angle, which translates into blade incidence angle. A 2D CFD analysis confirms this assessment. Figure 4-9 shows the design intent 2D pressure distribution, a pressure distribution from 2D analysis with incidence increased by 12 degrees, and the result from the 3D multistage analysis. A difference of 3.5 degrees of vane exit

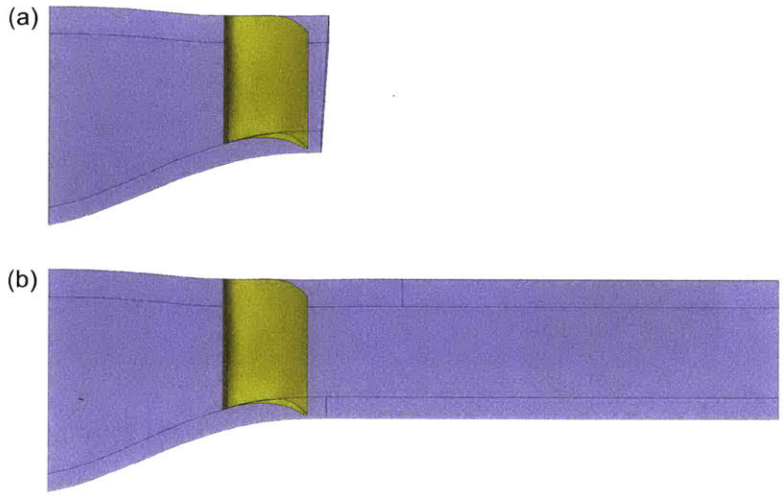

Figure 4-6: First vane (a) multistage domain and (b) extended domain.

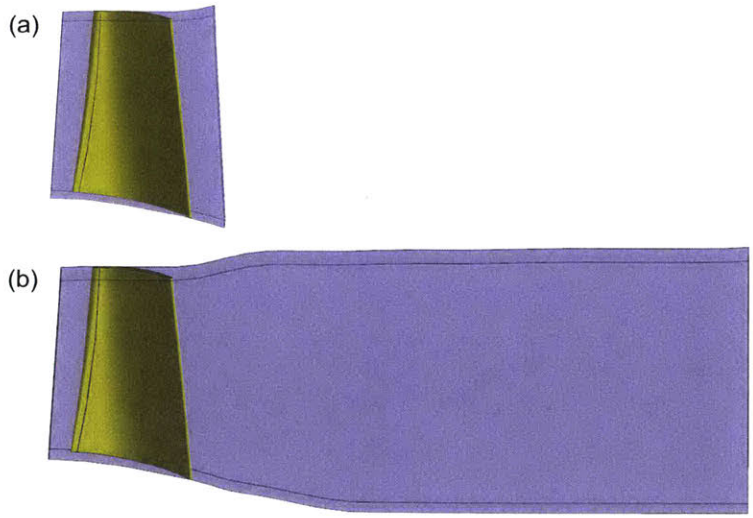

Figure 4-7: Blade (a) multistage domain and (b) extended domain.

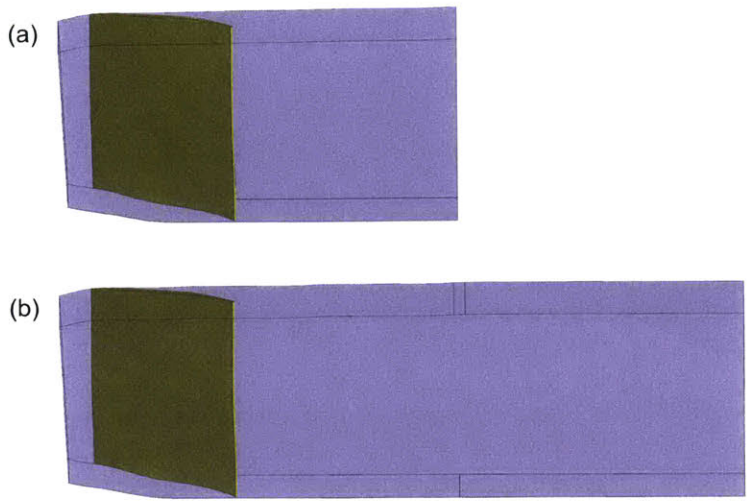

Figure 4-8: Second vane (a) multistage domain and (b) extended domain.

angle results in 12 degrees blade incidence difference. The 2D model with an increased angle of incidence is used to compare loss results with the 3D multistage model.

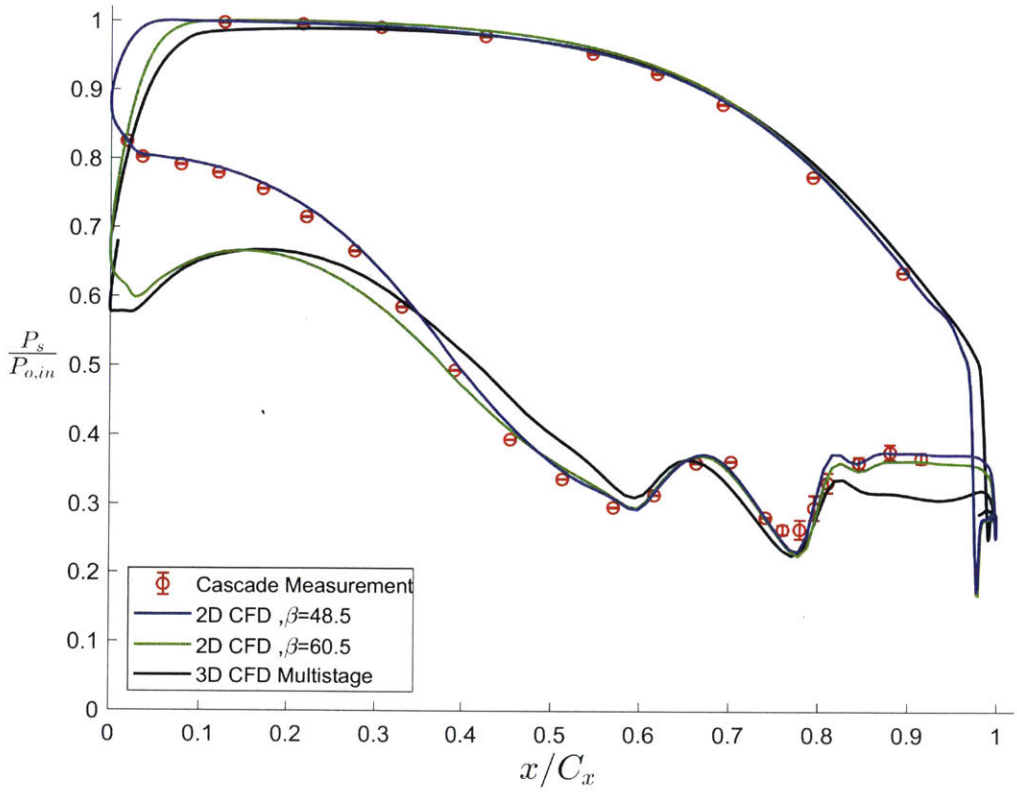

Figure 4-9: 1B midspan static pressure comparison between nominal 2D CFD result, 2D CFD result with increased incidence, 3D CFD result, and cascade test data.

4.4 Cooled Multistage Analysis

The HIT turbine is tested with purge flow and cooling flow, therefore, a CFD model that implements these sources of coolant flows is necessary for a direct comparison to the experimental data. The multistage analysis is expanded by the addition of purge and cooling flow in two steps. The first step is to add the purge flow alone to the simulation. Figure 4-10 shows the full multistage domain and the locations of purge flow. Cool purge flow is introduced with source terms at the hub between the first vane and blade and at the casing upstream of the blade. The hub flow is injected at a tangential velocity equal to 1/2 the rotor hub rotational speed (swirl=0.5) and a meridional angle of 45 degrees. The blade outer air seal (BOAS) flow is injected

radially from the casing. The multistage mixing planes are depicted in Figure 4-10 as lines between the airfoil rows. The hub flow is introduced upstream of the first mixing plane, and the BOAS flow is introduced after the mixing plane.

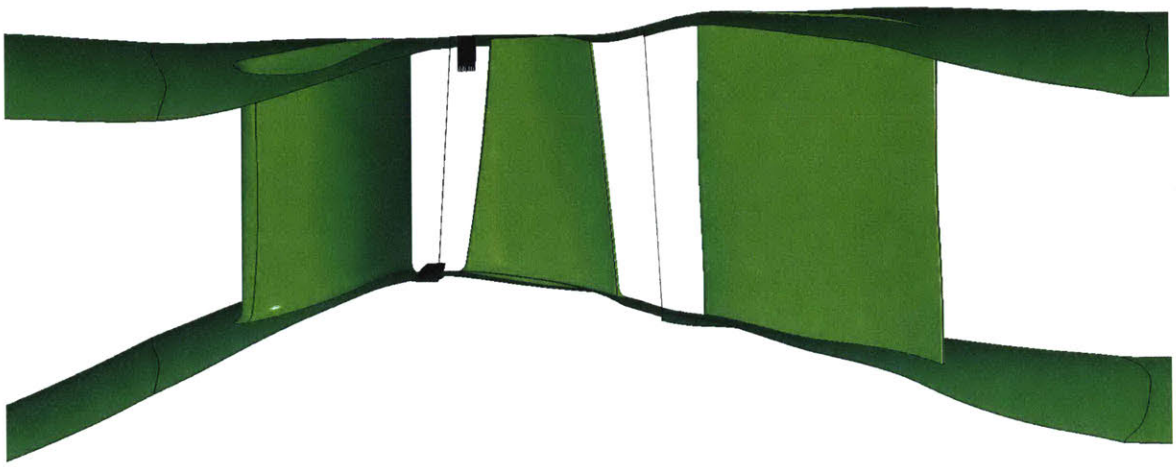

Figure 4-10: The full multistage domain showing the locations of the purge flow injection by the black arrows. The purge flow is introduced on the hub and casing, upstream and downstream of the first mixing plane, respectively.

The purge flow enters the flowpath all around the annulus; however, only a subset of the airfoils are cooled. To analyze the cooling loss from an individual cooled airfoil, a fully cooled stage is modeled as shown in Figure 4-11.

The losses from these two cooled models are combined to account for the ratio of cooled first vane airfoils and cooled blades, and also considering the full annulus purge flow. The amount of flow modeled in this analysis matches the venturi measured cooling mass flow rate from the blowdown test. The cooling flow source temperature and pressure measured from test are also used for the cooling loss calculations.

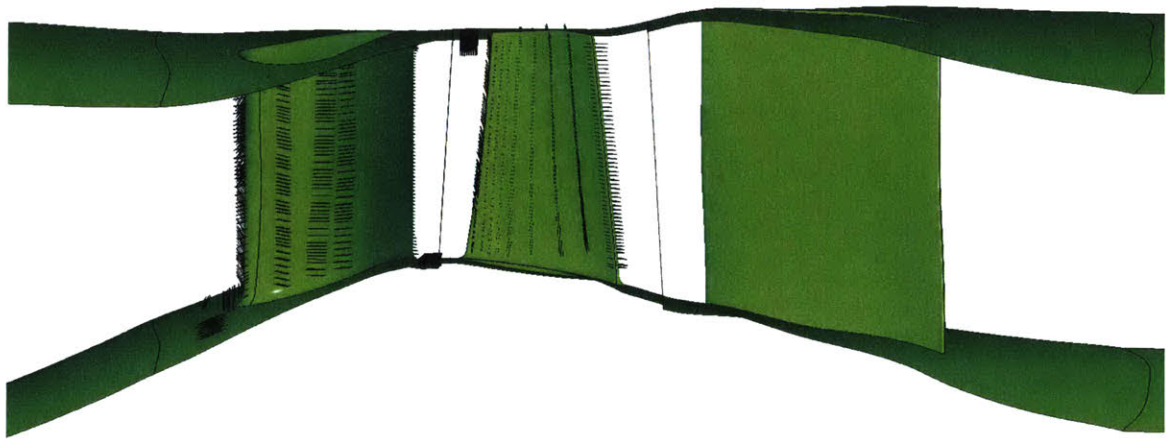

Figure 4-11: The full multistage domain showing the locations of the purge and cooling flow source terms. The purge flow is the same as the previous analysis, and film, band, and trailing edge cooling is added to the first vane and blade.

4.5 Multistage Unsteady Analysis

The multistage unsteady analysis is implemented by specifying a sliding mesh interface between airfoil rows instead of the mixing planes used in the steady analysis. Periodic convergence and time step size convergence are achieved, and the unsteady computation is compared to the high-frequency test data. The results and convergence of the unsteady analysis are assessed by inspecting periodic pressure traces, discrete Fourier transform (DFT) results, and overall entropy generation.

4.5.1 Periodic Convergence

Periodic convergence must be achieved for the unsteady computational solution, defined by convergence of time-averaged inlet and exit temperature, pressure, mass flow, and entropy. The CFD iterations are carried out for 20 to 30 blade passing periods before periodic convergence is achieved. The unsteady analysis is also performed at several time step sizes, and each of these must reach periodic convergence before they can be compared. The periodic convergence of the unsteady pressure field is visualized by comparing two sequential periods of a local static pressure result. Figures

4-12, 4-13, and 4-14 show comparisons for 200, 400, and 1,000 time steps per period for the last two periods of the blade unsteady computation (denoted Period A and Period B). The location of the static pressure trace is the blade suction side location shown in Figure 4-22. Periodic convergence of the unsteady flow computation is achieved for each of the time step sizes. The flow is periodic at the frequency of the stationary vane rows, which have 1/2 as many airfoils as the blade. The vane passing period is 0.353 ms.

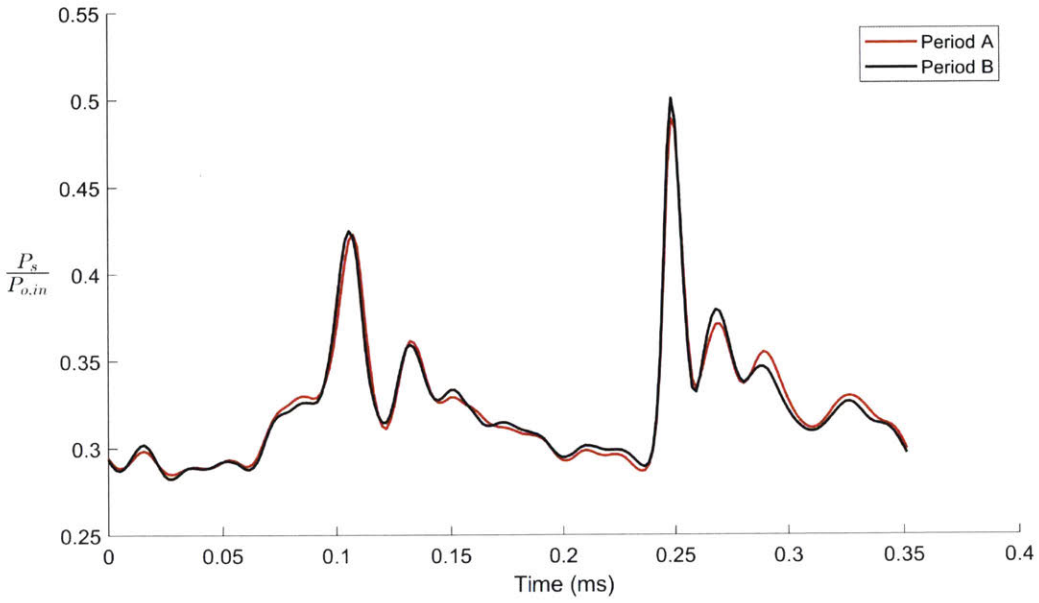

Figure 4-12: 1B periodic convergence - 200 timesteps per period.

Figures 4-15, 4-16, and 4-17 also show comparisons for 200, 400, and 1,000 time steps per period for the last two periods of the 2V unsteady computation (denoted Period A and Period B). The location of the static pressure trace is the endwall location shown in Figure 4-24. Periodic convergence of the unsteady flow computation is achieved for each of the time step sizes. The flow is periodic at the frequency of the upstream blade row, which has 2x as many airfoils as the vane. The blade passing period is 0.177 ms.

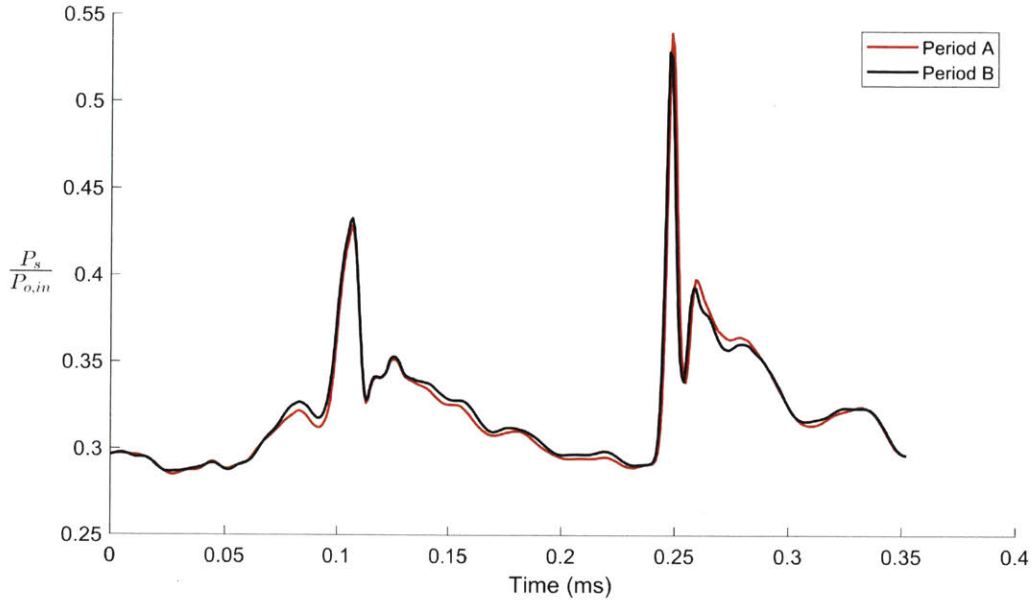

Figure 4-13: 1B periodic convergence - 400 timesteps per period.

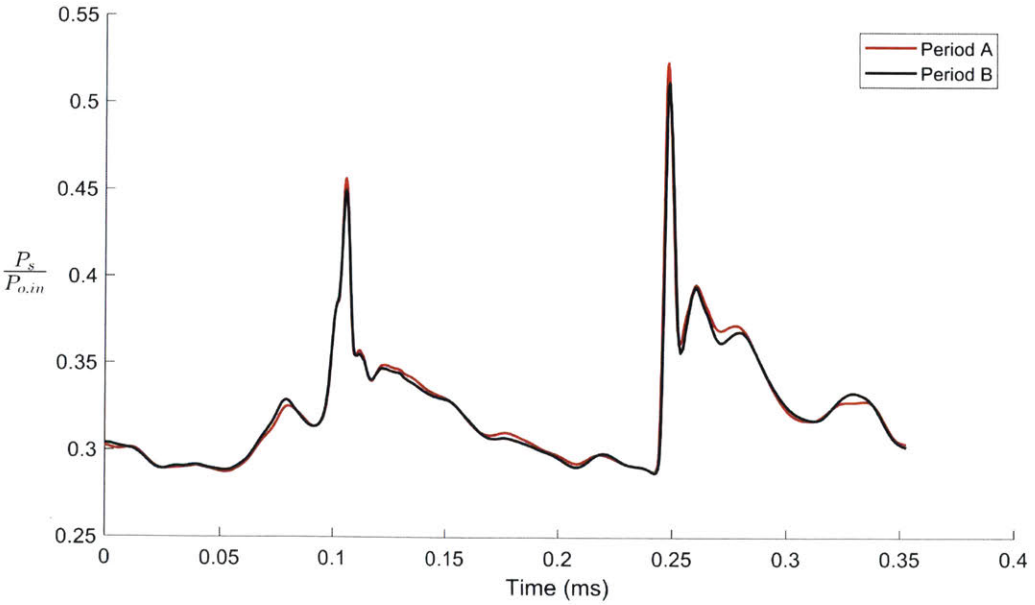

Figure 4-14: 1B periodic convergence - 1000 timesteps per period.

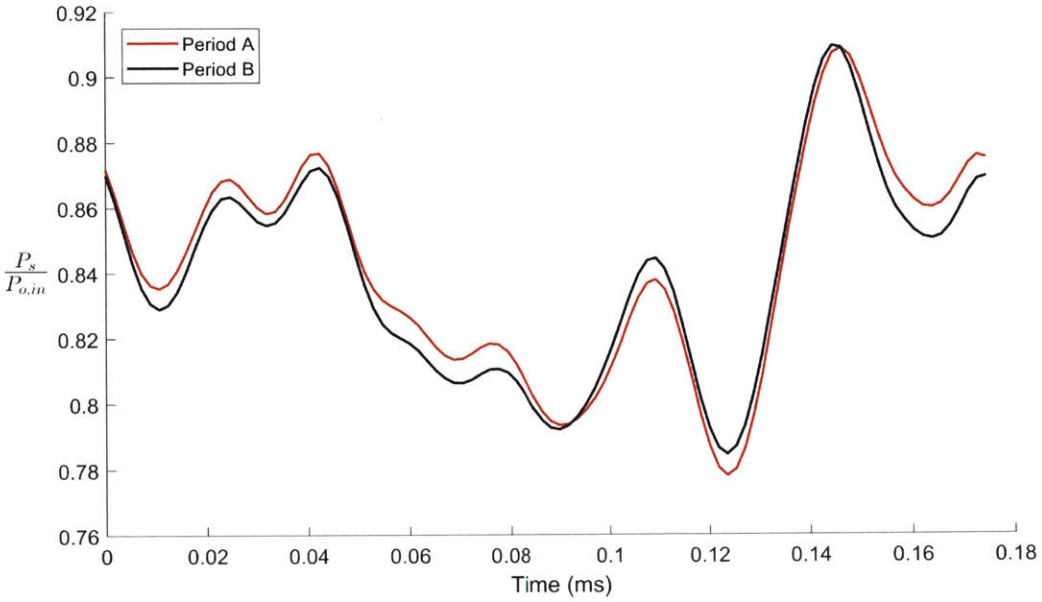

Figure 4-15: 2V periodic convergence - 200 timesteps per period.

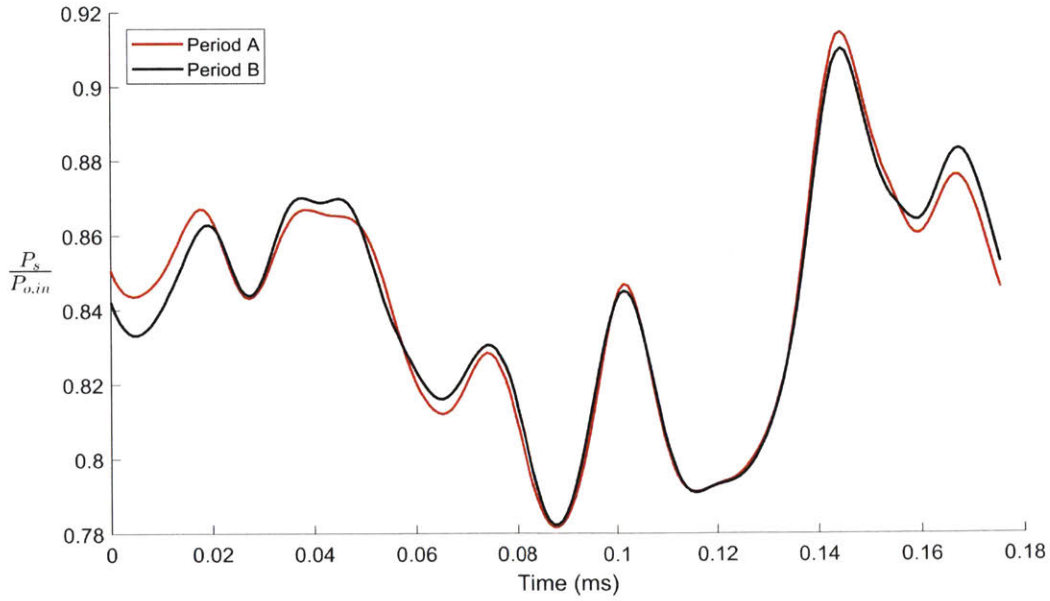

Figure 4-16: 2V periodic convergence - 400 timesteps per period.

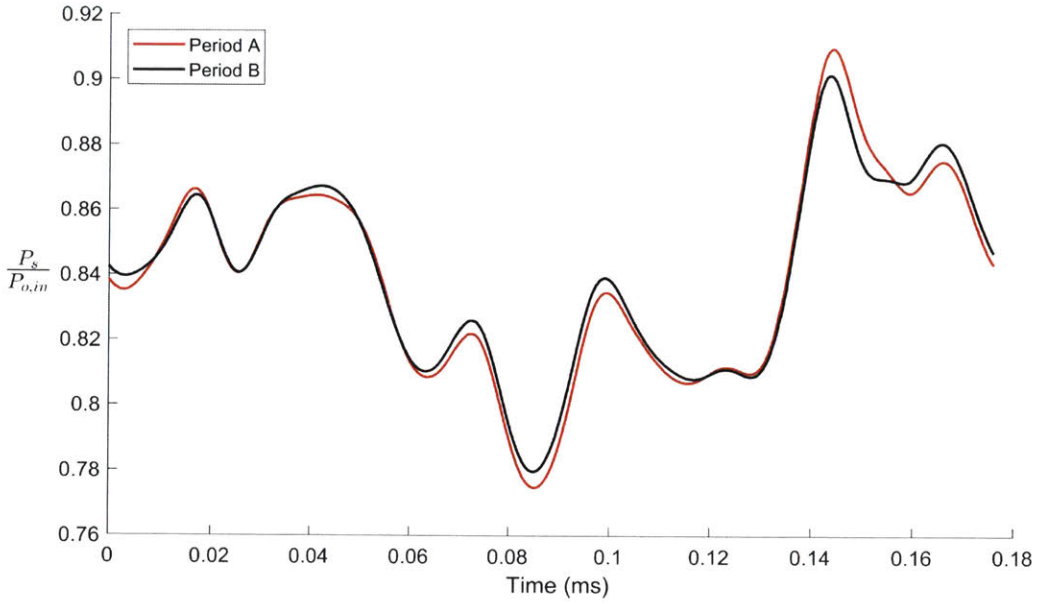

Figure 4-17: 2V periodic convergence - 1000 timesteps per period.

4.5.2 Time Step Size Convergence

A time step convergence assessment is conducted by comparing overall entropy generation for three time step sizes. 200, 400, and 1,000 time steps per period are analyzed. The results of the assessment in Table 4.2 and Figure 4-18 show that there is 0.3% difference in overall entropy generation for the full 1.5 stage domain between 400 and 1,000 time steps per period. A model with 1,000 time steps per period is selected for all the unsteady computations presented in this thesis; however, analysis with 400 time steps is adequate for future assessments to reduce the needed computational resources.

Table 4.2: 3D Unsteady Timestep Independence

Timesteps per Period	**1V** ζ	**1B** ζ	**2V** ζ	**Stage** ζ
200	0.0966	0.3337	0.1379	0.5686
400	0.0948	0.3325	0.1367	0.5644
1,000	0.0941	0.3321	0.1358	0.5625

The static pressure is compared for 200, 400, and 1000 time steps for a location

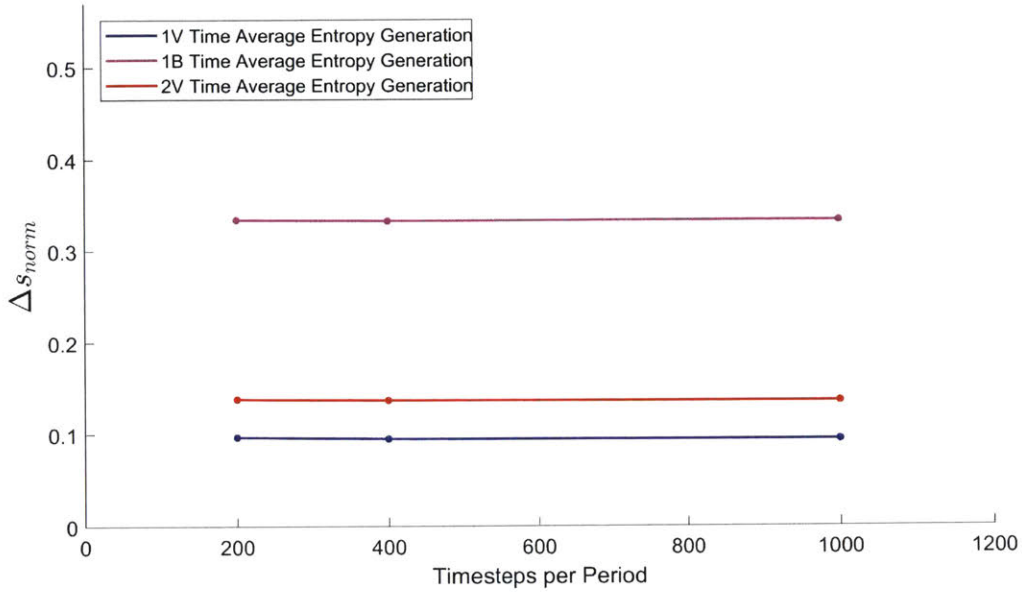

Figure 4-18: Time step convergence of unsteady multistage analysis individual airfoil row entropy generation .

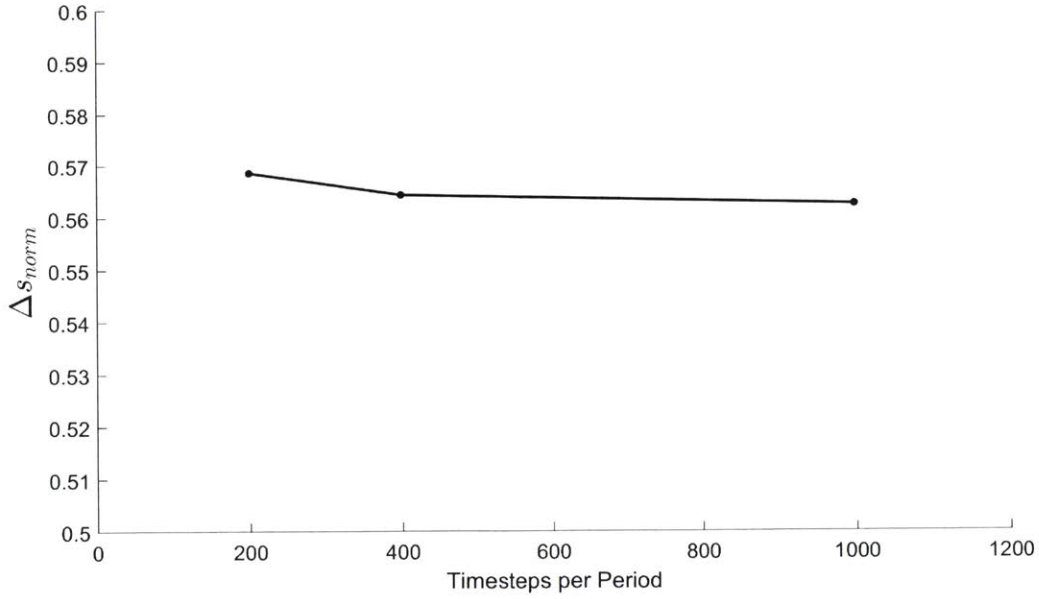

Figure 4-19: Time step convergence of unsteady multistage analysis overall stage entropy generation.

on the blade suction side surface in Figure 4-20, and a location on the downstream endwall in Figure 4-21.

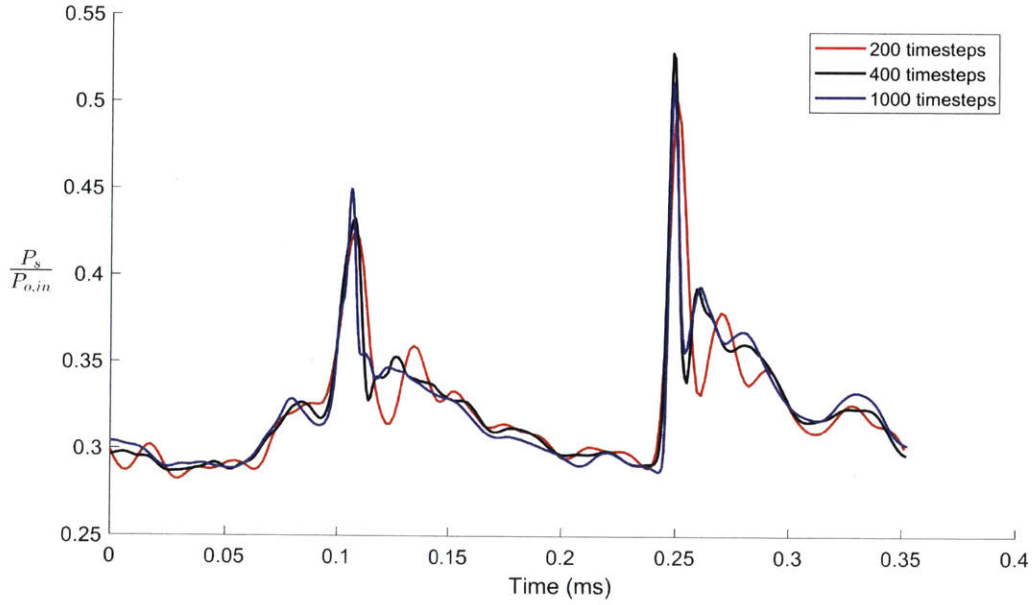

Figure 4-20: Timesteps per period comparison of unsteady pressure trace on the blade surface.

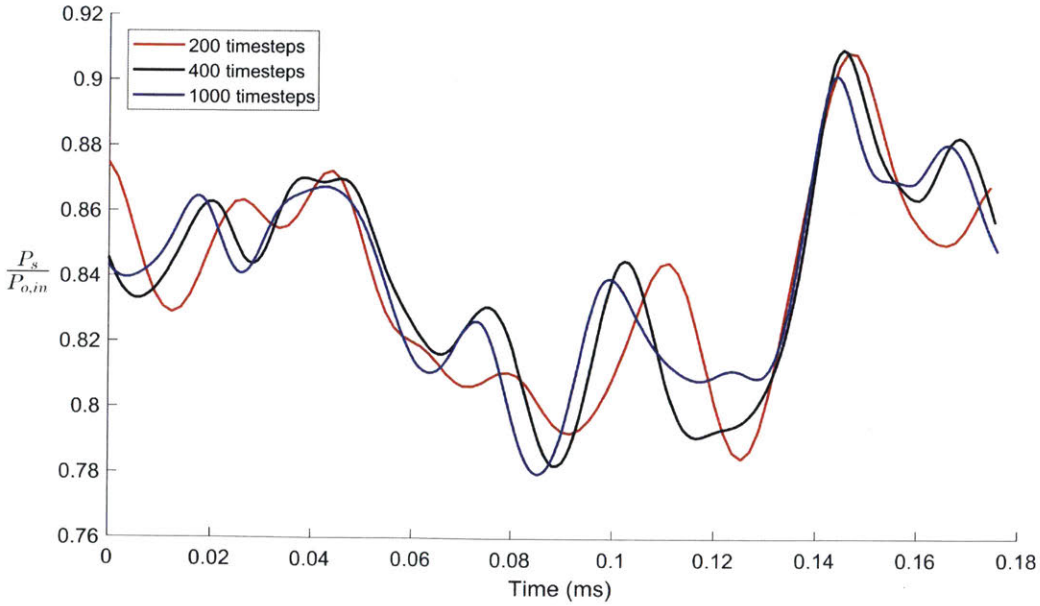

Figure 4-21: Timesteps per period comparison of unsteady pressure trace on the downstream vane hub surface.

The results for 400 and 1,000 time steps per period are comparable and show similar pressure response characteristics. Either solution is acceptable for comparison to the test data or estimating entropy generation.

4.5.3 Comparison of Unsteady Computation and Test Data

The unsteady CFD computational result is compared against the test data by performing a DFT analysis on the time dependent pressure trace. The Kulite locations on the airfoil suction side surfaces are overlaid on a 2D image of the 1.5 stage turbine in Figure 4-22. The contour in Figure 4-22 is the magnitude of the DFT response at a frequency equal to 2x the blade passing frequency. The DFT magnitude results presented here were calculated by the AFRL [17]. High values of DFT magnitude correspond to large static pressure fluctuations.

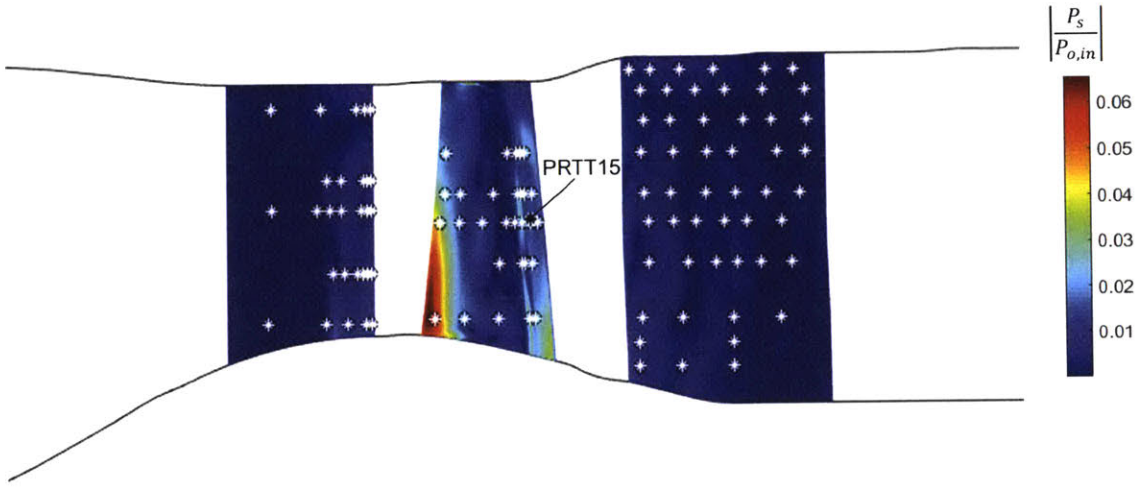

Figure 4-22: Calculated DFT magnitude of the airfoil suction side surfaces, overlaid with the locations of the high-frequency pressure taps on the blowdown rig. Probe PRTT15 is used for the blade suction side pressure comparisons in this thesis.

Computational results are recorded at locations on the CFD domain walls coincident with the location of the Kulites on test. Figure 4-23 is a comparison between the CFD result, unfiltered rig Kulite data, and the cyclically averaged rig data at a location on the blade suction side at midspan near the trailing edge. The test result

frequencies and general trend of signal power magnitude is captured by the CFD result.

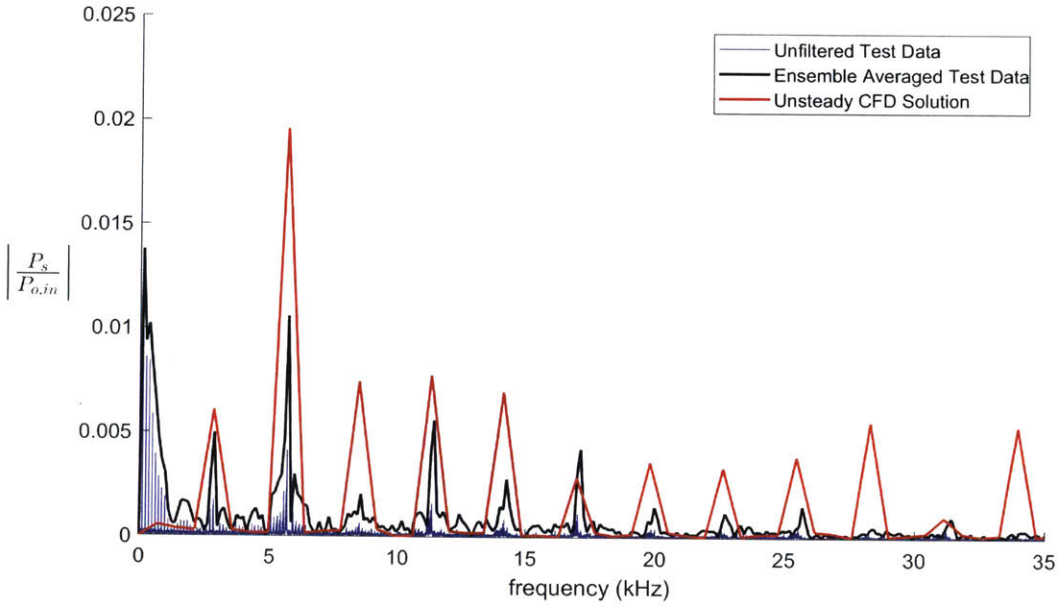

Figure 4-23: DFT comparison between unsteady CFD result and blowdown test Kulite data. The location is on the blade suction side at probe PRTT15.

The largest magnitude DFT response is at twice the vane passing frequency. This is a result of the rotor trailing edge shock reflecting off the downstream airfoil, traveling back upstream, and impinging on the suction side surface. The reflected trailing edge shock creates a large pressure fluctuation at the probe PRTT15 location. This result can also be observed in Figure 4-14, where in one vane passing period two large pressure peaks are observed.

Kulites are also located on the endwalls of the downstream vane row. Figure 4-24 is the magnitude of the DFT response for 2x the blade passing frequency on the inner diameter endwall and also shows the locations of the pressure taps.

The unsteady computational result and experimental data are compared for a location on the endwall near the 2V airfoil leading edge. Figure 4-25 is the DFT response at this location.

The magnitude of the response and frequencies are similar between CFD and test data. In both the CFD computation and test result, the dominant response

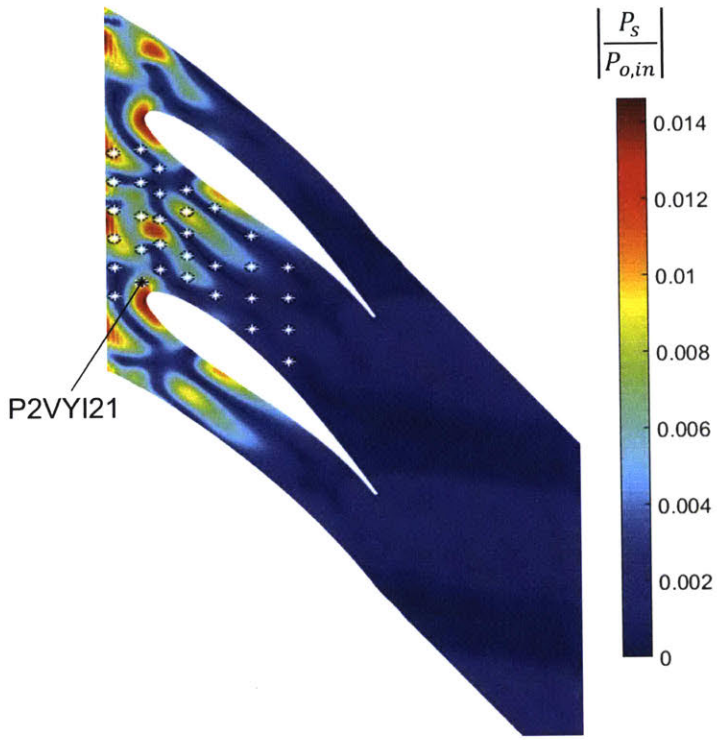

Figure 4-24: Calculated DFT magnitude of the 2V ID endwall surfaces, overlaid with the locations of the high-frequency pressure taps on the blowdown rig. Probe P2VYI21 is used for the 2V endwall pressure comparisons in this thesis.

frequencies are multiples of the blade passing frequency. Also, the value of the 2V endwall DFT response is lower than that on the blade suction side, indicating a lower level of unsteadiness.

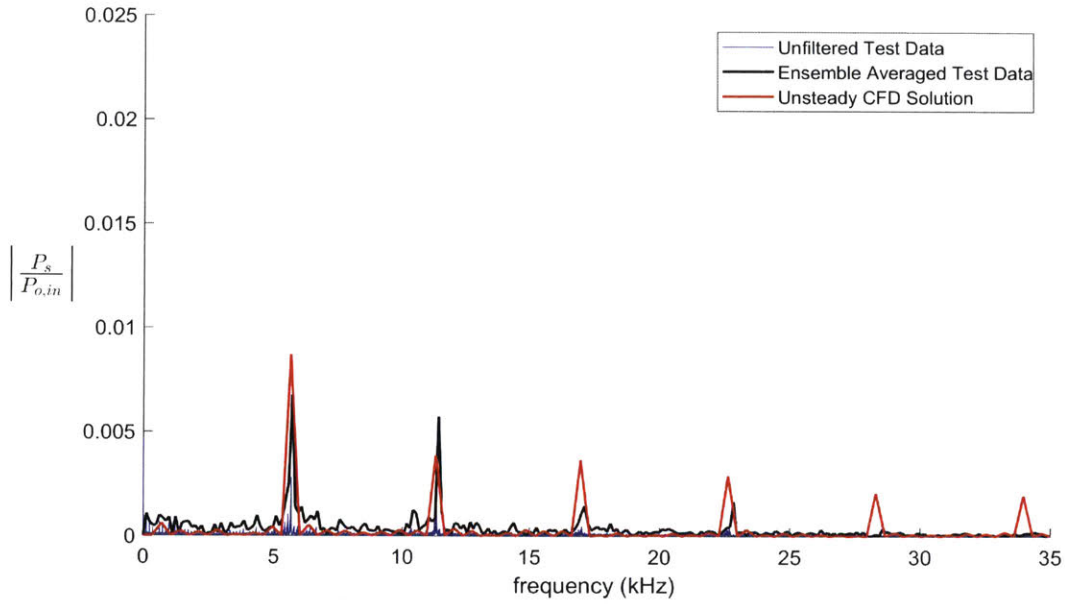

Figure 4-25: DFT comparison between unsteady CFD result and blowdown test Kulite data. The location is on the 2V ID endwall at probe P2VYI21.

4.6 Summary

Various levels in physical and geometric complexities of CFD simulations have been implemented; these include flow situations in a 2D and 3D domain, single stage and multistage, and steady and unsteady. Simulations are implemented with the vanes and blades uncooled and cooled, and with and without purge flow. Both discrete temporal and spatial convergence of the solution were assessed for selecting the appropriate time step size in which computations are to be implemented. The computed results have also been assessed against test data from the AFRL blowdown facility. The computed results and their use in identifying and quantifying various loss mechanisms are described and presented in Chapter 5 that follows.

Chapter 5

Estimation of Sources of Loss

This chapter describes methods for calculating losses in a 1.5 stage turbine. The methods include direct estimation of loss from the CFD computed flow fields and measurements taken in AFRL blowdown test, mixed-out loss estimation, as well as use of known correlations.

Where it is meaningful, a comparison is made between two methods of loss calculation. As discussed in Section 2.1, the loss components in a gas turbine are calculated from the entropy generation caused by the underlying flow mechanism, and the use of stagnation pressure coefficients is avoided. The airfoil row losses are normalized by the exit flow state, shown in Equation 5.1. If the losses are compared across the entire stage, the stage exit condition is used for normalization.

$$\Delta s_{norm} = \Delta s \left(\frac{T_{exit}}{0.5 V_{exit}^2} \right) \tag{5.1}$$

5.1 Experimental Overall Stage Loss Estimation

The loss in the experiment is calculated by comparing the time and area averaged stagnation pressure and temperature of the upstream and downstream rakes. The blowdown test also includes cooling and purge flow, so this must be considered. The mass flow weighted Hartsel turbine efficiency method as described by Young and Horlock [18] is adapted for the cooled stage entropy generation calculation. Equation

5.2 is applied to three flow streams: mainstream flow, inner tank flow, and outer tank flow, and the respective entropy generation is weighted by mass flow rate. The reference condition is the inlet relative stagnation temperature and pressure for each respective stream.

$$s - s_{ref} = C_p \ln\left(T/T_{ref}\right) - R \ln\left(P/P_{ref}\right) \tag{5.2}$$

This method may overestimate the turbine loss if some of the cooling flow is leaked into the test cell instead of entering the main gas path.

5.2 CFD Loss Estimation

The analytical loss is calculated from the CFD models using mass flow averaged flux quantities as described by Zlatinov [8]. Individual airfoil row loss is determined by comparing the entropy flux difference between inlet and exit planes. Entropy in the CFD result is calculated with Equation 5.2, using the inlet relative condition as a reference. Additionally, the entropy generation across an airfoil row is determined by discretizing the CFD domain into axial cut planes and calculating the entropy content at each plane relative to the inlet. The results of entropy generation as a function of x/C_x are in Section 6.2.

Since the flow is not completely mixed out at the exit plane of the shortened multistage domains, the downstream mixing loss is determined from the entropy flux difference between an axial cut plane coincident with the multistage domain exit and the exit plane of an extended slip wall duct section. The domains used for these calculations have been described in Chapter 4. The iterative methodology for calculating mixed out loss described by Prasad [19] was considered; however, the downstream mixing from the CFD domains is used instead for ease of computation. Future work may consider comparing the CFD solution downstream mixing loss result to Prasad's mixed out calculation.

In this thesis, the estimation of trailing edge loss, tip leakage loss, and secondary flow loss using control volume methods [1] [20] assumes the downstream condition to

be fully mixed out. Therefore, to attribute the loss model results (i.e. loss estimated using a control volume approach) to their corresponding CFD domains properly, the CFD result (i.e. loss estimated directly using computed flow) for downstream mixing loss is attributed to the downstream airfoil row and subtracted from the airfoil row's accounting. The downstream mixing components are identified in the loss accounting results in Chapter 6.

The loss in a turbine stage can be qualitatively inspected by calculating the volumetric entropy generation rate [8]. Equation 5.3 [8] is the viscous portion of the volumetric entropy generation rate.

$$\dot{S}'''_{visc} = \frac{1}{T}\tau_{ij}\frac{\delta V_i}{\delta x_j} \tag{5.3}$$

Figure 5-1 is a contour of the viscous entropy generation rate for the entire stage flow field at the midspan section.

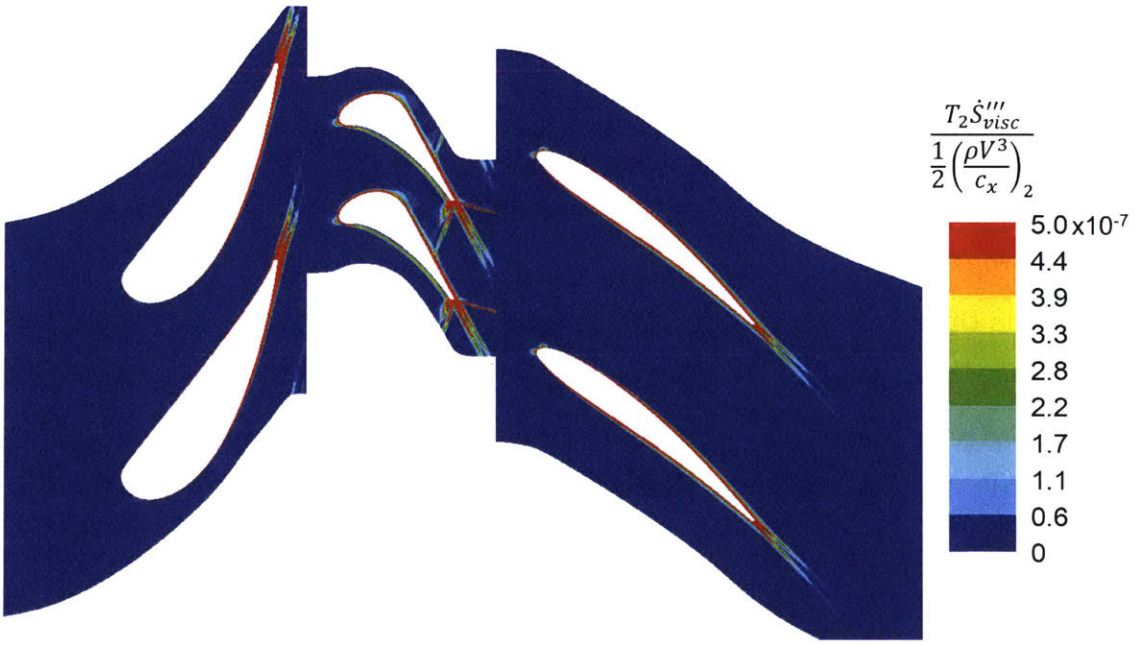

Figure 5-1: Normalized viscous entropy generation rate applied to the entire stage flow field. Boundary layer loss, trailing edge mixing loss, and shock loss are observed.

The boundary layer loss, trailing edge mixing loss, and shock losses are seen clearly. The results show some locations with high viscous entropy generation rate, such as

the downstream vane leading edge, which may be overestimated because of the grid resolution or computational discontinuities. Zlatinov [8] discusses the limitations of using viscous entropy generation rate to quantitatively determine the loss in a turbine; however, it is a useful tool for identifying the locations of loss generation. All losses in this thesis are quantified with Equation 5.2 and control volume models.

5.3 Profile Loss Estimation

Profile loss results from viscous forces in the boundary layer at the airfoil surface. Denton [1] estimates the profile loss is about 1/3 of an airfoil row loss. There are three methods for determining profile loss of an airfoil. The first is to use a constant dissipation coefficient (C_d) of 0.002 [1] across the entire airfoil surface. The second method is to calculate C_d from the Reynolds number correlation for a turbulent boundary layer in Equation 5.4 [1]. The last method is to calculate C_d explicitly from the boundary layer flow properties. This method is explained in detail in this section.

$$C_d = 0.0056 Re_\theta^{-1/6} \tag{5.4}$$

The boundary layer details are determined from the CFD solution by extracting the flow properties at vectors normal to the airfoil surface. Figure 5-2 shows the normal vectors that are applied to the blade. The boundary layer velocity, temperature, and pressure profiles are determined for each of the discretized locations. The boundary layer edge is defined by the boundary layer entropy thickness, δ_s. The entropy profile of the boundary layer is calculated with Equation 5.2 using the free stream condition as a reference.

The edge of the boundary layer is defined when the incremental entropy generation reaches <0.1% of the total entropy contained in the boundary layer. The method is iterative, but the solution converges rapidly. Figures 5-3 and 5-4 show the entropy boundary layer profile and the velocity profile at the suction side trailing edge. The free stream properties are defined at y=δ_s.

Once the boundary layer thickness is determined from the entropy thickness, the

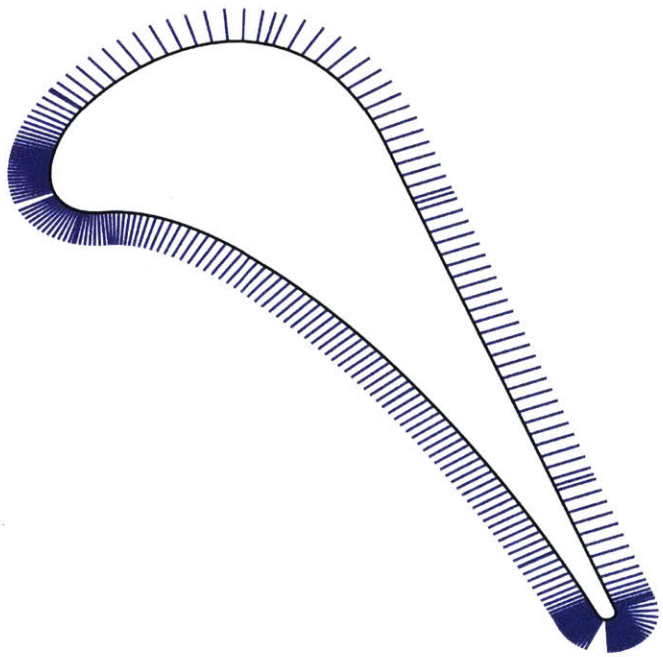

Figure 5-2: Vectors normal to the blade surface.

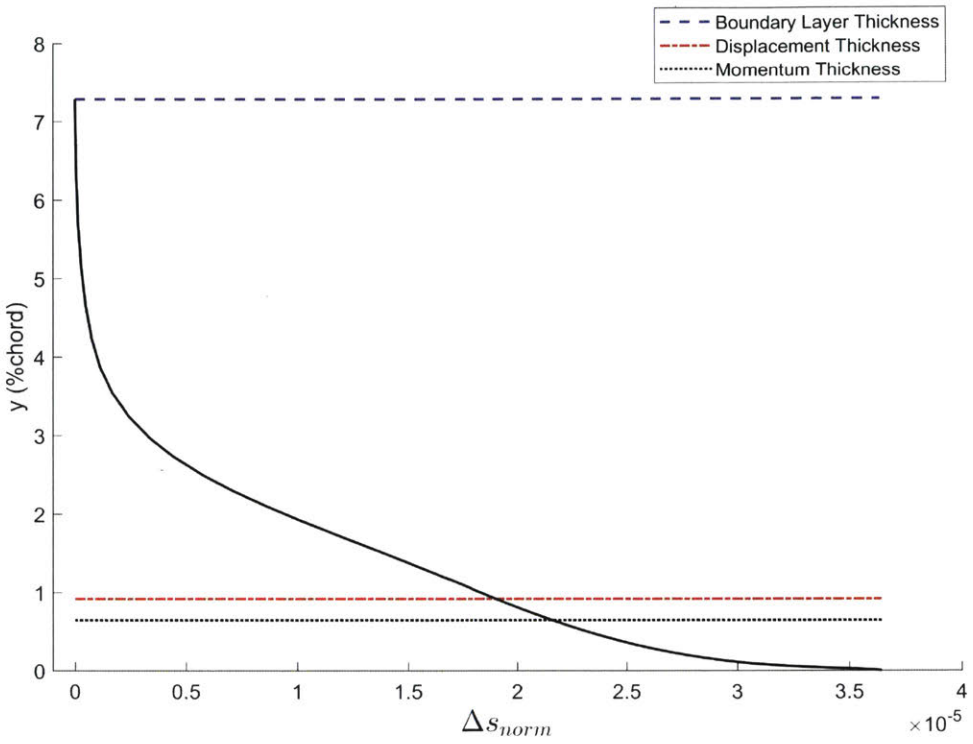

Figure 5-3: Entropy Boundary Layer Profile.

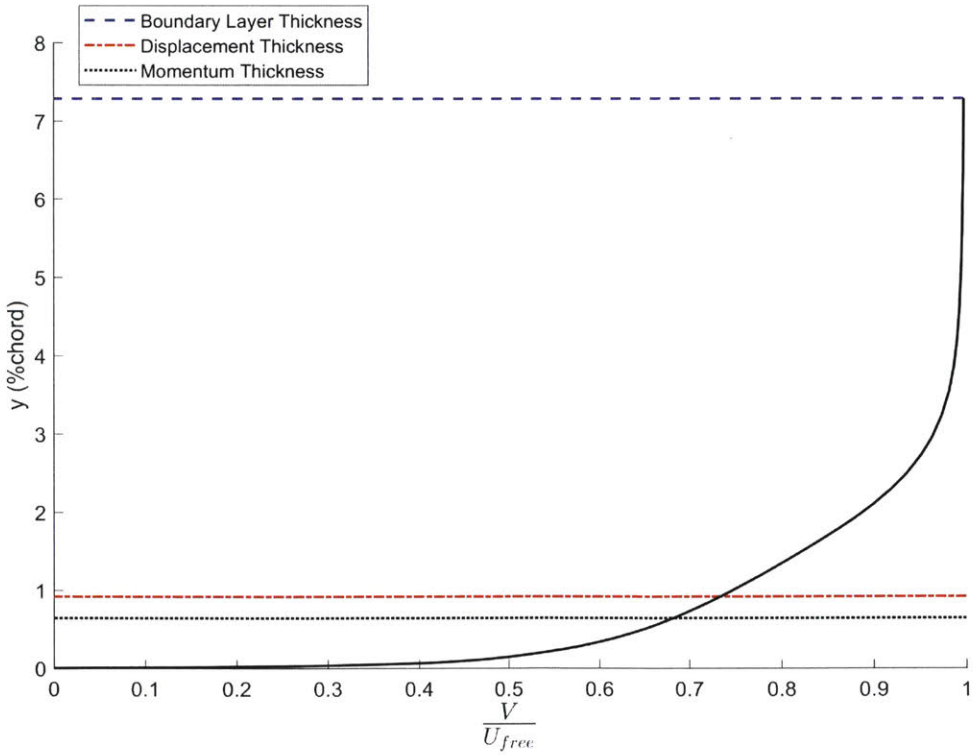

Figure 5-4: Velocity Boundary Layer Profile.

momentum and displacement thicknesses are calculated from the velocity and density profiles by applying Equations 5.5 and 5.6 for compressible flow.

$$\delta^* = \int_0^{y_s} \left(1 - \frac{\rho(y)u(y)}{\rho_s u_s}\right) dy \tag{5.5}$$

$$\theta = \int_0^{y_s} \frac{\rho(y)u(y)}{\rho_s u_s}\left(1 - \frac{u(y)}{u_s}\right) dy \tag{5.6}$$

The momentum and displacement boundary layer thicknesses are shown as a function of axial chord in Figure 5-5.

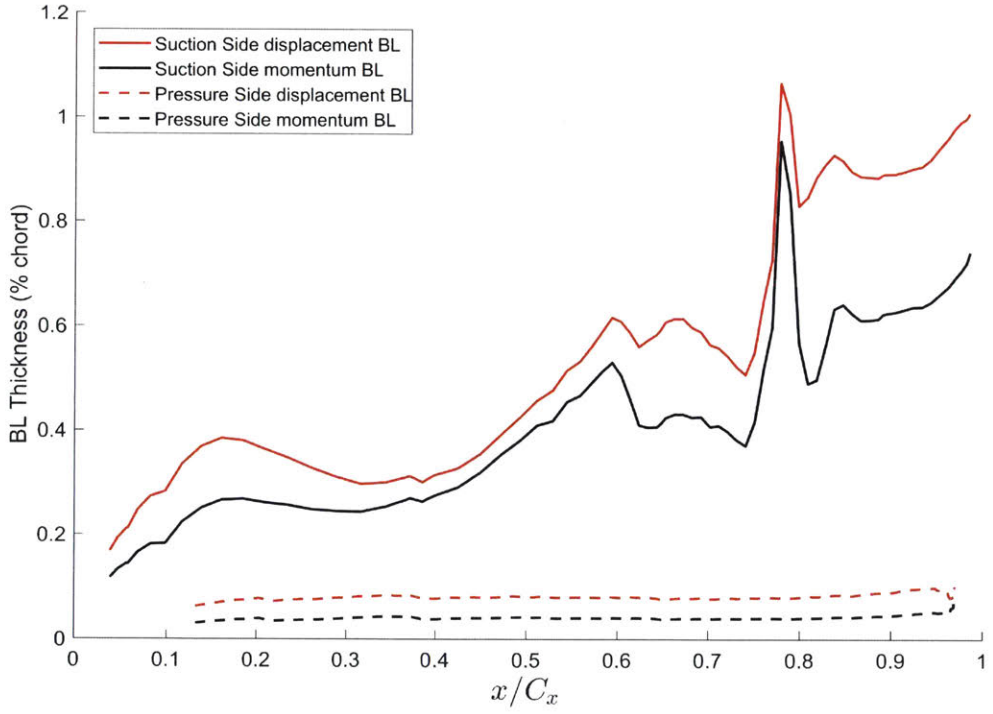

Figure 5-5: Boundary layer thickness as a function of axial chord.

At each position along the chord of the airfoil the entropy content of the boundary layer can be calculated by integrating the entropy profile from the wall to the free stream. The entropy content in the boundary layer relative to the inlet entropy is given by Equation 5.7. Equation 5.8 is the total rate of entropy creation in the airfoil surface boundary layer.

$$S_a = \int_0^{\delta} \rho U(s - s_\delta)\, dy \tag{5.7}$$

$$\dot{S}_a = \frac{d}{dx} \int_0^{\delta} \rho U(s - s_\delta)\, dy \tag{5.8}$$

The entropy content in the boundary layer is shown as a function of axial chord in Figure 5-6. The entropy content is normalized and expressed on a per unit mass flow basis, so the value at the trailing edge ($x/C_x = 1$) is the total entropy generated by the airfoil boundary layer. A sharp rise in entropy generation rate is observed at the location on the suction side around 80% chord where the trailing edge shock from the adjacent airfoil impinges.

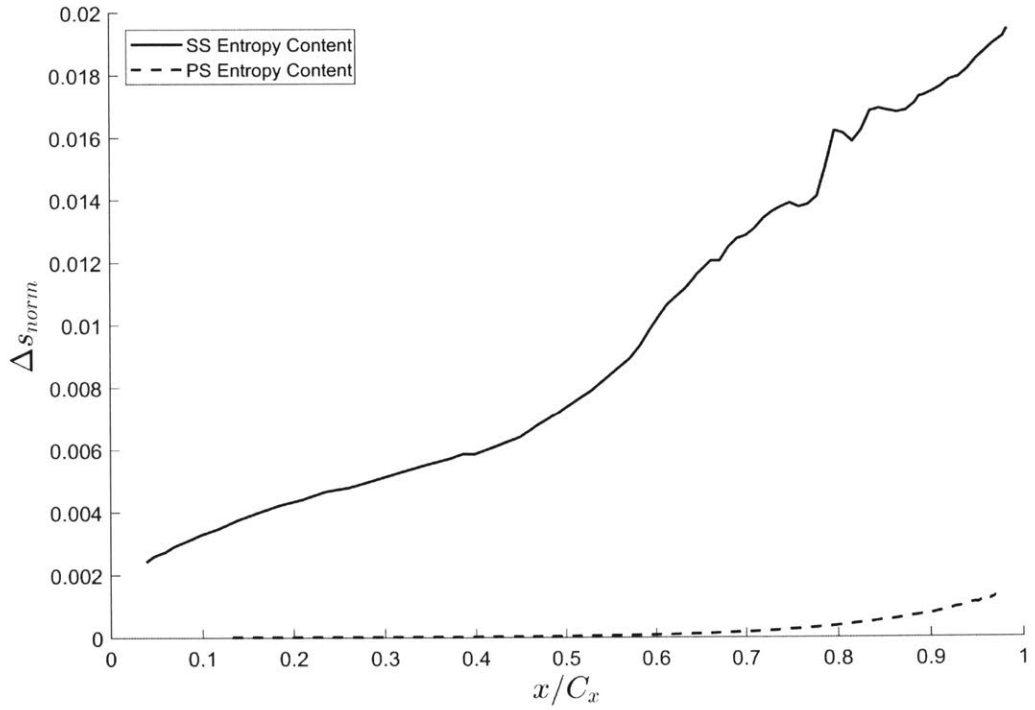

Figure 5-6: SS and PS entropy content in the boundary layer.

An analytical dissipation coefficient is calculated from the boundary layer entropy creation rate. Equation 5.9 is the definition of C_d. The analytical C_d depends on local entropy creation rate, and is compared to the value for C_d proposed by Denton [1] of 0.002 in Figure 5-7.

$$C_d = \frac{T\dot{S}_a}{\rho V_\delta^3} \tag{5.9}$$

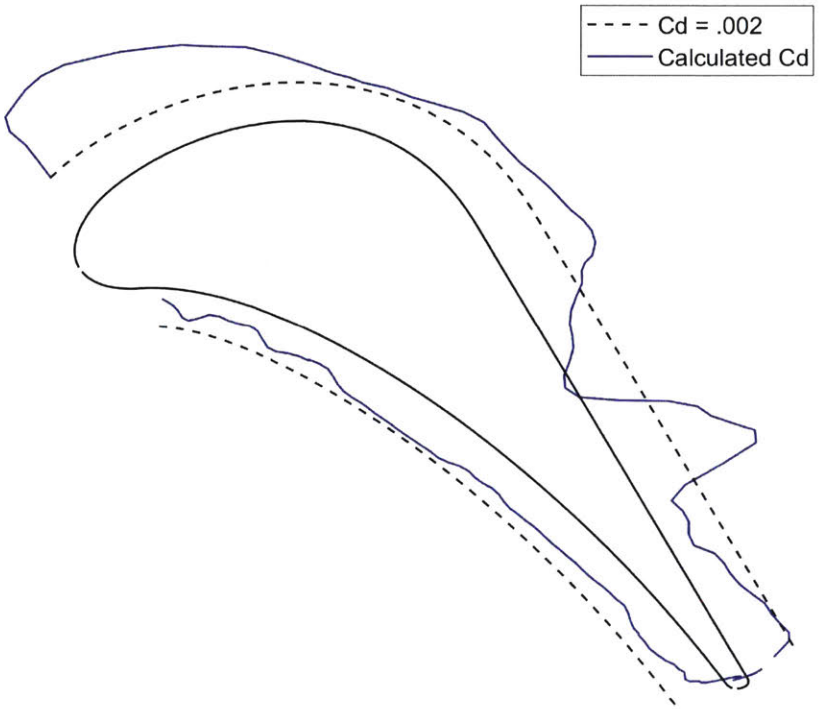

Figure 5-7: Comparison of the calculated value of Cd vs 0.002.

The surface area averaged analytical C_d for the midspan blade section is 0.002. However, the suction side average analytical C_d is greater than 0.002, and the pressure side average analytical C_d is less than 0.002. The method for calculating the profile loss from boundary layer flow attributes yields a solution closely tied to the flow physics, but the implementation is more complex. The loss accounting in Chapter 6 uses the profile loss calculated from the Reynolds number correlation for C_d, which is about equal to the result for C_d=0.002 on the entire surface.

The 2D profile loss method described in this section is applied to the 3D solution

by using the midspan results and applying them to the entire airfoil. The profile loss calculation can be improved at the expense of added complexity by assessing the loss over the entire 3D airfoil surface instead of the midspan section alone.

5.4 Trailing Edge Loss Estimation

The trailing edge loss is the loss associated with mixing out of the flow downstream of the trailing edge. The loss is a result of the sudden expansion of flow around the trailing edge, the shear layer that forms between pressure side and suction side flows, and the low base pressure at the trailing edge. Denton [1] describes a control volume method for estimating the trailing edge loss, shown in Figure 5-8.

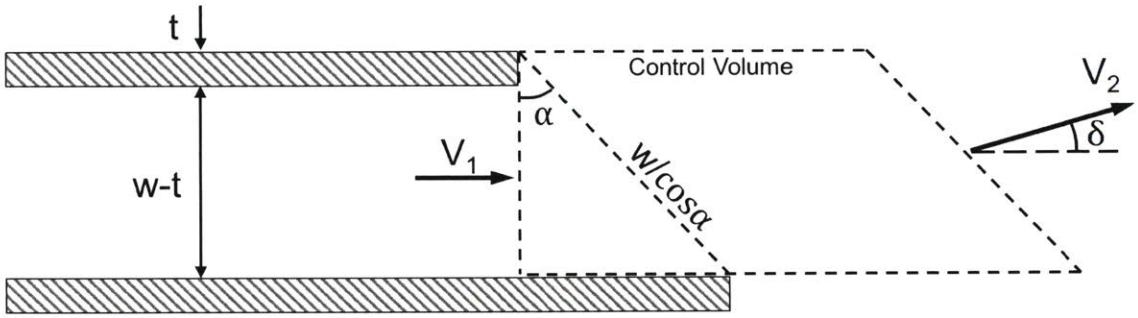

Figure 5-8: Denton's control volume for thick trailing edge loss.

Denton's control volume result is simplified to Equation 5.10.

$$\zeta = -\frac{C_{pb}t}{w} + \frac{2\theta}{w} + \left(\frac{\delta^* + t}{w}\right)^2 \tag{5.10}$$

This result assumes incompressible flow, zero flow deviation, and the suction side surface pressure is equal to the downstream pressure. The first term in Equation 5.10 is the base pressure loss, the second term represents the mixing out of the suction

and pressure side shear layers, and the third term is the sudden expansion loss from the trailing edge thickness and boundary layer blockage.

The compressible result for the trailing edge control volume is derived to assess the validity of Denton's assumptions. Figure 5-9 shows the control volume chosen for this analysis.

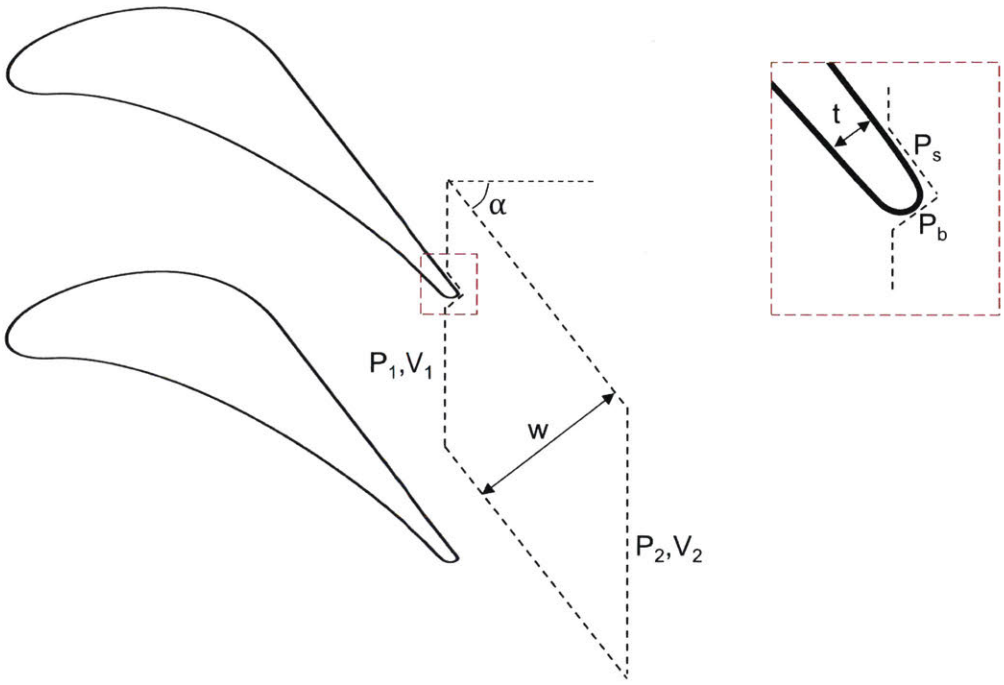

Figure 5-9: Control volume for trailing edge loss.

Since the deviation and suction side pressure are variables in this analysis, both x and y-momentum must be balanced. The suction side pressure can be calculated if the deviation is known from CFD analysis. Alternatively, an assumption can be made about the suction side surface pressure similar to Denton's approach. Equation 5.11 is the y-momentum balance for this control volume, and Equation 5.12 is the x-momentum balance which is expressed as a loss coefficient. For a 3D analysis, h is the flowpath passage height at the control volume inlet and exit.

$$(P_s - P_b)h_1 t \sin\alpha = mV_2 \sin(\alpha - \delta) - mV_1 \sin\alpha + \rho V_1^2 \theta h_1 \sin\alpha \tag{5.11}$$

$$\zeta = \frac{-C_{pb} t \cos^2\alpha}{w} \frac{\rho_1 V_1^2}{\rho_2 V_2^2} - \frac{2m\cos^2\alpha V_1}{h_1 w \rho_2 V_2^2} + \left(1 + \frac{2\theta\cos^2(\alpha-\delta)}{w}\right)\frac{\rho_1 V_1^2}{\rho_2 V_2^2} + \frac{2(h_2 - h_1)P_2}{h_1 \rho_2 V_2^2} + \frac{(P_1 - P_s)}{0.5\rho_2 V_2^2}\frac{t\sin\alpha\tan\alpha\cos\alpha}{w} - 1 \tag{5.12}$$

Equation 5.12 is dependent on the flow deviation. For a blade design with exit flow angle greater than 65 degrees, deviation is important in calculating trailing edge loss. A small deviation can have a significant change to the momentum flux through the exit boundary. The sensitivity to flow deviation is shown in Chapter 6. The importance of including the deviation in a trailing edge loss calculation is discussed. A new model is derived that does not eliminate the effect of deviation. Equation 5.13 is the resultant extended trailing edge loss model.

$$\zeta = \left[\left(\frac{2\cos(\alpha-\delta)\cos\delta}{\cos\alpha} - 1\right)\left(\frac{(w - t - \delta^*)\cos\alpha}{w\cos(\alpha-\delta)}\right)^2 - 1 + \frac{2(t + \delta^* + \theta)}{w} - \frac{C_{pb}t}{w}\right]\left[\frac{w\cos(\alpha-\delta)}{(w - t - \delta^*)\cos\alpha}\right]^2 \tag{5.13}$$

This equation appears significantly more complex than the simplified model in Equation 5.10; however, the only additional unknowns are the deviation angle and exit flow angle. The deviation angle can be determined from a computational solution or estimated from similar designs, and the exit flow angle is known from the one-dimensional turbine design. Loss accounting results are presented in Chapter 6, with results estimated from both the simplified Equation 5.10 and extended Equation 5.13 models for trailing edge loss. The trailing edge loss model with deviation is shown to represent the trailing edge loss in a highly loaded turbine more closely.

5.5 Secondary Flow Loss Estimation

The secondary flow loss is composed of three parts: endwall loss, secondary kinetic energy (SKE) loss from the passage vortex, and boundary layer loss on the airfoil suction side below the separation line [21]. The endwall loss is accounted for independently in Section 5.6 and is omitted from the definition of secondary flow loss in this section. Furthermore, it is assumed that the boundary layer loss on the airfoil suction side in the secondary flow region is the same as at the midspan section. The secondary flow loss in this thesis is only related to the loss of SKE from the mixing out of the passage vortex.

The SKE is calculated from the CFD flow field at the trailing edge. The velocity components of the flow moving perpendicular to the average exit flow angle contribute to the SKE. Equations 5.14 and 5.15 [22] relate the SKE to the velocity components. The total SKE is a mass average of the exit plane SKE. The fluid mass fraction involved in the passage vortex is equal to the ratio of displacement boundary layer thickness to span [23].

$$V_{sec} = V_z \sin\overline{\alpha} + V_u \cos\overline{\alpha} \tag{5.14}$$

$$SKE = 0.5\rho\left(V_{sec}^2 + V_r^2\right) \tag{5.15}$$

A coefficient of secondary kinetic energy (CSKE) is defined as the SKE normalized by exit dynamic pressure. The contour of CSKE in Figure 5-10 shows the location of high passage vortex loss near the suction side ID corners of the blade. The second vane CSKE contours in Figure 5-12 show high loss at both ID and OD suction side corners.

Equation 5.16 is the total entropy generation from loss of SKE, where δ^* is the endwall boundary layer displacement thickness and h is the span height.

$$\Delta s_{SKE} = \left(\frac{\delta^*}{h}\right)\frac{SKE}{0.5\rho V_{exit}^2} \tag{5.16}$$

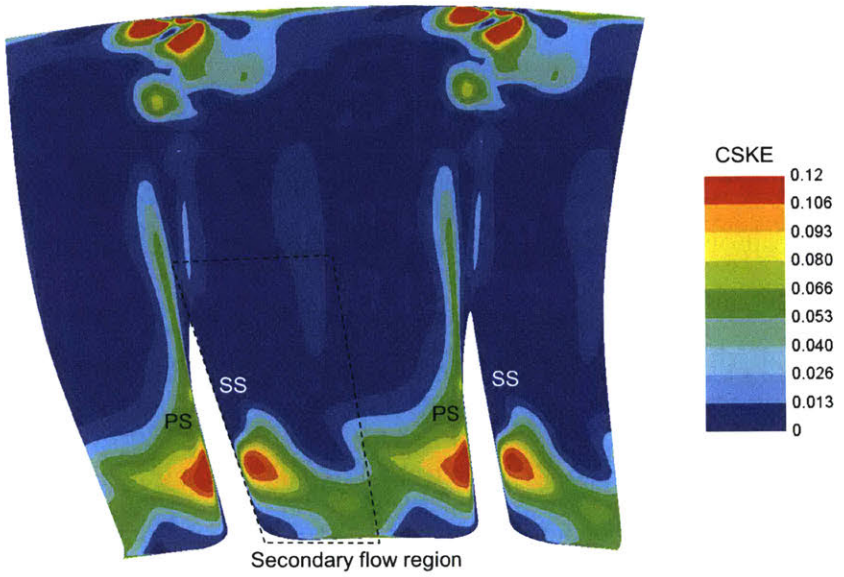

Figure 5-10: 1B trailing edge plane CSKE contour.

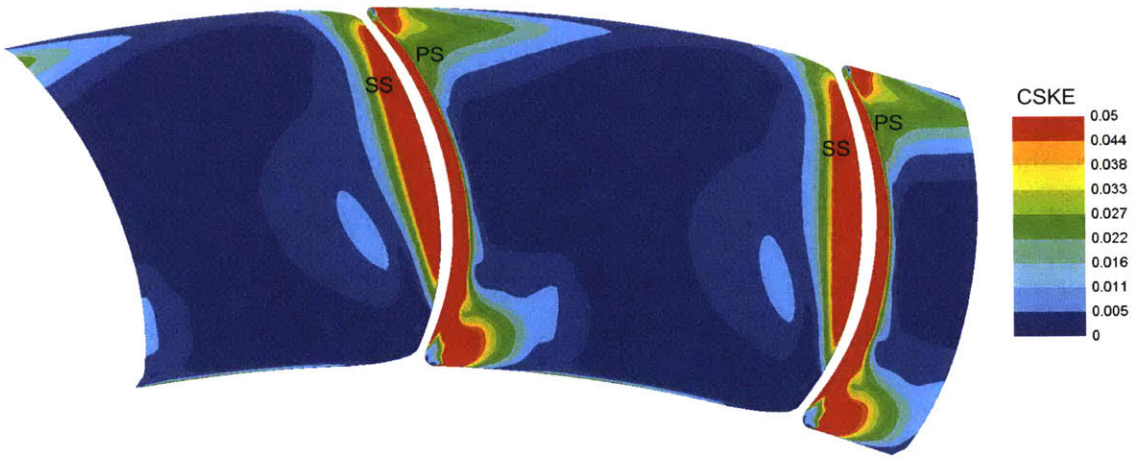

Figure 5-11: 1V trailing edge plane CSKE contour.

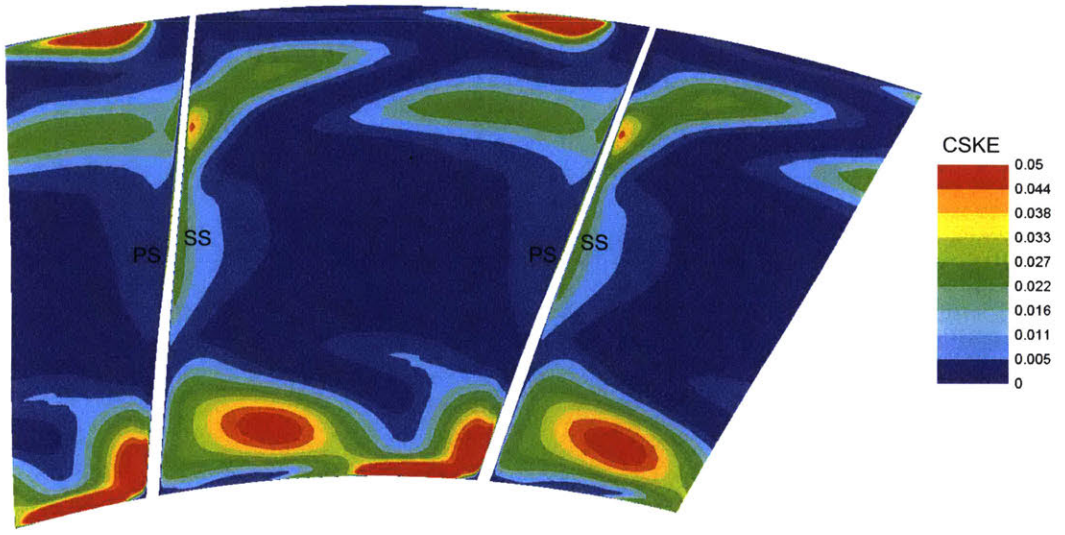

Figure 5-12: 2V trailing edge plane CSKE contour.

5.6 Endwall Loss Estimation

The endwall loss is calculated by a similar method to the profile loss; however, a uniform dissipation coefficient of 0.002 is used. This value is suggested by Denton [1] for turbulent boundary layers. The endwall free stream velocity is shown in Figure 5-13.

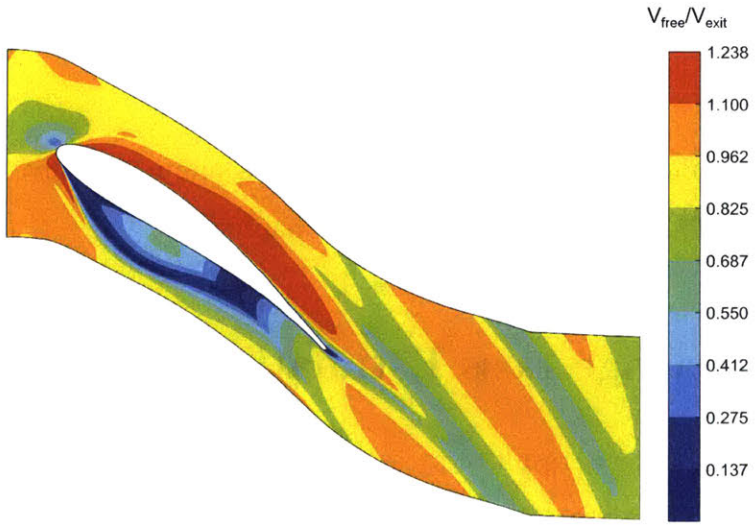

Figure 5-13: 2V inner endwall free stream velocity normalized by exit average velocity. The airfoil suction side has a high velocity.

The entropy generation is calculated by applying Equation 5.17 over the endwall area. Regions of high free stream velocity create large endwall losses.

$$S = \int_0^A \frac{\rho V_\delta^3 C_d}{T_\delta} \, dA \tag{5.17}$$

Figure 5-14 is the resulting entropy generation rate per unit area on the 2V inner endwall surface. The highest entropy generation is at the suction side where the velocity is maximum.

Figure 5-14: 2V inner endwall entropy generation per unit area. The highest entropy generation is at the airfoil suction side endwall coincident with the region of high free stream velocity.

The ID and OD endwall entropy generations are summed to give the total airfoil row endwall loss. The results are reported in Chapter 6.

5.7 Tip Leakage Loss Estimation

Blade tip clearance loss is a result of pressure driven flow between the airfoil pressure and suction sides. The leakage flow enters the gap on the pressure side and separates over the blade tip corner. For a thick trailing edge, the flow reattaches within the tip gap before discharging into the mainstream flow on the suction side [1].

The absolute velocity profile in the HIT turbine blade tip gap is shown in Figure 5-15. A separation bubble can be seen at the left side of the tip gap (pressure side entrance) on the blade surface. After the separation bubble, the flow reattaches before exiting the gap on the suction side.

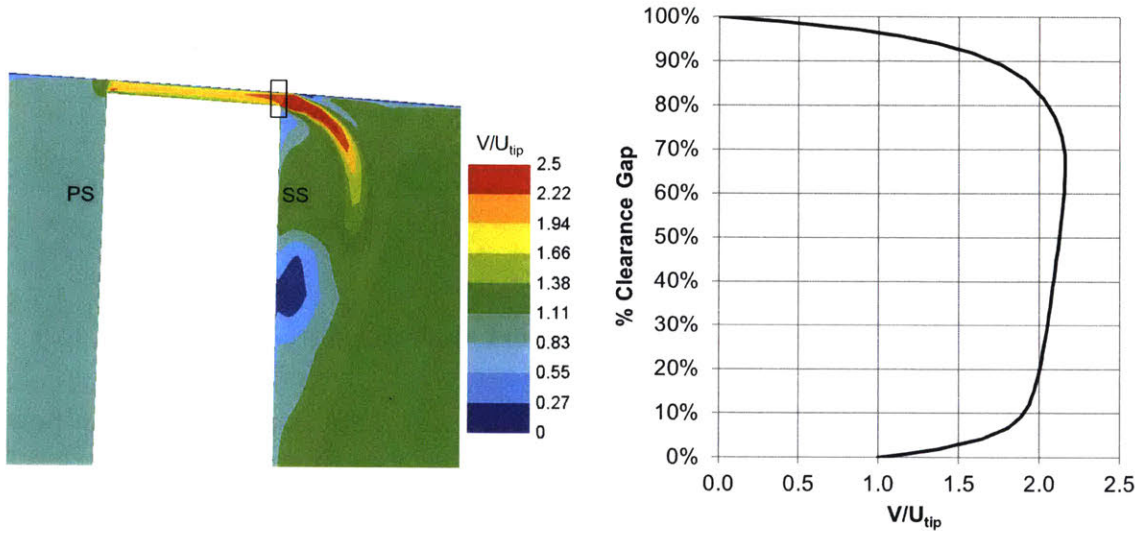

Figure 5-15: Flow is attached across the blade tip clearance gap. At the tip gap exit, the velocity distribution is used to calculate the mass flow across the tip gap at each location along the chord.

The leakage flow exits the tip gap on the airfoil suction side and tip leakage loss occurs from mixing of the leakage flow with the mainstream flow. The viscous loss from the boundary layer in the tip gap is assumed to be negligible in this analysis. Huang [6] shows that the losses within the clearance gap are small. The mixing loss model is a simple control volume for two stream mixing, applied to discrete axial locations along the suction side chord. Figure 5-16 is a diagram of the mixing loss model.

V_m is the velocity of the mainstream flow, and V_{leak} is the velocity of the tip leakage flow with an angle ϵ relative to the mainstream flow direction. The mainstream flow direction is assumed to be the angle of the suction side surface for this analysis. This control volume calculation is carried out over the length of the suction side. Figure 5-17 shows the divided blade tip section, the blue lines represent the inlet and exit

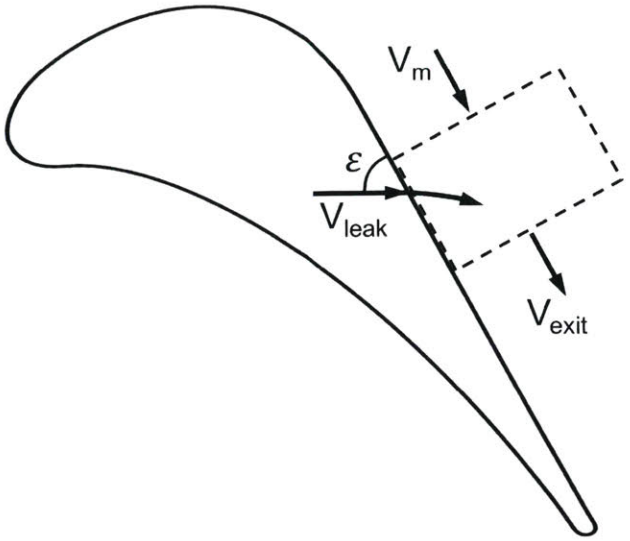

Figure 5-16: Mixing of tip leakage flow with mainstream flow.

for each individual control volume. The red arrows are the relative tip leakage flow angles and the purple arrows are the suction side angles (mainstream flow angles) for three representative locations. The arrow size represents the relative flow velocities for tip leakage and mainstream flow.

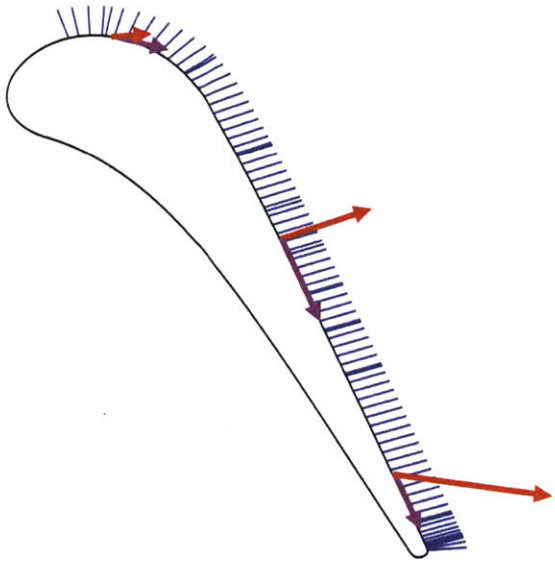

Figure 5-17: Discretization of blade tip gap with leakage flow angle.

The entropy generated by the total tip leakage loss is expressed in Equation 5.18 [24]. It is an integration across the blade surface of the control volume solution [20].

$$T\Delta s_{gen} = \int_{gap} \frac{\rho V_{leak} \sin\epsilon}{m_m} \left(\frac{1}{2}[V_{leak}^2 + V_m^2 - 2V_m V_{leak} \cos\epsilon] + c_p T \int_T^{T_{inj}} \frac{1}{T} - \frac{1}{\tau} d\tau \right) dA \tag{5.18}$$

The entropy generation from the static temperature difference is neglected in this analysis. Huang [24] estimates the right hand term of Equation 5.18 contributes less than 5% to the calculated loss since $T \approx T_{inj}$.

5.8 Oblique Shock Loss Estimation

The entropy generated from the shock system of a highly loaded turbine blade is determined by analyzing the shock as normal passage shocks. Usually the shocks are at an angle relative to the mainstream flow and are treated as oblique shocks. Normal shock relations are used to calculate the entropy generated for flow across a normal shock. The exact equation for normal shock loss is in Equation 5.19 [25]. For a weak shock, the relation can be simplified to Equation 5.20.

$$\frac{\Delta s_{gen}}{R} = \ln \left[1 + \frac{2\gamma}{\gamma+1}(M_1^2 - 1) \right]^{\frac{1}{(\gamma-1)}} \left[\frac{(\gamma+1)M_1^2}{(\gamma-1)M_1^2 + 2} \right]^{\frac{-\gamma}{(\gamma-1)}} \tag{5.19}$$

$$\frac{\Delta s_{gen}}{R} = \frac{2\gamma}{3(\gamma+1)^2}(M_1^2 - 1)^3 \tag{5.20}$$

Equation 5.20 is applied by dividing the length of a shock into several individual control volumes. This is necessary since the flow angle and velocity change across the passage, and therefore change along the shock. The shock strength is different across the passage. The shock strength is generally larger near the suction side where velocities are higher, and the majority of the shock loss occurs at this location.

The shocks in the blade passage are identified with contours of velocity divergence, relative Mach number, and static pressure. Figure 5-18 is a contour of velocity divergence at a 1B midspan section. The contours show the shock location by identifying areas of negative velocity divergence, i.e. compression.

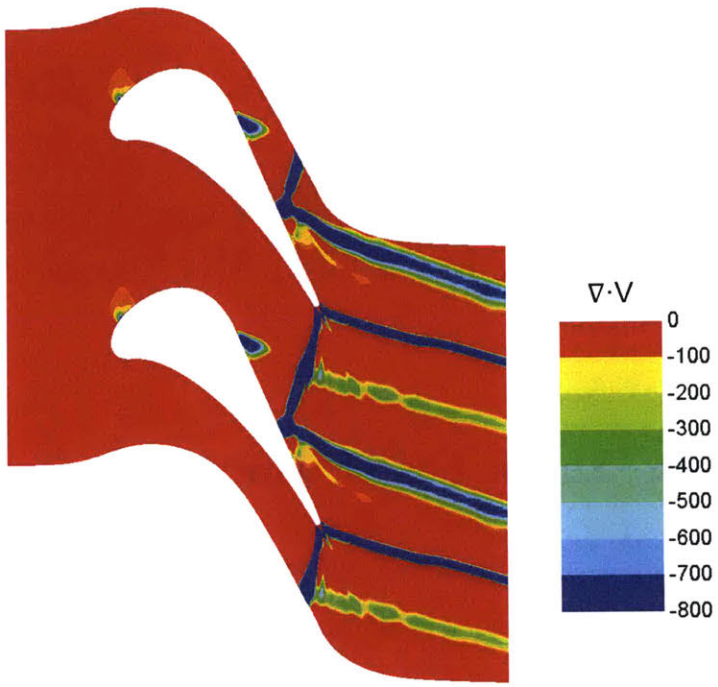

Figure 5-18: 1B midspan velocity divergence.

The two trailing edge shocks are seen clearly, along with the pressure side trailing edge shock reflection off the adjacent suction side. A fourth shock is identified originating from the suction side at about 50% chord. Data is queried from the CFD solution along the shock length for each individual shock. This data is used in equation 5.20 to calculate the shock loss from the oblique shocks. The shock angle is subject to interpretation since the shock front is not necessarily linear. The average of several measurements of shock angle is used for the calculation.

5.9 Cooling and Purge Flow Loss Estimation

The viscous and thermal mixing of purge and cooling flow with the mainstream is a source of entropy generation. This entropy generation can be estimated with a simplified control volume model of cooling flow injection into a mainstream flow, shown in Figure 5-19. This is an analogous model to the model used for the tip

leakage loss.

The control volume result for three dimensional cooling injection is described by Lim [12]. Equation 5.21 is the entropy generated by the injection of a single cooling stream into the mainstream flow. The total cooling flow loss is calculated by prescribing this relation for all the cooling sources in the turbine stage. There are 652 holes on the first vane (1V) and 425 holes on the blade (1B). This control volume result can also be applied to the purge flow entering the flowpath through inter-row gaps.

$$\Delta S_{gen} = m_c \int_{T_c}^{T_m} c_{pc}\left(\frac{1}{T} - \frac{1}{T_m}\right) dT + \frac{m_c \gamma_m R_m M_m^2}{2}\left[\left(1 - \frac{V_c}{V_m}\cos\kappa\right)^2 + \left(\frac{V_c}{V_m}\sin\kappa\right)^2\right] \tag{5.21}$$

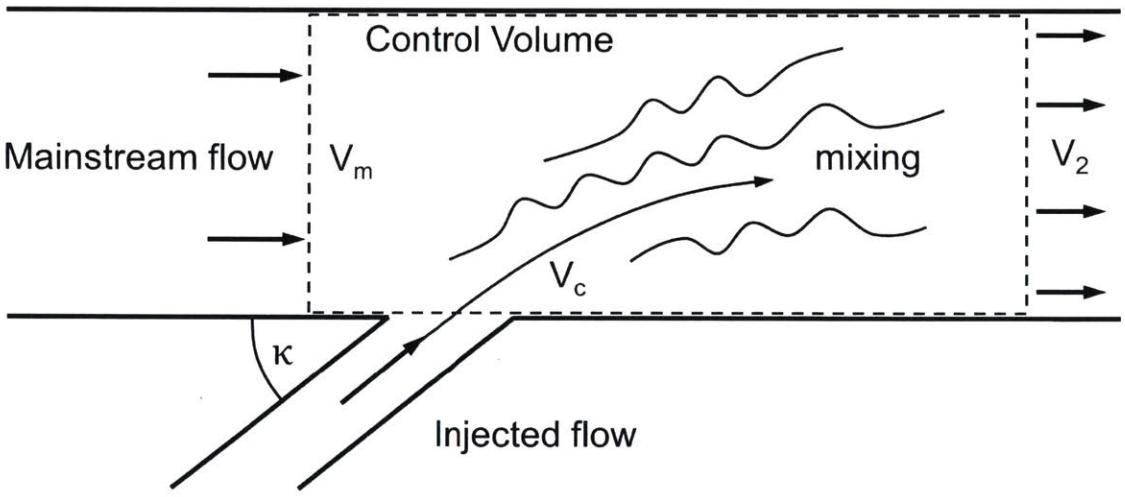

Figure 5-19: Mixing of injected cooling or purge flow with mainstream flow. The angle κ is a 3D angle between the cooling flow injection and mainstream flow.

The first term in Equation 5.21 is the entropy generation from thermal mixing of the cooling stream and mainstream temperatures. The second term is an approximation for the viscous losses of the cooling injection, assuming that all of the mainstream-flow-normal kinetic energy component of the cooling stream is lost.

5.10 Unsteady Loss Estimation

The overall unsteady loss is a time average of the unsteady multistage CFD calculation. Equation 5.2 is applied to determine the inlet-to-exit entropy generation for each airfoil row. The unsteady losses from each airfoil row are normalized to the exit rake flow condition to compare the total stage unsteady loss to the experimental loss.

The sliding mesh implemented in the unsteady analysis allows shocks from the rotor domain to travel downstream and enter the stationary vane row. These shocks travel through the vane domain with a tangential velocity equal to the rotor rotational speed. The shocks reflect off the second vane airfoil surfaces and travel back upstream toward the rotor. It is hypothesized that unsteady loss in the downstream vane is generated by this shock system. Figure 5-20 depicts the velocity divergence contour at the second vane midspan section. The negative velocity divergence indicates a shock, and one period of the shock system is identified with white dashed lines.

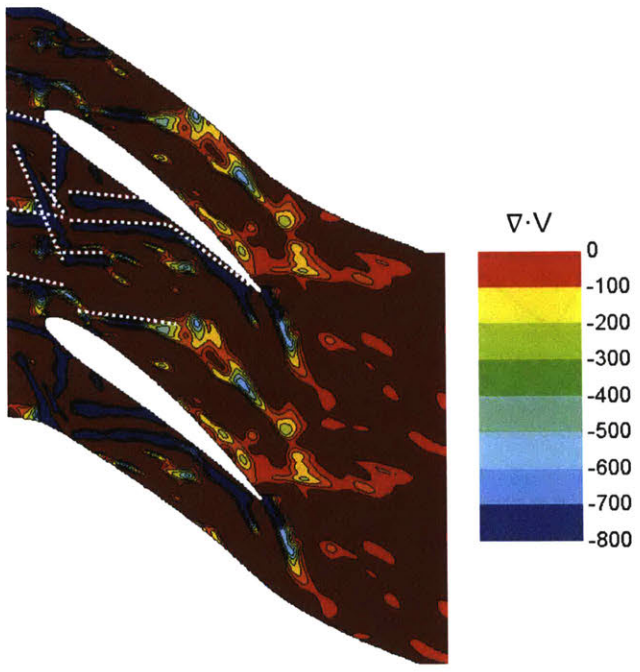

Figure 5-20: Application of the steady shock loss model to a single timepoint of the unsteady solution.

The steady shock loss calculation is used when evaluating the shock loss of the unsteady results. Single time points from the unsteady solution are analyzed individually. The procedure for determining shock loss using Equation 5.20 is applied to these individual time points, and to each shock identified in Figure 5-20.

5.11 Summary

Models for estimating various sources of loss in a 1.5 stage turbine are presented in this chapter; these models use fluid mechanics principles to determine loss from 3D complex flow using simple control volume representations. This allows a detailed inspection of the sources of loss in a turbine stage, since inefficiency can be traced back to its specific fluid mechanism. The models described in this chapter cover profile loss, trailing edge loss, shock loss, tip leakage loss, endwall loss, secondary flow vortex loss, cooling flow loss, and unsteady losses. The methodology of this thesis is to independently consider each mechanism. Using this approach, the loss accounting models can be added together and compared against the CFD solution and the experimental loss results.

Chapter 6

Results on Quantification of Loss in a Turbine Stage

The loss model calculations described in Chapter 5 are applied to all three airfoil rows. The loss models are applied to 2D and 3D representations of the rotor blade airfoil row and assessed against the CFD computational result. Additionally, the control volume loss models are applied to the first and second vane rows and compared to 3D CFD computational results.

The unsteady loss is determined from unsteady CFD simulations and assessed against the steady loss. The unsteady loss is quantified for each airfoil row. Additionally, the losses from the cooling and purge flow are presented for each airfoil row and the entire stage. These results are assessed against the HIT turbine loss estimated from measurements.

A key finding of this research is that the flow angle deviation from the trailing edge metal angle has a significant effect on the trailing edge loss calculation. This effect is important for a highly loaded transonic airfoil with a large exit angle. Since this effect is mentioned throughout this chapter, the first section discusses the trailing edge loss calculation sensitivity in detail.

6.1 Trailing Edge Loss Sensitivity

The trailing edge loss calculation methods described in Section 5.4 are sensitive to the boundary condition inputs. Equation 5.10 is quantitatively inaccurate for flow situations involving transonic-supersonic turbine blade design with high flow deflection greater than 65 degrees, but the key physics are preserved which capture the effects of trailing edge thickness, base pressure, and boundary layer thickness. The full control volume calculation, Equation 5.12, conserves mass and momentum and therefore is quantitatively accurate for capturing the fully mixed out trailing edge loss. This full control volume approach, however, is still sensitive to each term in the equation, and the implementation of this full control volume approach requires numerous flow quantities from a CFD computation. The extended trailing edge model is proposed, Equation 5.13, which adds the deviation and exit flow angle effect to Denton's simplified compressible model.

Deviation is the incremental flow angle change after the flow has moved past the physical trailing edge of the airfoil. A positive deviation occurs when the flow moves toward the suction side, and a negative deviation when the flow moves toward the pressure side. For a subsonic airfoil, the deviation is likely positive as streamlines curve from pressure side to suction side at the trailing edge while satisfying the Kutta condition. A negative deviation can occur for a transonic airfoil when the trailing edge suction side shock is stronger than the trailing edge pressure side shock. This results in a higher static pressure aft of the trailing edge on the suction side, and the flow turns toward the pressure side.

Figure 6-1 is the mass averaged passage flow angle of the HIT turbine blade row. After the trailing edge, which is at the location $x/C_x = 1$, there is significant turning of the flow in excess of the blade metal angle. This negative deviation is about 3.3 degrees.

It is noted by Denton [2] that a negative deviation acts to reduce the calculated trailing edge loss, but the magnitude of this reduction is not quantified. It is found in this thesis that for a blade exit metal angle of >65 degrees, a deviation of -2 degrees

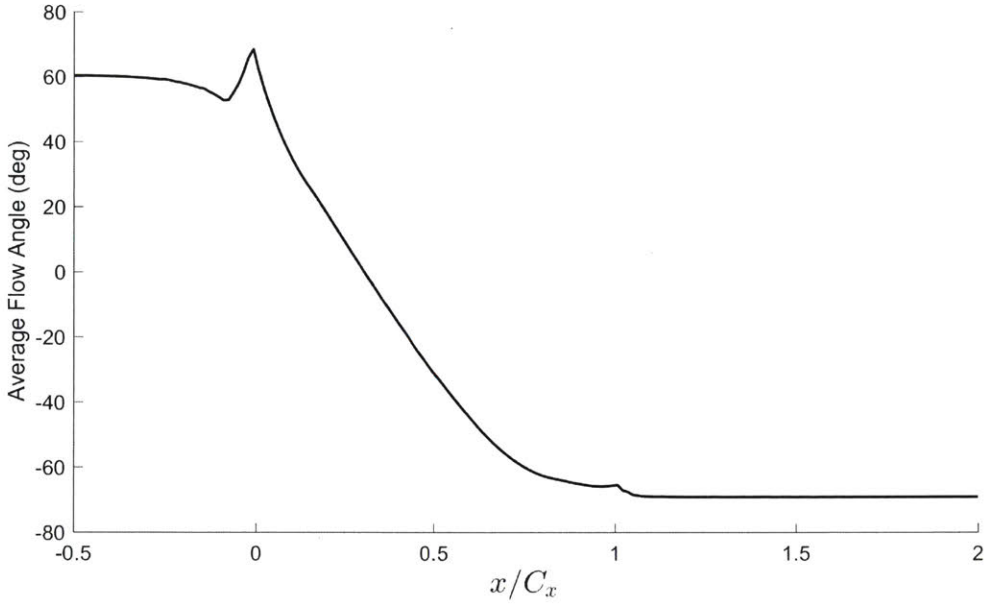

Figure 6-1: Trailing edge negative flow deviation for the blade airfoil caused by trailing edge shock turning. The flow turns an additional 3.3 degrees after the trailing edge ($x/C_x = 1$).

is capable of reducing the calculated trailing edge loss by 30%. Figure 6-2 shows the variation in calculated trailing edge loss for the HIT turbine blade with Denton's simplified model and the extended model from Section 5.4 at the nominal pressure ratio and incidence angle.

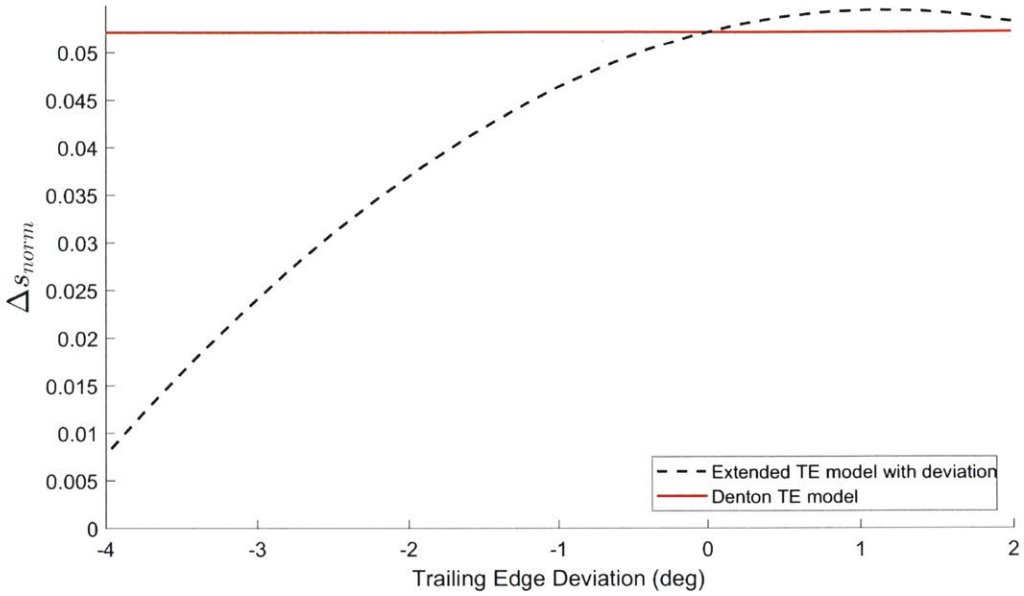

Figure 6-2: The calculated trailing edge loss from Denton's simplified model and the extended trailing edge loss model. Calculated trailing edge loss is reduced significantly for negative deviation.

In Figure 6-2, all model variables are fixed, and the deviation is varied. The calculated trailing edge loss is sensitive to deviation when the extended model is applied, which is derived from the full control volume result. The larger the exit angle of the flow, the larger the sensitivity to deviation. For large airfoil turning, a small change in flow angle equates to a large change in momentum flux through the domain exit. Therefore, trailing edge loss calculation for highly loaded airfoils with large turning is particularly sensitive to flow deviation. This is especially the case for transonic highly loaded airfoils with negative deviation from trailing edge shocks.

The extended trailing edge loss model preserves the original sensitivity to boundary layer thickness, trailing edge thickness, and base pressure from Denton's model. Figure 6-3 shows the change in trailing edge loss calculation with variation in trailing edge thickness, and it is the same for both models.

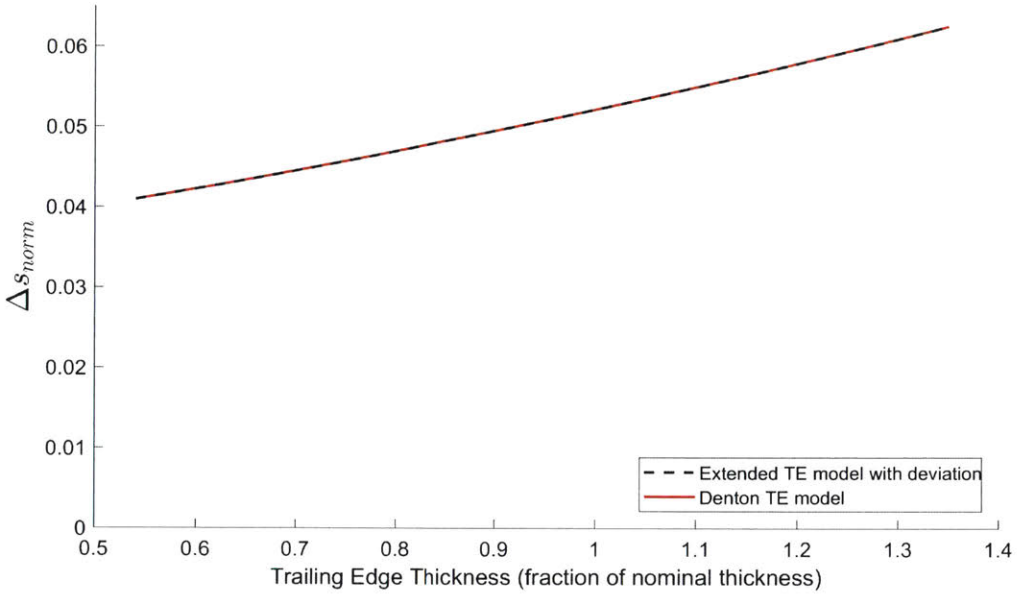

Figure 6-3: Trailing edge loss calculation dependence on trailing edge thickness for two loss models. The extended trailing edge model preserves the trailing edge thickness sensitivity of Denton's simplified model.

The assumption of zero deviation in the simplified incompressible approach is not appropriate for high turning transonic airfoils since it overestimates the trailing edge loss. In place of Denton's model, the extended model is implemented that accounts for flow deviation. In the following sections, the loss accounting results are shown with both Denton's trailing edge model and the extended trailing edge model for comparison.

6.2 Steady Uncooled Loss Results

6.2.1 Blade Row Results

The creation of entropy through an airfoil row is calculated from the CFD solution by dividing the domain into axial planes and calculating the mass averaged entropy for each plane (with the domain inlet as the reference). The axial progression of entropy generation through the blade row is shown in Figure 6-4. The 2D cascade,

3D midspan, and 3D full domain are shown. The 3D domain result shows the highest entropy creation since additional losses from endwall loss, secondary flow vortex loss, and tip leakage loss are present. It is notable that a large portion of the loss in an airfoil row occurs downstream of the trailing edge, denoted by x/C_x=1. This downstream loss is attributed to the trailing edge mixing loss, the tip leakage flow that mixes out past the trailing edge, the secondary flow vortex mixing, and endwall loss downstream of the trailing edge. There may also be oblique shock loss downstream of the trailing edge depending on the configuration and strength of the trailing edge shocks.

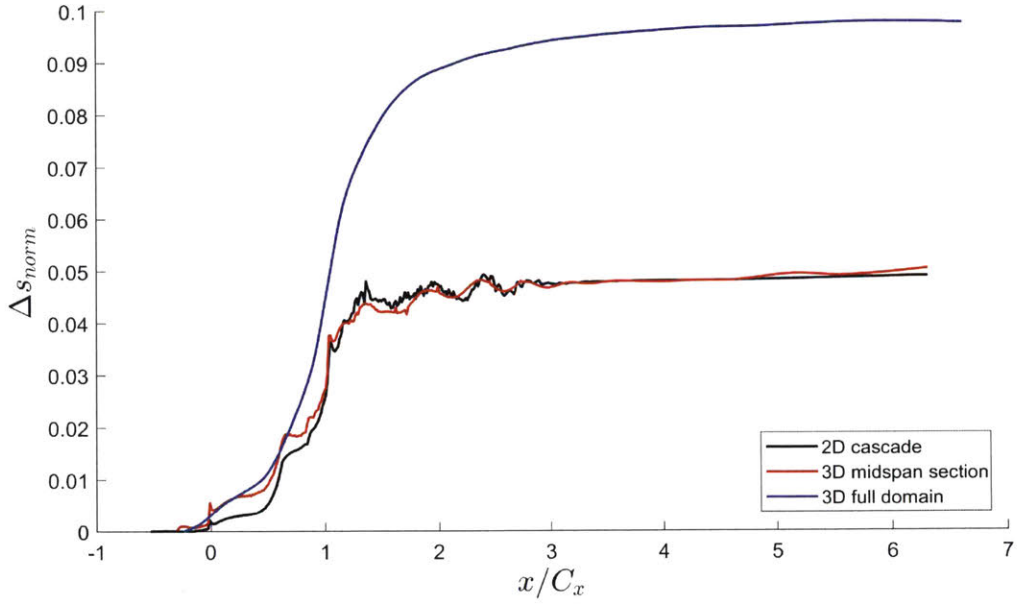

Figure 6-4: Entropy generation of the blade row for a domain with extended exit. The 2D cascade result and the 3D midspan section results are similar. The 3D full domain result shows the additional loss from 3D effects.

Figure 6-5 is a comparison between the 3D short multistage domain result and the 3D extended domain result. A significant portion of the overall entropy is generated downstream of the multistage domain exit. This mixing loss occurs in the downstream second vane airfoil row for the multistage analysis. The 3D short domain and 3D extended domain results have negligible difference up until the end of the short domain.

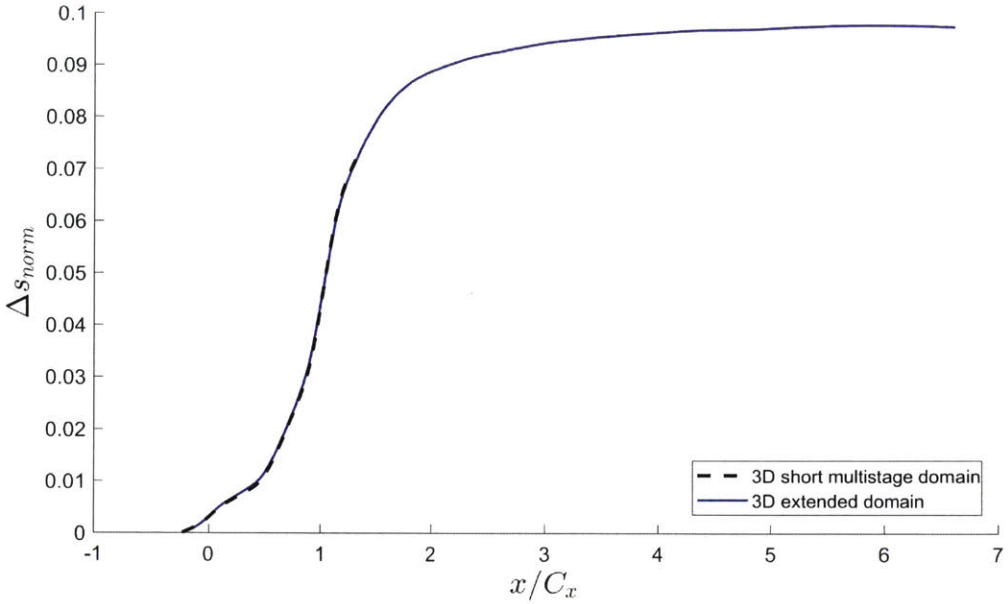

Figure 6-5: Entropy generation of the blade row for a domain with extended exit compared to the axially shorter multistage domain. The entropy generation is similar up until the multistage domain exit. The mixing loss downstream of the short blade domain is realized in the downstream 2V domain.

The loss accounting models are initially assessed for the blade midspan section via 2D analysis. In the 2D analysis, the only loss generating mechanisms are trailing edge loss, profile loss, and oblique shock loss. Downstream mixing loss is subtracted since the flow is not fully mixed out at an axial location consistent with the rake location in the cascade test. The downstream mixing component is determined from a CFD solution where the TE wake is mixed out at constant area and with a slip wall boundary condition. Alternatively, the fully mixed out loss could be calculated by the iterative procedure described by Prasad [19]. In Figure 6-6, the simplified incompressible TE loss calculation, Equation 5.10, is applied with the assumption that deviation is negligible. With this trailing edge loss model, the sum of the loss models is 78% over that determined from the CFD computation. Denton's trailing edge loss model neglects the impact of deviation, and yields a significantly higher level of trailing edge loss. The use of this assumption for highly loaded, high turning airfoils likely overestimates the loss significantly.

In Figure 6-7, the trailing edge loss is recalculated with the extended simplified

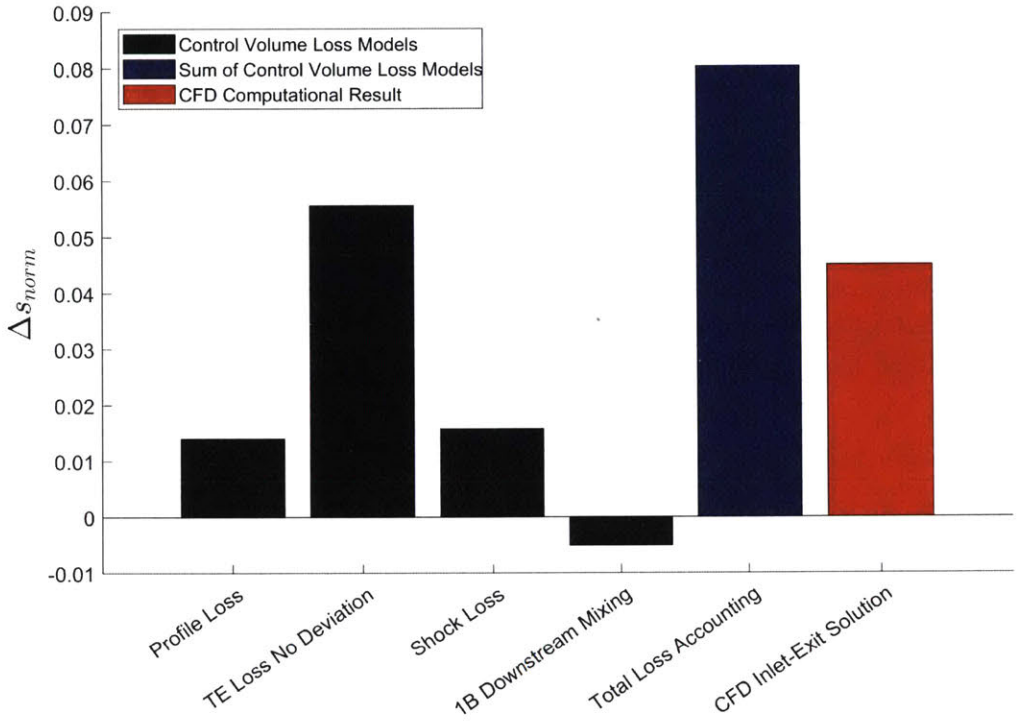

Figure 6-6: 1B control volume loss accounting for 2D cascade analysis with $\delta = 0$ assumption. The trailing edge loss is dominant, and the sum of the control volume results exceeds the computational result.

incompressible approach, Equation 5.13. The trailing edge loss is now a similar magnitude to the profile and oblique shock loss, and the sum of the control volume models is within 6% of the entropy generation estimated from CFD computed flow.

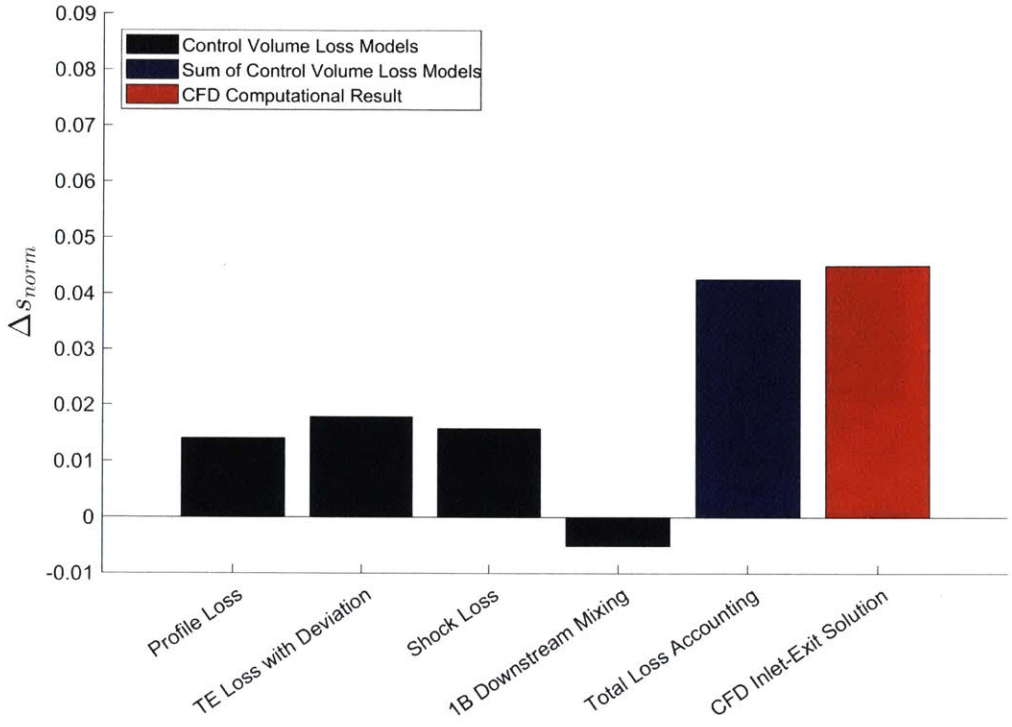

Figure 6-7: 1B control volume loss accounting for 2D cascade analysis with $\delta \neq 0$. The trailing edge loss is the largest loss component, and the sum of the control volume results is comparable to the computational result.

The results for the trailing edge calculation including the deviation angle is quantitatively closer to the CFD result. For both approaches, the trailing edge loss is the largest loss mechanism.

Mee [3] analyzed and tested a turbine cascade at a range of Mach numbers from 0.6 to 1.2. Extrapolating this result to the HIT turbine design point of Mach 1.3, it can be compared to the HIT turbine 2D results. The turbine design in Mee's experiment has a t/w=6.3%, the same value as the HIT turbine design. For both assessments, the trailing edge mixing loss is dominant, providing support for the observation of large trailing edge losses for transonic turbine blades. Figure 6-8 shows the relationship between Mee's loss estimate and the HIT results in Figure 6-7 as a percentage of total

entropy generation.

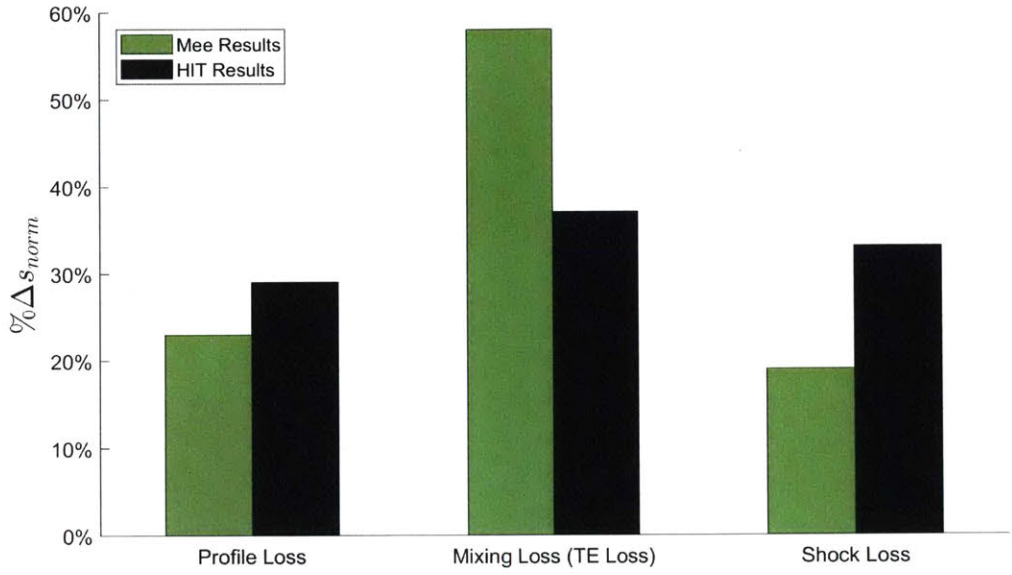

Figure 6-8: Mee's loss accounting for a high Mach number cascade compared to HIT cascade result. The trailing edge loss is highest for both analyses.

Mee's mixing loss result is calculated with traverse total pressure measurements at the trailing edge compared to the exit total pressure [3]. Consequently, some of the downstream shock loss may be attributed to the downstream mixing loss. If this factor were to be resolved, Mee's result may be more in-line with the HIT cascade control volume loss accounting result (i.e. higher shock loss and lower trailing edge mixing loss).

After the 2D analysis is complete, the loss accounting models are applied to the 3D geometry and flow. A 3D airfoil row has several loss generating mechanisms that are not present in the 2D flow field. Tip leakage loss, endwall loss, secondary flow vortex loss, and multistage mixing loss must be considered. Figure 6-9 presents the 3D blade row loss accounting with the simplified (Equation 5.10) trailing edge loss model. The trailing edge loss is dominant, and the total loss accounting overestimates the CFD result.

The results are re-calculated with the extended trailing edge loss model and shown in Figure 6-10. Consistent with the 2D result, the calculated trailing edge loss is

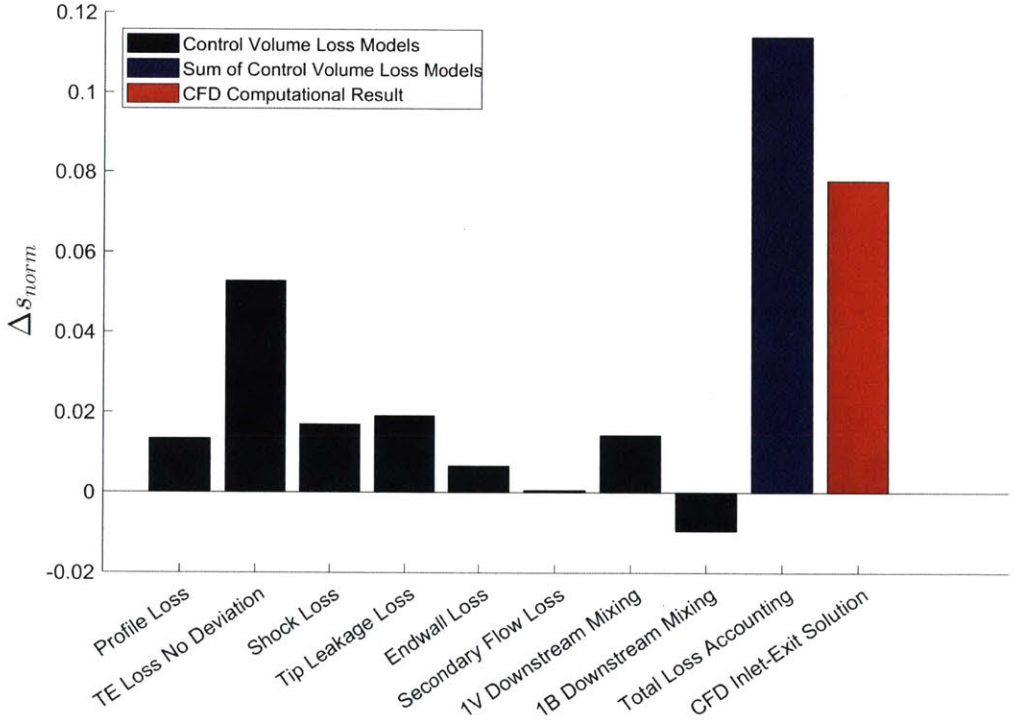

Figure 6-9: 1B control volume loss accounting for 3D multistage analysis with $\delta = 0$ assumption. The trailing edge loss is dominant, and the sum of the control volume results exceeds the computational result.

greatly reduced. The trailing edge loss is now the second largest loss mechanism, behind the tip leakage loss. The tip leakage loss, trailing edge loss, and oblique shock loss are each about one quarter of the blade loss. The profile loss is still significant, but lower than the three previously listed. The secondary flow and endwall losses are the smallest loss contributions. Compared to profile loss, the small endwall loss is reasonable since there is little endwall area on the high aspect ratio blade with small axial gaps between airfoil rows.

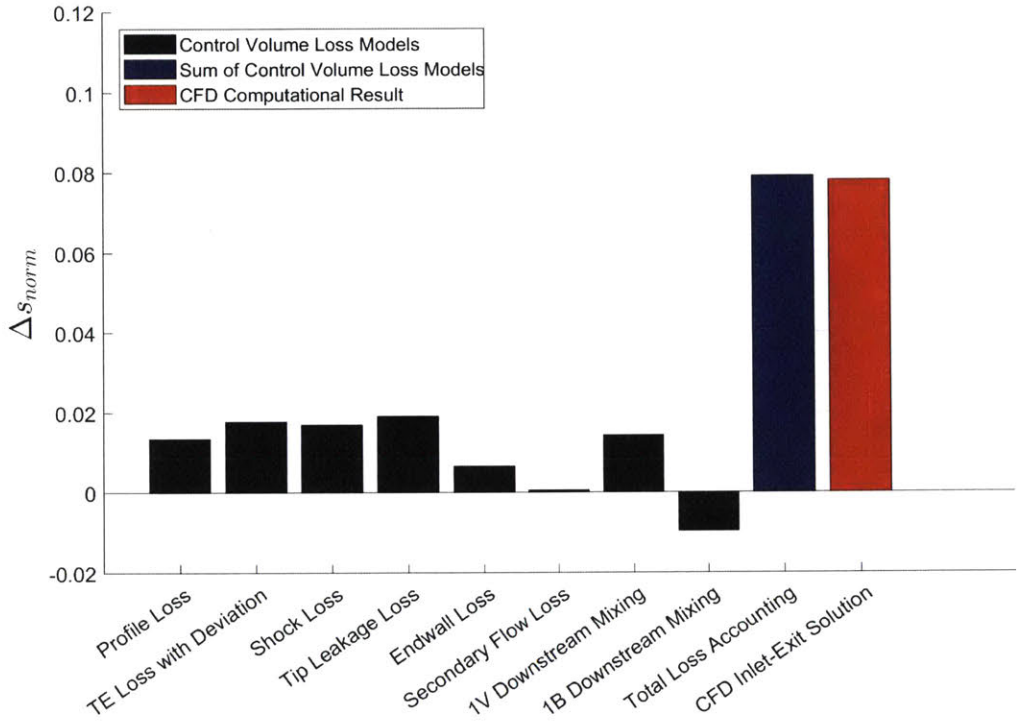

Figure 6-10: 1B control volume loss accounting for 3D multistage analysis with $\delta \neq 0$. The trailing edge loss and tip leakage loss are the largest loss components, and the sum of the control volume results is comparable to the computational result.

The result in Figure 6-10 denoted by "CFD Inlet-Exit Solution" is determined from the multistage blade row CFD solution that uses as the inlet condition the flow at the mixing plane downstream of 1V; likewise it uses an outflow condition the flow at the mixing plane upstream of 2V. Therefore, the CFD simulation does not have uniform inlet and exit boundary conditions (pressure, temperature, and velocity profiles) and there is a loss associated with mixing out the flow non-uniformities. The

mixing out of the blade inlet (1V exit) is added to the blade row loss accounting, and the mixing out of the blade row exit (2V inlet) is subtracted. After these adjustments, the sum of the 3D blade control volume models is within 2% of the CFD inlet-to-exit solution.

The tip leakage loss is the largest loss component in the blade row. Tip clearance gap is an important design parameter and effects the performance of the turbine. To assess the impact of varying tip clearance on blade row loss, CFD simulations are implemented with varying levels of tip clearance. Figure 6-11 shows the loss trend with tip clearance gap.

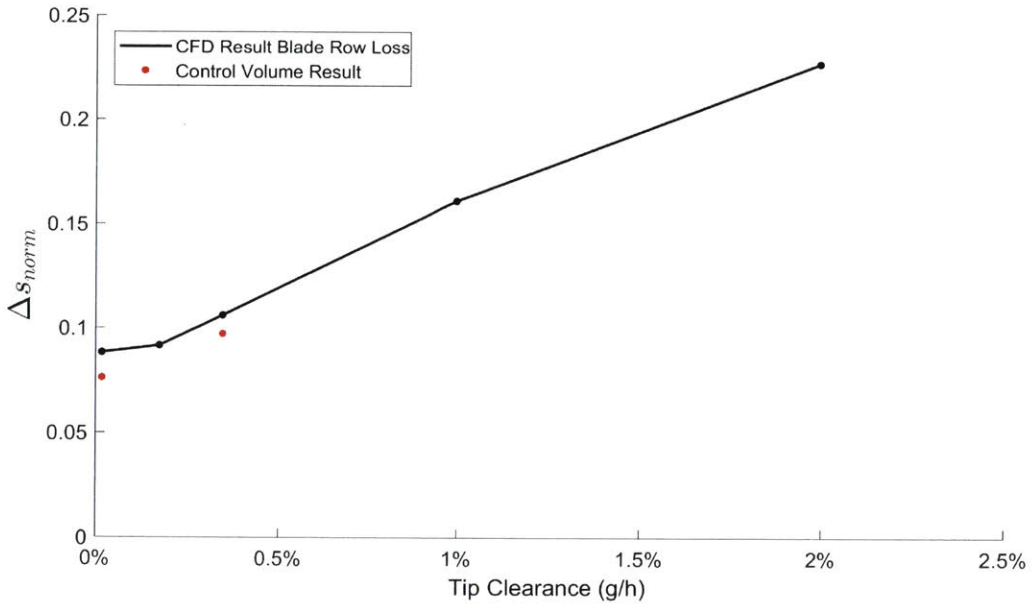

Figure 6-11: Overall loss from a CFD solution of an extended blade row 3D domain with varying tip clearance from 0.02% to 2% of span. The CFD computed loss difference between nominal and vanishingly small clearance is comparable to the tip leakage loss difference calculated using the control volume model.

The variation in CFD computed blade row loss with tip clearance is comparable to the difference calculated using the control volume model for tip clearance loss.

Several assumptions explain differences between the control volume loss accounting and the CFD computed loss for the airfoil row. The profile loss, shock loss, and trailing edge loss calculation results are determined from the midspan section of the 3D blade. Each of these loss components may be different at other span locations.

The viscous loss of the tip leakage flow through the tip gap and the thermal component of tip leakage mixing are both neglected; both could add additional calculated loss. Also, the full mixing out of the airfoil downstream flow is considered. In the actual flow, the full mixed out loss may not be realized. Furthermore, several of the loss accounting control volume models make simplifying assumptions (e.g. incompressible flow, uniform mainstream flow, linear shock fronts, etc).

6.2.2 First Vane Row Results

The entropy generation in the first vane row is calculated for axial cut planes through the domain. Figure 6-12 is the entropy generation of the first vane row for the 3D multistage short domain and the 3D extended domain.

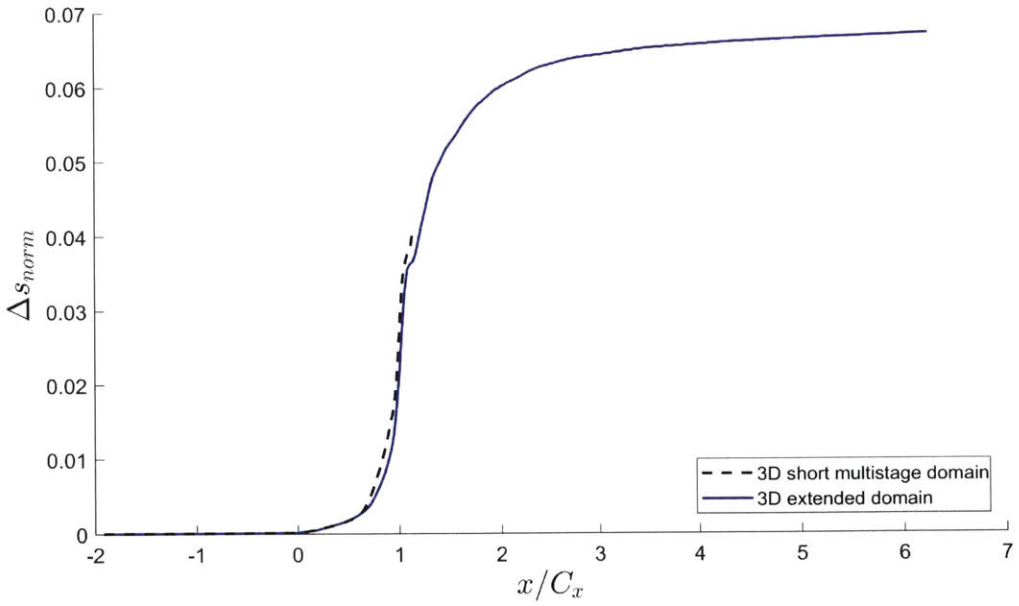

Figure 6-12: Entropy generation of the first vane row (1V) for a domain with extended exit compared to the axially shorter multistage domain. The entropy generation is similar up until the multistage domain exit. The mixing loss downstream of the multistage domain is realized in the downstream 1B domain.

Figure 6-13 compares the loss accounting models to the steady CFD computed loss for the first vane row. In this result, the trailing edge loss is the largest calculated loss component. The high trailing edge loss is likely the reason the sum of the loss

models is above the loss level calculated from the CFD result.

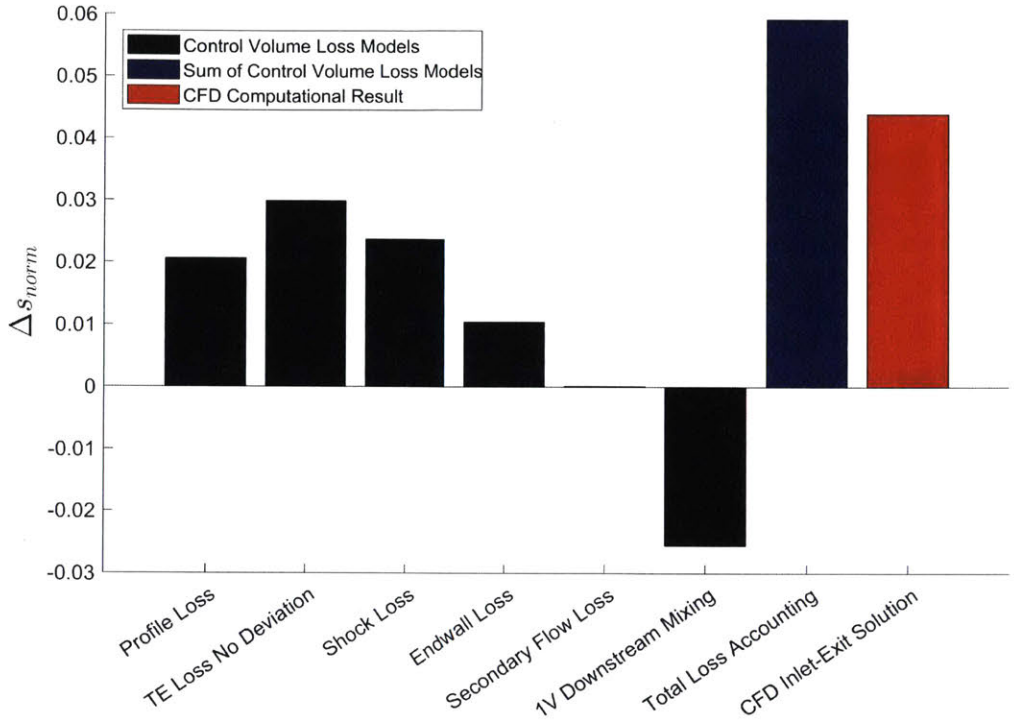

Figure 6-13: 1V control volume loss accounting for 3D multistage analysis with $\delta = 0$ assumption. The trailing edge loss is dominant, and the sum of the control volume results exceeds the computational result.

The 1V airfoil has an exit relative Mach number above Mach 1 and turning of 80 degrees. This high turning angle makes the trailing edge result sensitive to deviation. In the CFD solution, a small negative deviation is observed as a result of a shock near the trailing edge on the suction side. When the negative deviation is accounted for using the Equation 5.13 model, the sum of the control volume models is within 10% of the CFD inlet-to-exit solution. This result is shown in Figure 6-14.

The trailing edge loss is now the third largest loss component, behind the profile loss and shock loss. The secondary flow vortices are small for the 1V and the secondary flow loss is small. The endwall loss is more significant for the 1V than for the blade row since the endwall area is larger. The downstream mixing loss that occurs past the exit mixing plane location is significant, shown in Figure 6-12, and is subtracted from the 1V loss accounting result.

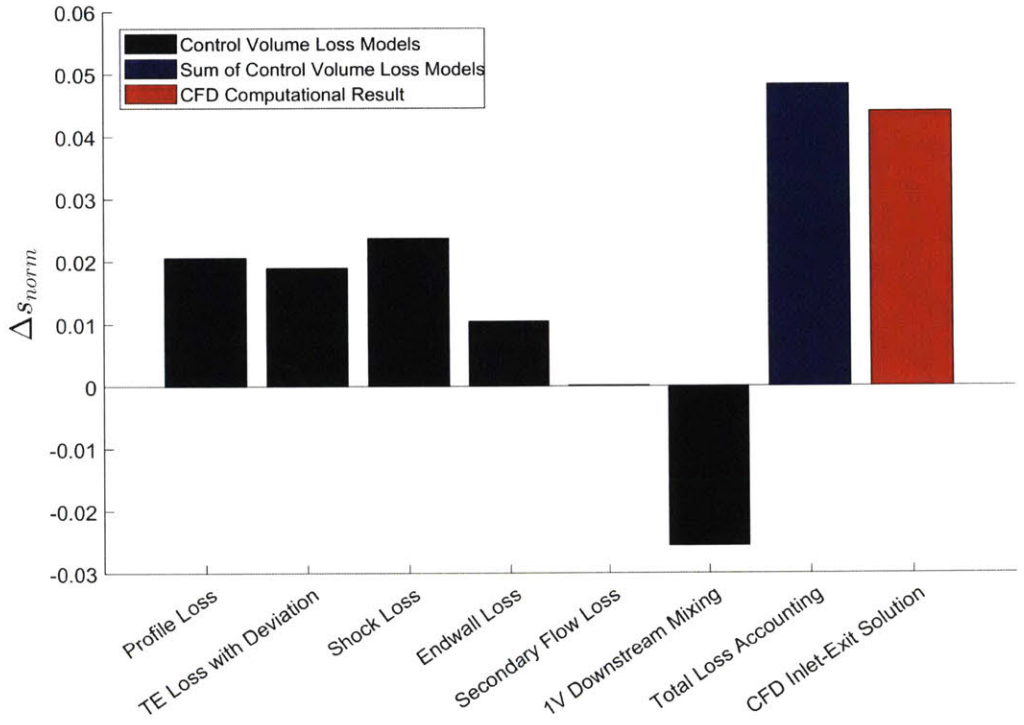

Figure 6-14: 1V control volume loss accounting for 3D multistage analysis with $\delta \neq 0$. The shock loss is the largest loss component, and the sum of the control volume results is comparable to the computational result.

6.2.3 Second Vane Row Results

The entropy generation in the second vane row is calculated for axial cut planes through the domain. Figure 6-15 is the entropy generation of the second vane row for the 3D multistage short domain and the 3D extended domain. The short domain only extends to the axial location of the blowdown rig exit rake.

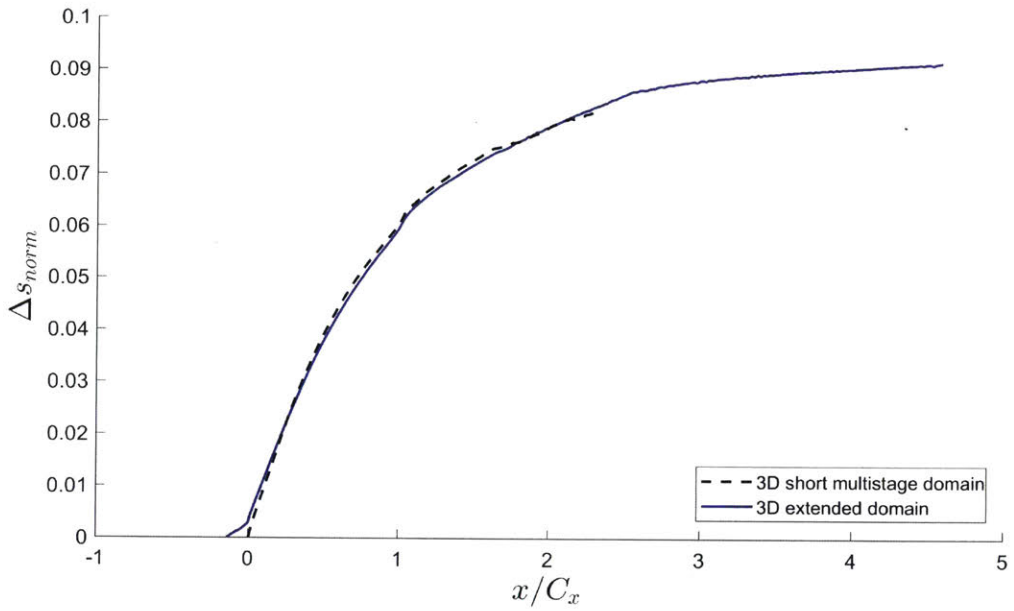

Figure 6-15: Entropy generation of the second vane row (2V) for a domain with extended exit compared to the axially shorter domain which ends at the downstream rake location. The entropy generation result is similar up until the exit rake. The mixing loss downstream of the exit rake is accounted for in the 2V loss accounting.

The loss components for the second vane row (2V) are computed. Figure 6-16 compares the loss accounting models to the steady CFD computational result. This result is with Denton's simplified trailing edge model. The sum of the control volume models is within 6% of the CFD inlet-to-exit solution.

The 2V trailing edge losses are re-calculated with the extended trailing edge model. Figure 6-17 summarizes the result.

Since the 2V exit flow angle is less than 55 degrees and the deviation is small, there is little difference between the two trailing edge models. With the extended trailing edge loss model, the loss accounting is within 2% of the CFD computed result.

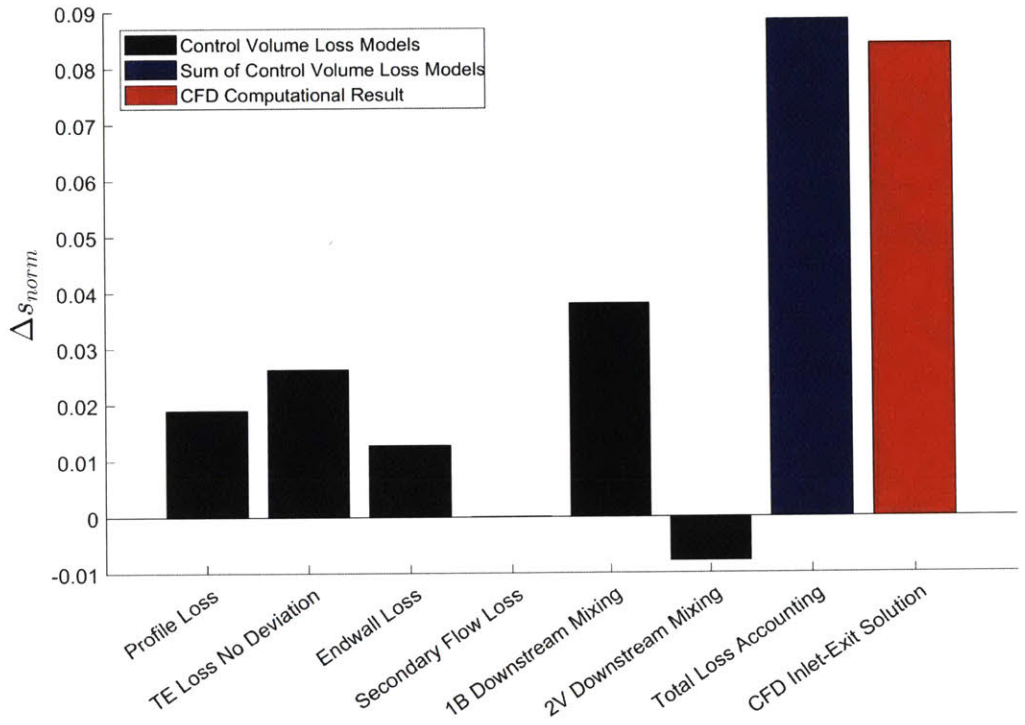

Figure 6-16: 2V control volume loss accounting for 3D multistage analysis with $\delta = 0$ assumption. The trailing edge loss and 1B downstream mixing loss is dominant, and the sum of the control volume results slightly exceeds the computational result.

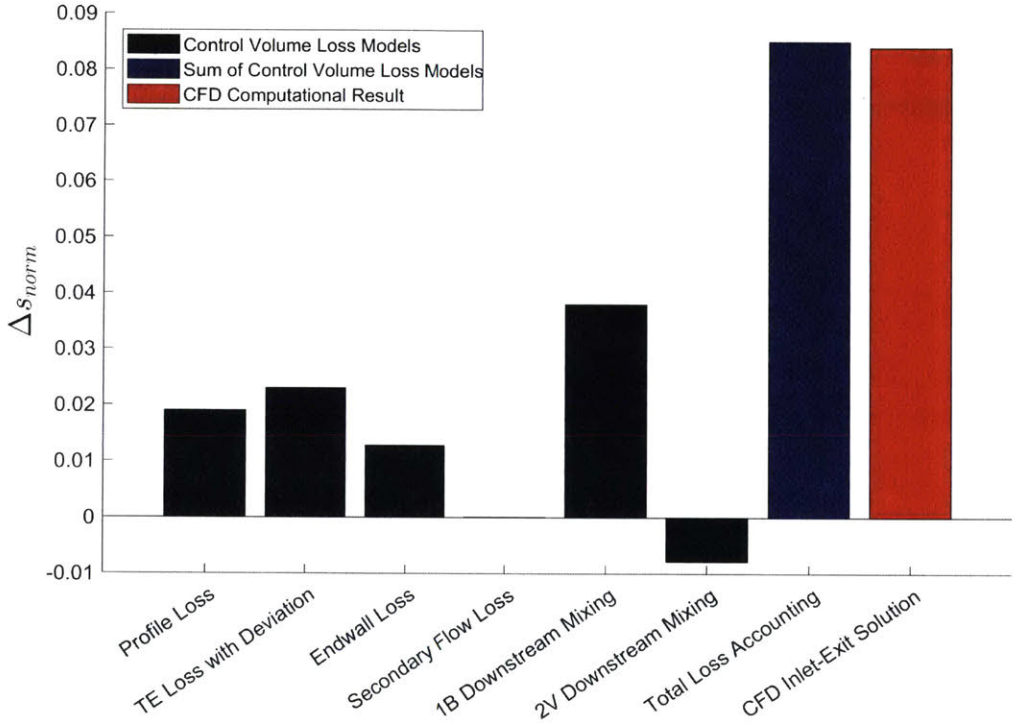

Figure 6-17: 2V control volume loss accounting for 3D multistage analysis with $\delta \neq 0$. The trailing edge loss and 1B downstream mixing loss is dominant, and the sum of the control volume results is comparable to the computational result.

6.2.4 Steady Loss Accounting Summary

In general, the trailing edge loss is a significant loss component for all airfoil rows. Oblique shock losses contribute to the loss of a transonic stage; these shock losses would not be present if the blade design remained in the subsonic flow regime. Figure 6-18 compares the control volume loss accounting result with the computational result for all three airfoil rows and the full 1.5 stage turbine.

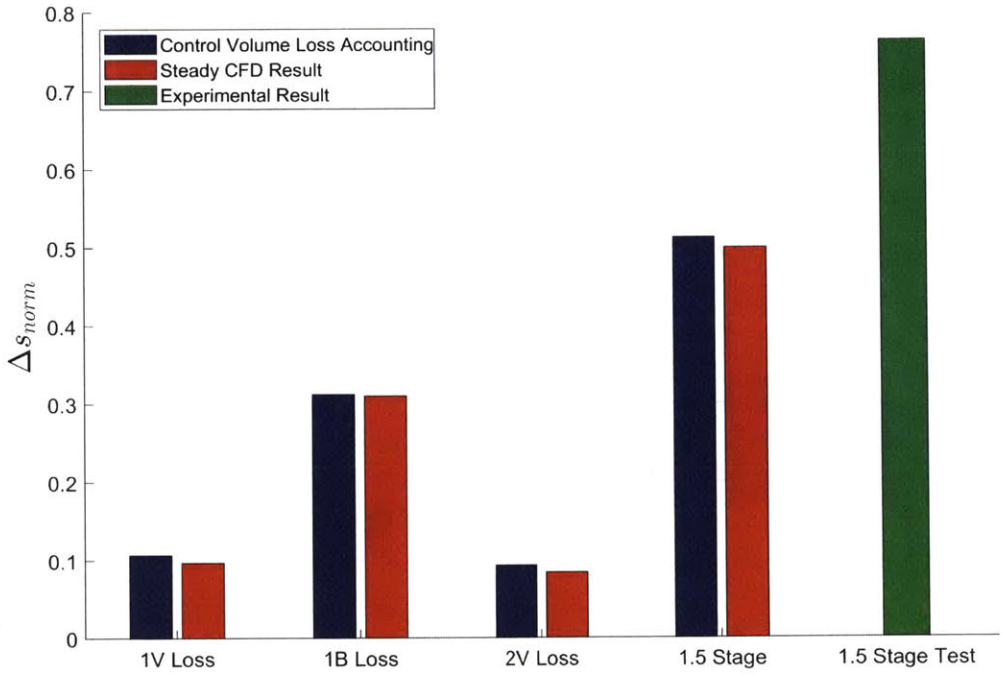

Figure 6-18: The control volume loss accounting model results for each airfoil row and the entire stage are quantitatively comparable to the 3D multistage CFD inlet-exit results.

The 3D 1.5 stage control volume loss accounting is within 5% of the computational result. The time averaged experimental result from the HIT turbine blowdown rig is also shown. The loss accounting and CFD results are for steady, uncooled models, therefore, unsteady and cooling flow effects are needed to fully explain the blowdown test data. The losses from unsteady flow, airfoil cooling, and purge flow are described in Sections 6.3 and 6.4 below.

6.3 Unsteady Loss Results

Upon completing the formulation and development of loss models to account for the steady analysis results, the unsteady CFD computation is post-processed to determine the unsteady loss. The unsteady analysis allows the first vane wakes to travel into the blade row domain, and for the blade trailing edge wakes and shocks to propagate into the downstream 2V airfoil row. Figure 6-19 shows the contour of the divergence of velocity from the steady and unsteady solution of the downstream vane; the unsteady flow at a particular instant shows the presence of shock systems in the 2V passage. These shocks move through the second vane domain with a tangential velocity equal to the rotor speed.

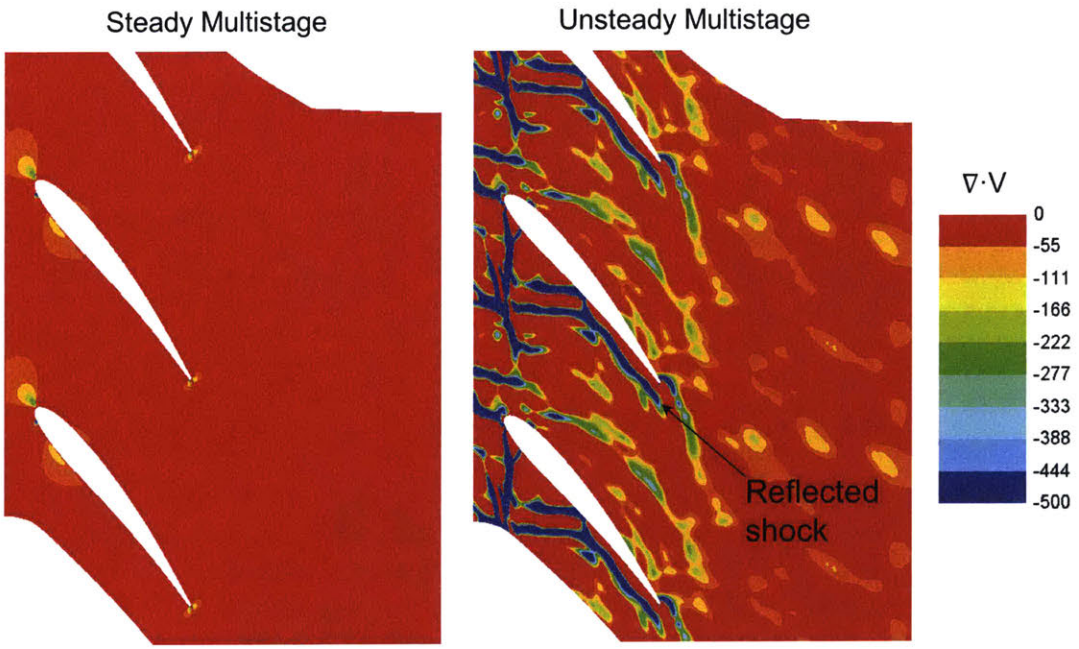

Figure 6-19: Velocity divergence in a steady analysis compared to an unsteady analysis. The negative velocity divergence shows the location of shocks that have traveled into the 2V domain from the 1B trailing edge. Reflected shocks travel upstream after reflecting off the 2V pressure side.

There is significant interaction between the shocks and the airfoils. The blade

trailing edge shocks reflect off the 2V airfoils, travel back upstream, and impact the blade suction side. The blade suction side boundary layer thickness changes during and after this shock impingement. Shocks also reflect off the 2V pressure side and then impact the adjacent 2V suction side. Additionally, as the blade trailing edge shocks pass by the bow waves of the 2V airfoils, the shock angle oscillates. This oscillation creates additional loss as the shock becomes more normal to the flow direction. The time variation of entropy generation in a 1.5 stage highly loaded turbine is shown in Figure 6-20.

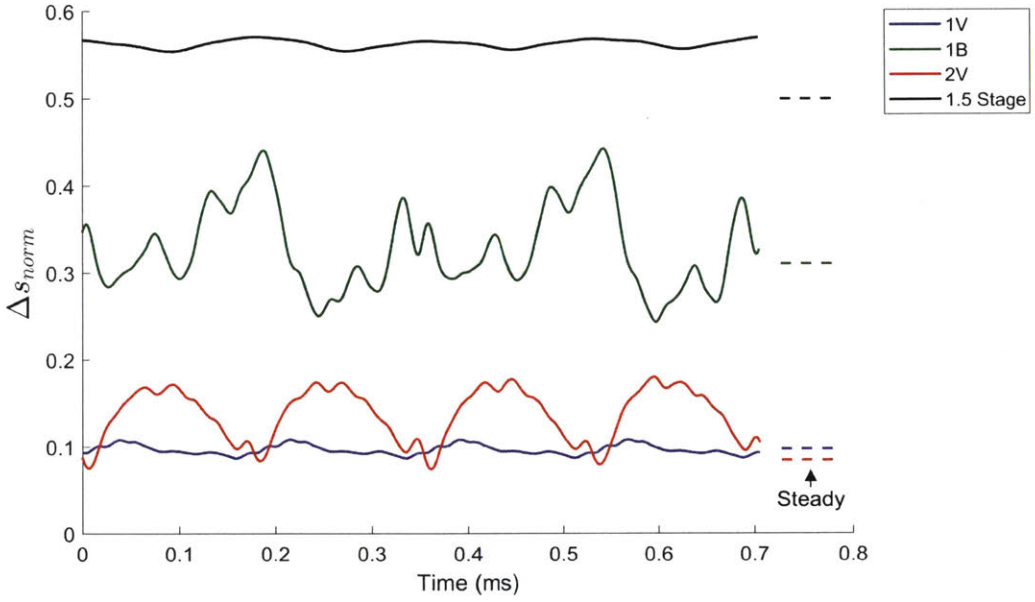

Figure 6-20: Unsteady entropy generation for the 1V, 1B, and 2V airfoil rows over 4 blade passing periods (2 vane passing periods). The total 1.5 stage entropy generation is the sum of the three airfoil rows. The steady computational result is shown at right for comparison.

Figure 6-21 shows a comparison of the inlet-to-exit CFD entropy generation for the steady and time averaged unsteady solutions. It is inferred that the addition of unsteady loss mechanisms yields a result in improved accord with the measured loss from the test data; nevertheless there is still a difference between the model and experimentally determined stage loss.

The unsteady entropy generation contributes an additional 13% to the overall loss,

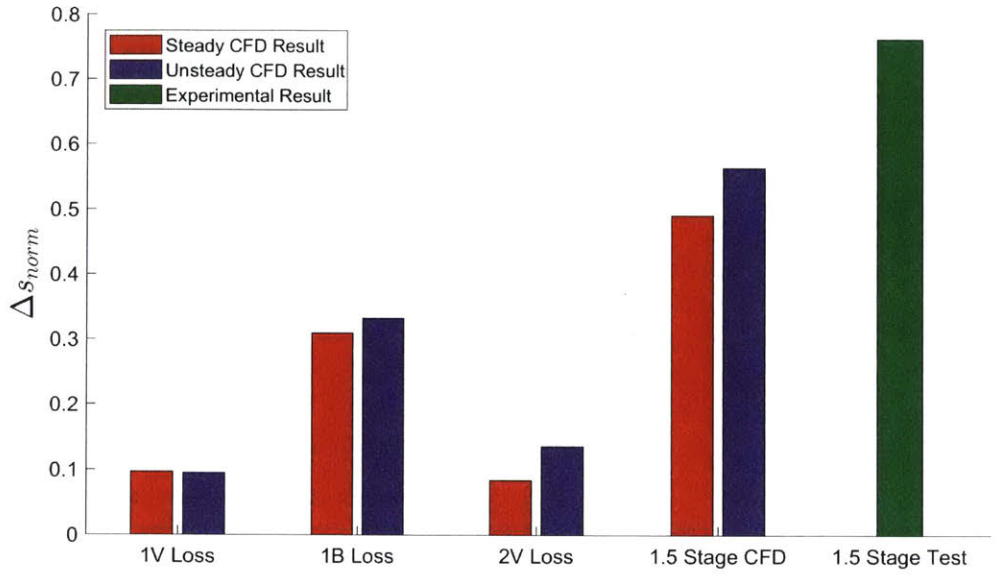

Figure 6-21: Steady loss compared to time averaged unsteady loss for a 3D multi-stage computation. The time averaged unsteady loss is in improved accord with the measured loss from test data.

and a significant portion of this loss occurs in the downstream 2V blade row. The oblique shock calculations described in Section 5.10 are carried out to identify the major contributing factor for the high unsteady losses in the second vane row. The result for the oblique shock model is in Figure 6-22.

The blue points represent the steady second vane CFD loss plus the oblique shock loss from control volume calculation. This is a quasi-steady calculation for individual time points. There is variation in the calculation result since the shock angle and location is based upon the graphical interpretation of the shock location. The error bars represent the maximum and minimum calculation result after 10 independent graphical shock position selections. An improved algorithm to better identify shock position and angle will reduce this variation. It can be seen that the oblique shock loss accounts for much of the additional loss observed in the downstream vane row in the unsteady CFD analysis. This result assumes that the profile loss, trailing edge loss, and endwall loss are constant between steady and unsteady conditions. In reality, these loss mechanisms will also vary, but likely much less than the additional shock

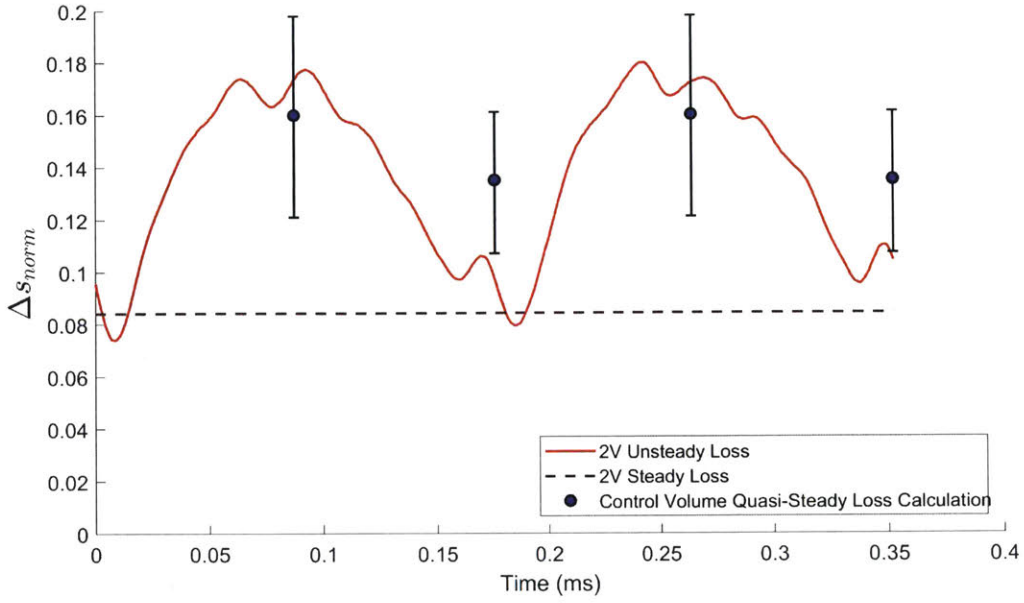

Figure 6-22: Oblique shock loss contribution to second vane row unsteady loss.

loss that is not present in the steady solution.

6.4 Loss in a Cooled Turbine Stage

The entropy generated by the introduction of purge and cooling flow can be estimated from the control volume method described in Section 5.9. Figure 6-23 shows the entropy generation estimated from the control volume method compared to the CFD result for each airfoil row and also the total stage. The purge flow loss and cooling flow loss are estimated separately, so they can be individually assessed against the CFD results.

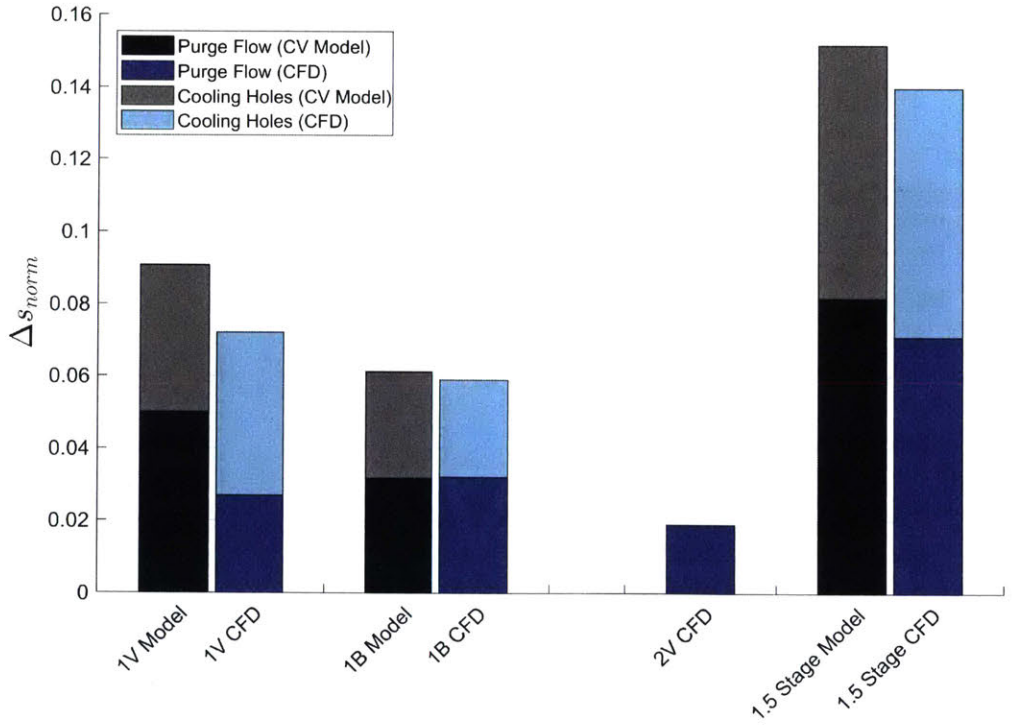

Figure 6-23: Control volume estimation of cooling loss compared against CFD computational result for cooling loss.

The first purge flow source is introduced into the first vane domain at the hub surface aft of the trailing edge. It is modeled with source terms on the hub surface and represents the flow through the rotor-stator gap. A second purge flow source is introduced in the 1B domain at the outer diameter case surface forward of the blade leading edge. This represents the flow through the blade outer air seal (BOAS). The cooling flow is introduced through 652 holes on the first vane airfoil and endwalls and

425 holes on the blade. The entropy generation for each cooling hole is estimated individually and added together for the result in Figure 6-23. The loss estimated from the control volume method is quantitatively comparable to the CFD result. The control volume estimation for stage cooling and purge loss is within 9% of the CFD result.

The steady uncooled, unsteady, purge flow only, and cooled CFD simulations are synthesized to yield a loss level for assessment against the experimentally determined 1.5 stage turbine loss. The cooling flow result is calculated considering that only 16 out of 23 vanes are cooled in the blowdown rig and only 34 out of 46 blades are cooled. The losses for each airfoil row and the 1.5 stage total are shown in Figure 6-24.

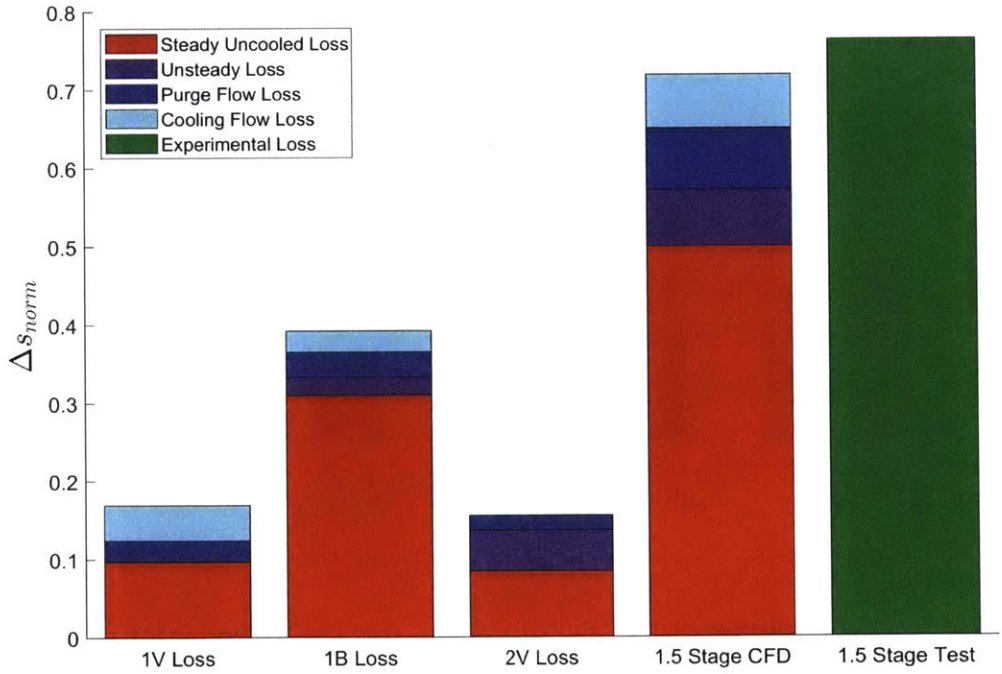

Figure 6-24: Computational entropy generation results for the individual airfoil rows and entire 1.5 stage turbine are compared to the experimentally determined entropy generation of the HIT blowdown rig. The steady uncooled loss, unsteady loss, purge flow loss, and cooling flow loss are identified separately.

The first vane has considerable purge flow and cooling losses, and negligibly small loss contribution from flow unsteadiness. The bow wave from the blade does not

greatly influence the time averaged entropy generation of the first vane row. The blade has significant unsteady loss from shock oscillation, interaction with the first vane wake, and reflected shocks traveling upstream from the second vane and interacting with the blade suction side boundary layer. The blade also has significant loss from the BOAS purge flow and the cooling flow. The second vane has a loss from purge flow injection, even though the purge flow is introduced upstream of the blade leading edge, because of a higher mass flow rate through the second vane. The second vane row has a large loss from unsteady effects. The unsteady loss is determined to be caused by blade trailing edge shocks propagating into the downstream vane row. The quasi-steady application of normal shock relations yields a loss comparable to the unsteady loss level estimated using unsteady CFD simulations.

The results of Figure 6-24 can also be shown in terms of overall 1.5 stage total-total efficiency. The Hartsel efficiency definition [18] is used to account for the cooling flow introduction. Figure 6-25 is a walk from the steady uncooled to the unsteady cooled 1.5 stage computed efficiency compared to the experimentally determined 1.5 stage efficiency.

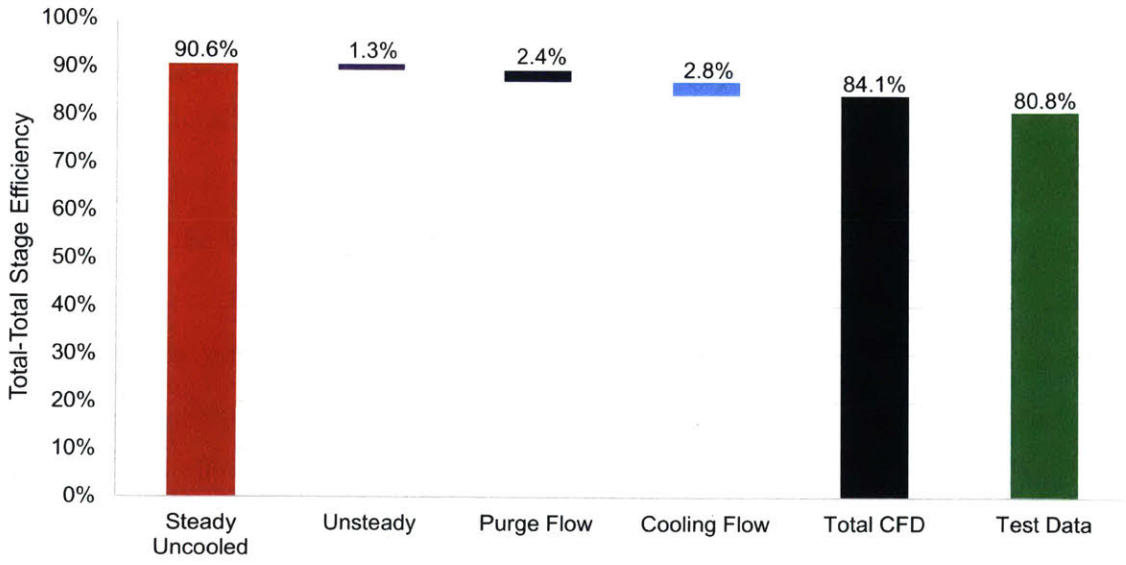

Figure 6-25: Stage efficiency walk from steady, unsteady, purge flow, and cooling flow losses compared to blowdown rig test data.

The overall loss from the CFD assessment is 5.6% lower than the experiment

result (see Figure 6-24), and the difference in stage efficiency is 3.3% (see Figure 6-25). The difference between analysis and test may be explained by additional loss generating mechanisms that are not modeled in the CFD, or it may be inherent to the RANS CFD modeling used. Additional loss could be generated by the blade and vane mounted instrumentation, rakes, or imperfect flowpath surfaces. Heat transfer to the test hardware during the relatively fast blowdown period increases the apparent experimentally measured efficiency compared to the adiabatic CFD result, therefore, if heat transfer is accounted for the results will be more dissimilar. A major assumption of the efficiency calculation is that all measured venturi flow from the cooling and purge air circuits enters the flowpath. If any of this flow exits the test rig as leakage or downstream of the exit rake, the calculated efficiency will be higher. Overall, the CFD analysis and experimental data are quantitatively comparable, and this gives confidence that the blowdown rig physics are captured in the 1.5 stage CFD assessment.

6.5 Mach Number and Pressure Ratio Variation

The simple control volume loss model results closely represent the CFD computed loss and test results for overall stage loss. Parameter variation is performed to assess the impacts of pressure ratio, exit Mach number, and incidence angle on the individual loss components of the rotor blade. For the parametric assessment of loss, only 2D computations are implemented at varying boundary conditions.

Denton's trailing edge loss model [1] and the extended trailing edge model in Equation 5.13 are compared to the CFD computation. Figure 6-26 depicts the control volume loss and the CFD computed loss dependence on Mach number. The simplified trailing edge model from Denton [1] is used, and the total loss model result overestimates the CFD result by up to 50%.

The extended trailing edge model that accounts for deviation is applied, and Figure 6-27 is the updated result. The loss models now reflect the same trend and general magnitude as the CFD computed result.

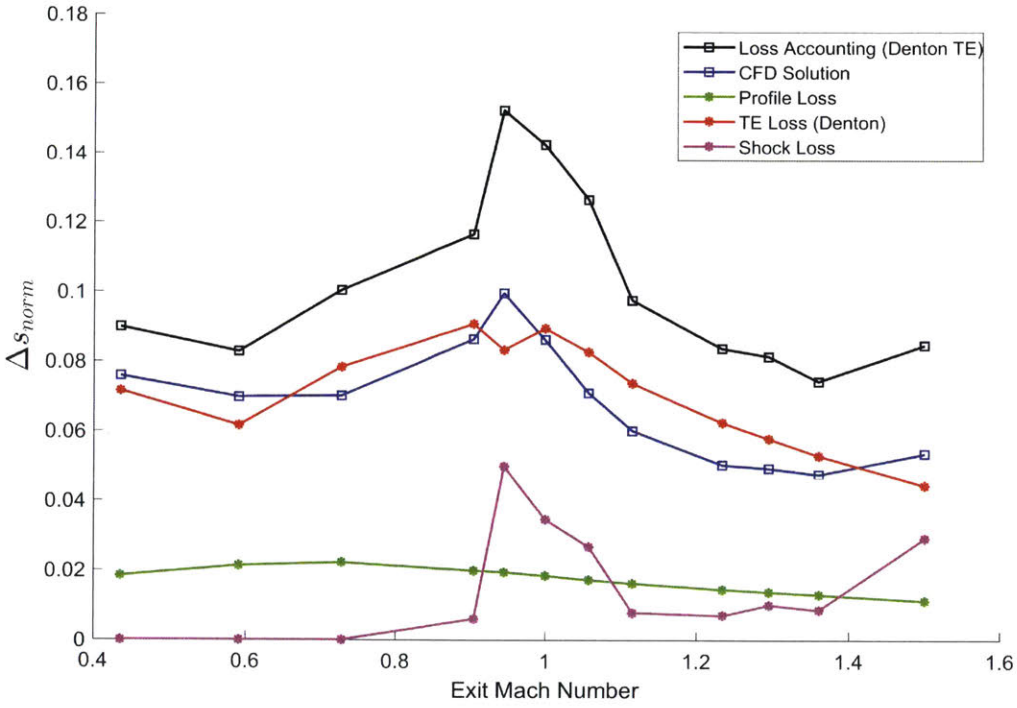

Figure 6-26: Control volume models and CFD computed loss versus exit Mach number. The trailing edge model assumes $\delta = 0$, and the control volume models overestimate the loss.

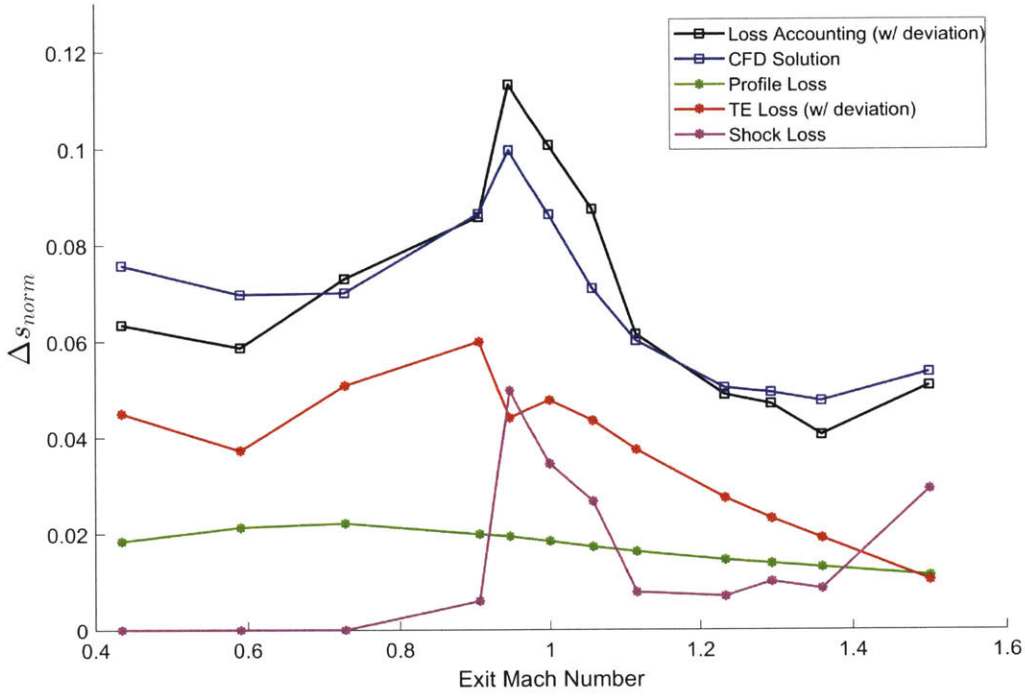

Figure 6-27: Control volume models and CFD computed loss versus exit Mach number. The trailing edge model assumes $\delta \neq 0$, and the control volume model result is comparable to the computational result.

The loss accounting control volume models result in the same maximum as the CFD solution at Mach 0.95. At this condition, the pressure side trailing edge shock is perpendicular to the airfoil throat and the shock loss is large. As the Mach number increases, the trailing edge shock becomes more oblique to the flow direction with a resulting decrease in shock loss. At Mach 1.5 the velocity is high enough that the reflected shock loss (pressure side trailing edge shock reflecting off the adjacent airfoil suction side) becomes significant. The loss models yield a result with the same minimum as the CFD computed result at Mach 1.35.

Similar loss trends are observed in the parametric variation with pressure ratio, since pressure ratio is directly related to blade exit Mach number. Figure 6-28 shows the loss variation with the pressure ratio across the blade row.

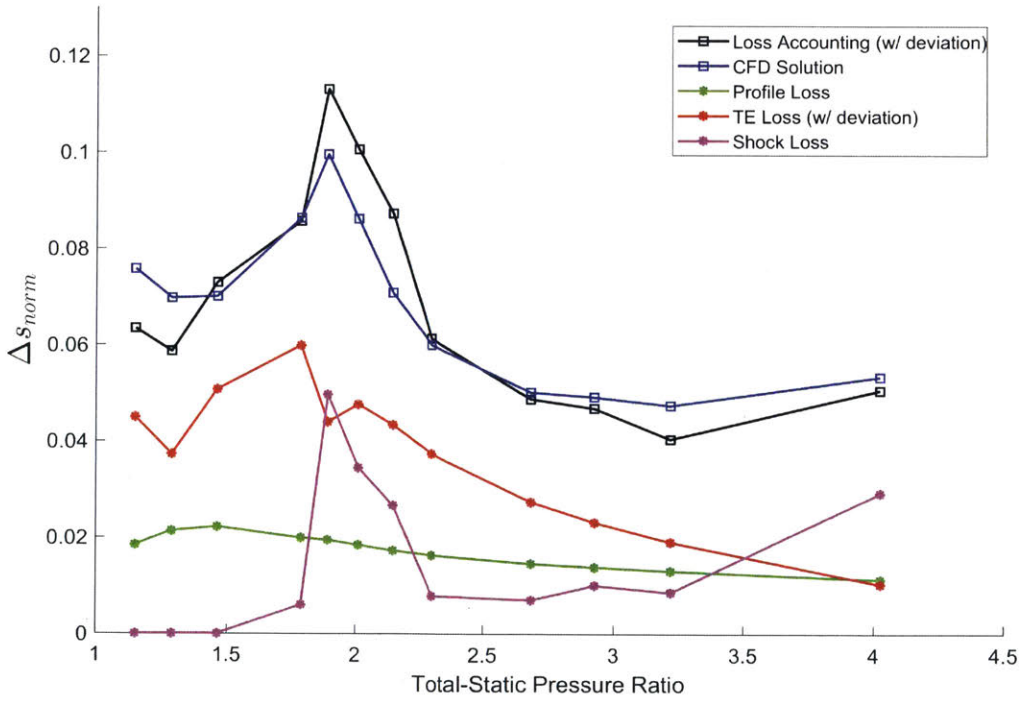

Figure 6-28: Control volume models and CFD computed loss versus turbine blade pressure ratio. The control volume model trends and magnitude are comparable to the computational result.

Figure 6-29 is the change in trailing edge deviation with blade exit Mach number. The trailing edge deviation becomes more negative as the trailing edge shock strength

increases and the shock angles change. When the blade row exit Mach number approaches 1, there is a step change in deviation. It is important to account for this deviation when estimating trailing edge loss for highly loaded transonic airfoils with an exit angle above 65 degrees.

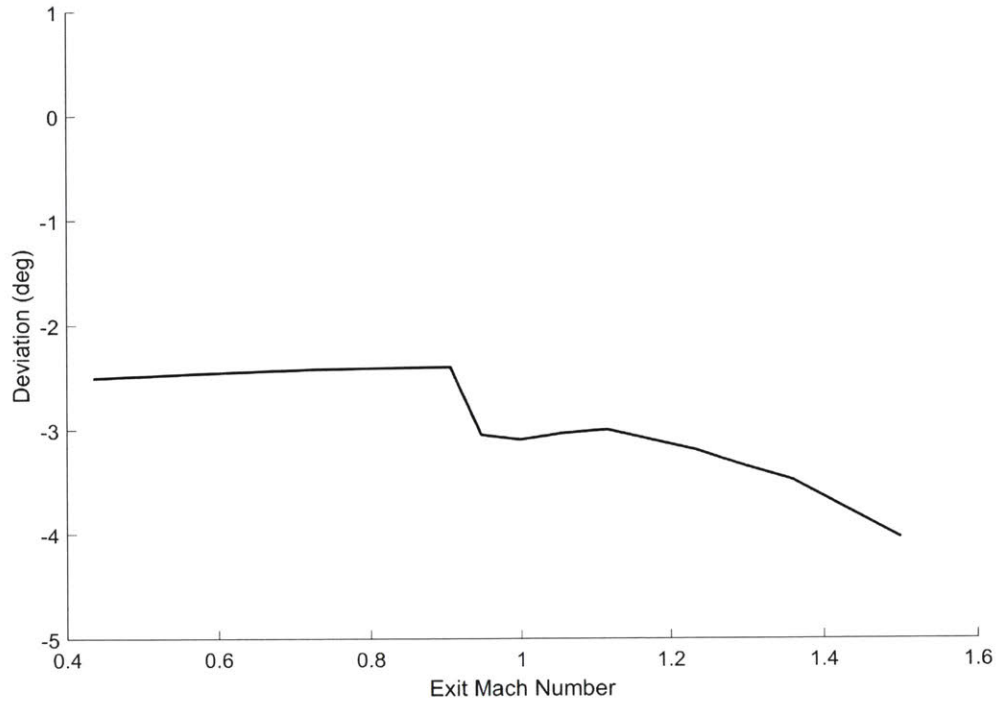

Figure 6-29: Trailing edge deviation angle variation with exit Mach number.

6.6 Incidence Angle Variation

Incidence angle is also varied to assess the effect on loss. Figure 6-30 is the loss component dependency on blade row incidence angle.

The design point incidence angle is 48.5 degrees; however, the multistage result shows the blade operates at a higher incidence of 60.5 degrees during the blowdown test. The loss accounting model results are quantitatively comparable to the CFD computed results. There is little variation in loss for angles from 30 to 60.5 degrees. At 70 degrees there is fully separated flow on the suction side, resulting in a large

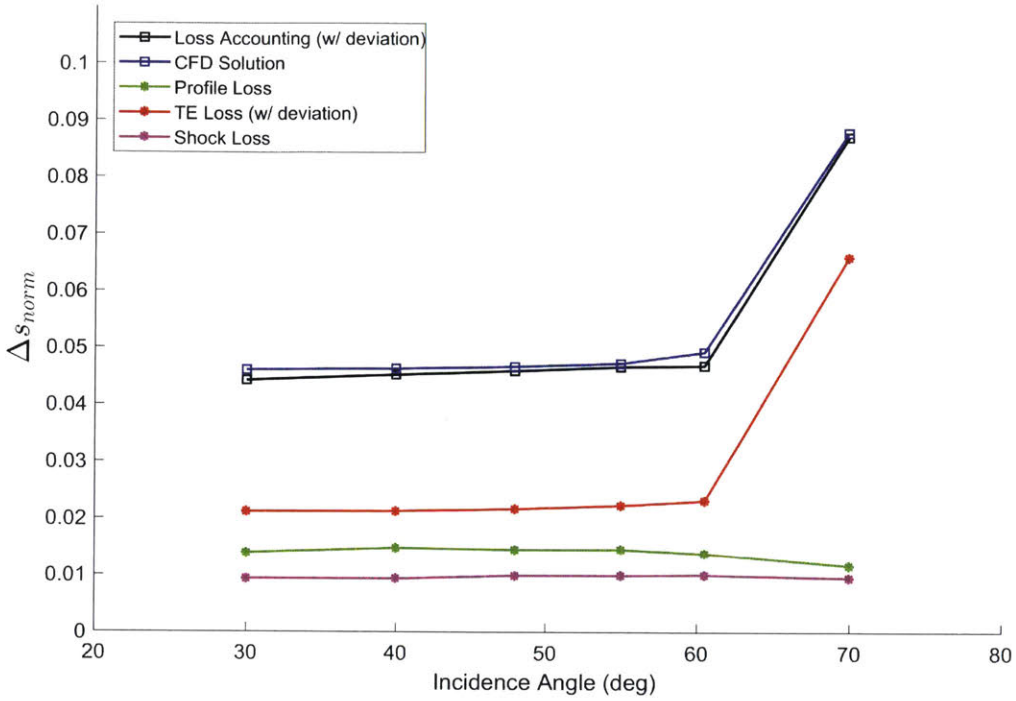

Figure 6-30: Loss component variation with blade incidence angle variation at $M_{exit} = 1.3$. The sum of the individual loss accounting model results is comparable to the computational result.

boundary layer thickness. The trailing edge loss model robustly estimates the overall rise in entropy in accord with the CFD computed result.

6.7 Summary

The loss models are applied to three airfoil rows of a 1.5 stage highly loaded transonic turbine. The simple control volume loss accounting results are quantitatively comparable to the computational entropy generation from CFD. An extended trailing edge loss model is used which accounts for negative deviation observed in a highly loaded transonic airfoil. Application of the extended trailing edge loss model brings the simple control volume results into improved accord with the computational solution. Steady, unsteady, and cooled 1.5 stage simulations are implemented to compare the computational results to the experimental data. The steady loss, unsteady loss, purge flow loss, and cooling flow loss are calculated from the CFD results, and the total 1.5 stage loss is within 6% of the blowdown test result. A parametric assessment of the loss accounting models, applied to the blade cascade, results in a non-monotonic trend with exit Mach number, pressure ratio, and incidence angle.

Chapter 7

Summary and Future Work

The flow in a 1.5 stage highly loaded transonic turbine representative of future generation turbine aerodynamics technology is assessed for its role in loss generation. Steady and unsteady flow computations, complemented by simplistic control volume analyses as well as test data, provide results for determining the quantitative level of loss from each source. The geometry for computational assessments of flow matches the geometry tested in a cascade and blowdown turbine research rig. The overall loss determined from unsteady three-dimensional flow computations of a cooled 1.5 stage turbine is within 6% of that inferred from the blowdown turbine rig test data. The computed flows are post-processed to allow an estimation using control volumes of blade profile loss, trailing edge loss, shock loss, endwall loss, secondary flow loss, tip leakage loss, cooling injection loss, and unsteady flow loss.

7.1 Summary and Key Findings

The individual loss sources for a 1.5 stage highly loaded transonic turbine are quantified for each airfoil row with control volume based loss models. The entropy generation estimated from the loss accounting models is within 10% of the two-dimensional and three-dimensional computational results. The dominant loss sources are determined to be trailing edge loss, profile loss, and tip leakage loss.

The estimated trailing edge loss is found to have a strong functional dependence

on deviation angle. The computed flows show that the flow deviation in a highly loaded transonic turbine airfoil with trailing edge shocks is negative (-2° to -4°), and estimating the trailing edge loss by assuming zero flow deviation in a simple control volume approach would yield a significantly higher value. An extended trailing edge loss model is implemented which accounts for trailing edge deviation. The results from the extended model agree closely with the computational results for a range of stage pressure ratios, Mach numbers, and incidence angles.

Unsteady effects increase the loss in a 1.5 stage highly loaded turbine by 13%. The majority of the unsteady loss is concentrated in the downstream vane row. The loss is generated by rotor trailing edge shocks propagating into the downstream vane domain. The shocks reflect off of the downstream vane surface and travel upstream to interact with the blade. Normal shock loss calculations applied to individual timepoints of the unsteady analysis give a result commensurate with the downstream vane row unsteady computed flow fields.

Parametric assessment of the loss models shows a non-monotonic trend with pressure ratio and exit Mach number. An increase in loss at an exit Mach number of 0.95 is identified, and the loss is a minimum between Mach 1.3 and 1.4. At higher Mach numbers the loss increases with increased shock loss. A parametric variation of the loss accounting control volume models is comparable to the magnitude and trend of computational results.

The results are consistent with Mee's assessment of a turbine cascade [3] which found downstream mixing loss (composed mostly of trailing edge loss) is larger than profile and shock loss at high Mach numbers. Mee also identifies a sharp rise in shock loss at an exit Mach number of 0.95 and a decrease in shock loss above Mach 1.1. The loss trends also agree with Duan's conclusion for the blade 1 cascade [4]; however, the trends are more pronounced for the HIT design which is more highly loaded and has a thicker trailing edge. The shock loss and trailing edge loss are significantly higher for the HIT turbine.

7.2 Recommendation for Future Work

The conclusions in this thesis rely on assumptions and simplifications that can be challenged to increase the understanding of loss generating fluid mechanisms in highly loaded transonic turbine stages. The following topics are suggested for future study.

1. Develop a simple quasi-steady model for quantifying the unsteady downstream loss in a highly loaded transonic turbine stage.

2. Assess the extended trailing edge loss model against additional turbine designs and design parameters. The trailing edge loss model accuracy depends on the process for interrogating the computational solution and is sensitive to deviation. The extended model is intended to be a simple trailing edge loss model that captures effects of negative deviation, boundary layer thickness, geometry, and base pressure. Simplified studies can be carried out to assess the application of this extended model. Future work to estimate deviation angle from trailing edge shock strength and angle would be useful to the turbine designer.

3. Extend the loss accounting framework by increasing the fidelity of the loss categorization. Spanwise variation in loss generating mechanisms can be identified and quantified. Second order effects such as the interaction between loss mechanisms can be assessed. For example, what is the impact of cooling flow injection on shock loss?

4. Perform experiments to identify loss reduction opportunities from modifying the downstream vane. The AFRL shows that blade unsteadiness is greatly reduced by a bowed vane configuration; however, it will be useful to quantify the loss impact on a back-to-back basis.

5. Use unsteady computational models to determine the unsteady forcing on the blade and vane rows from shock impingement. An aeromechanical forced response assessment will be useful to quantify the fatigue life impact of various second vane designs.

Bibliography

[1] Denton, J.D. Loss Mechanisms in Turbomachines. *ASME Journal of Turbomachinery*, 115:621–656, October 1993.

[2] Denton, J.D., and Xu, L. The Trailing Edge Loss of Transonic Turbine Blades. *ASME Journal of Turbomachinery*, 112:277–285, April 1990.

[3] Mee, D.J., Baines, N.C., Oldfield, M.L.G., and Dickens, T.E. An Examination of the Contributions to Loss on a Transonic Turbine Blade in Cascade. *ASME Journal of Turbomachinery*, 114:155–162, April 1992.

[4] Duan, P., Tan, C.S., Scribner, A., and Malandra, A. Loss Generation in Transonic Turbine Blading. *ASME Journal of Turbomachinery*, 140, April 2018.

[5] Yoon, S., Vandeputte, T., Mistry, H., Ong, J., and Stein, A. Loss Audit of a Turbine Stage. *ASME Journal of Turbomachinery*, 138, May 2016.

[6] Huang, AC, Greitzer, E.M., Tan, C.S., Clemens, E.F., Gegg, S.G., Turner, E.R. Blade Loading Effects on Axial Turbine Tip Leakage Vortex Dynamics and Loss. *ASME Journal of Turbomachinery*, 135, September 2013.

[7] Sakulkaew, S., Tan, C.S., Donahoo, E. Cornelius, C., and Montgomery, M. Compressor Efficiency Variation with Rotor Tip Gap from Vanishing to Large Clearance. *ASME Journal of Turbomachinery*, 135, June 2012.

[8] Zlatinov, M.B., Tan, C.S., Montgomery, M. Islam, T., and Harris, M. Secondary Air Interaction with Main Flow in Axial Turbines. Master's thesis, Massachusetts Institute of Technology, 2011.

[9] Clifton, D. Impact of Unsteady Secondary Air Flow Interaction with Main Flow on Loss Generation in Axial Turbines. Master's thesis, Massachusetts Institute of Technology, 2012.

[10] Horlock, J.H., Watson, D.T., and Jones, T.V. Limitations on Gas Turbine Performance Imposed by Large Turbine Cooling Flows. *Journal of Engineering for Gas Turbines and Power*, 123:487–494, July 2001.

[11] Horlock, J.H. The Basic Thermodynamics of Turbine Cooling. *ASME Journal of Turbomachinery*, 123:583–592, July 2001.

[12] Lim, C.H., Pullan, G., and Northall, J. Estimating the Loss Associated with Film Cooling for a Turbine Stage. *ASME Journal of Turbomachinery*, 134, March 2012.

[13] Ng, W.F., and Epstein, A.H. Unsteady Losses in Transonic Compressors. *ASME Journal of Engineering for Gas Turbines and Power*, 107:345–353, April 1985.

[14] Anthony, R.J., and Clark, J.P. A Review of the AFRL Turbine Research Facility. *ASME Turbo Expo 2013: Turbine Technical Conference and Exposition*, 94741, June 2013.

[15] Ooten, M.K. Unsteady Aerodynamic Interaction in a Closely Coupled Turbine Consistent with Contrarotation. Master's thesis, University of Cincinnati, 2016.

[16] Mattingly, J.D. *Elements of Propulsion: Gas Turbines and Rockets*. AIAA, 2006.

[17] Ooten, M.K., Anthony, R.J., Lethander, A.T., and Clark, J.P. Unsteady Aerodynamic Interaction in a Closely Coupled Turbine Consistent with Contrarotation. *ASME Journal of Turbomachinery*, 138, June 2016.

[18] Young, J.B., and Horlock, J.H. Defining the Efficiency of a Cooled Turbine. *ASME Journal of Turbomachinery*, 128:658–667, October 2006.

[19] Prasad, A. Calculation of the Mixed-Out State in Turbomachine Flows. *ASME Journal of Turbomachinery*, 127:564–572, July 2005.

[20] Greitzer, E.M., Tan, C.S., and Graf, M.B. *Internal Flow: Concepts and Applications*. Cambridge University Press, Cambridge, UK, 2004.

[21] Benner, M.W., Sjolander, S.A., and Moustapha, S.H. An Empirical Prediction Method for Secondary Losses in Turbines - Part I: A New Loss Breakdown Scheme and Penetration Depth Correlation. *ASME Journal of Turbomachinery*, 128, April 2006.

[22] Kumar, K.N., and Govardhan, M. Secondary Flow Loss Reduction in a Turbine Cascade with a Linearly Varied Height Streamwise Endwall Fence. *International Journal of Rotating Machinery*, March 2011.

[23] Benner, M.W., Sjolander, S.A., and Moustapha, S.H. An Empirical Prediction Method For Secondary Losses In Turbines - Part II: A New Secondary Loss Correlation. *ASME Journal of Turbomachinery*, 128, April 2006.

[24] Huang, A.C. Loss Mechanisms in Turbine Tip Clearance Flows. Master's thesis, Massachusetts Institute of Technology, 2011.

[25] Liepmann, H.W. and Roshko, A. *Elements of Gasdynamics*. John Wiley and Sons, Inc, 1957.